journal of
physics

Vol. 50 No. 5
May 1998

DIAN ACADEMY OF SCIENCES
an National Science Academy

amana journal of physics Vol. 50 (No. 5), May 1998

Contents

ew

ation of $3^{1,3}P$ and $3^{1,3}D$ states of helium from the ground 1^1S state by ons and positrons . . . . *Surbhi Verma and Rajesh Srivastava* 355

arch Articles

ciation energy of diatomic molecules . . . .*Sarvpreet Kaur and C G Mahajan* 397

splitting and energy transfer between Dy^{3+}–Ho^{3+} and between Tb^{3+}–Er^{3+} cium–lithium borate glass . . . . *Brajesh Sharma, V B Singh, D K Rai and S B Rai* 405

optogalvanic spectroscopy of argon in the wavelength region 605–740 nm . . . . *R C Sharma, T Kundu and S N Thakur* 419

lectrostatic charge state selector for ion-atom collisions: Design, spectral hapes and performance . . . .*Amal K Saha, K V Thulasi Ram, L C Tribedi, W A Fernandes, S D Narvekar, V Nanal, M B Kurup, K G Prasad and P N Tandon* 433

Report

electron scattering cross sections for carbon dioxide at low electron ies . . . .*P Rawat, K P Subramanian and Vijay Kumar* 447

etization of high T_c superconductors . . . .*B Kalta and K K Nanda* 459

R Nityananda
Raman Research Institute, Bangalore

Associate Editor

H R Krishnamurthy
Indian Institute of Science, Bangalore

Editorial Board

G S Agarwal, *Physical Research Laboratory, Ahmedabad*
V Balakrishnan, *Indian Institute of Technology, Chennai*
J K Bhattacharjee, *Indian Assoc. for the Cultivation of Science, Calcutta*
D N Bose, *Indian Institute of Technology, Kharagpur*
B M Deb, *Panjab University, Chandigarh*
Rohini M Godbole, *Indian Institute of Science, Bangalore*
S Kailas, *Bhabha Atomic Research Centre, Mumbai*
R K Kaul, *The Institute of Mathematical Sciences, Chennai*
A V Khare, *Institute of Physics, Bhubaneswar*
T Padmanabhan, *Inter-Univ. Centre for Astronomy and Astrophysics, Pune*
R Ramaswamy, *Jawaharlal Nehru University, New Delhi*
A K Raychaudhuri, *National Physical Laboratory, New Delhi*
K C Rustagi, *Centre for Advanced Technology, Indore*
E V Sampathkumaran, *Tata Institute of Fundamental Research, Mumbai*
Abhijit Sen, *Institute for Plasma Research, Gandhinagar*
S K Sikka, *Bhabha Atomic Research Centre, Mumbai*
Y Singh, *Banaras Hindu University, Varanasi*

Editor of Publications of the Academy

N Mukunda
Indian Institute of Science, Bangalore

Annual Subscription Rates

All countries except India (Price includes AIR MAIL charges)	US$ 200
India	Rs. 200

Annual subscriptions for individuals for India and abroad are Rs. 100/- and $50 respectively.

All correspondence regarding subscription should be addressed to the Circulation Department of the Academy

---

Editorial Office

Indian Academy of Sciences, C V Raman Avenue,
P.B. No. 8005, Bangalore 560 080, India

Telephone: 334 2546
Telefax: 91-80-334 6094

Email: pramana@ias.ernet.in

Excitation of $3^{1,3}P$ and $3^{1,3}D$ states of helium from the ground 1^1S state by electrons and positrons

SURBHI VERMA and RAJESH SRIVASTAVA
Department of Physics, University of Roorkee, Roorkee 247 667, India

MS received 25 September 1997; revised 2 April 1998

Abstract. A systematic theoretical study is carried out for the electron and positron impact excitation of the $3^{1,3}P$ and $3^{1,3}D$ states of helium from the ground 1^1S state. The results are reported for the differential cross sections, Stokes parameters and alignment and orientation parameters. To calculate the scattering amplitude which relate these parameters, a distorted wave approximation theory with different choices of distortion potential has been used. The results are compared with available theoretical and experimental data in the energy range of 40–100 eV.

Keywords. Excitation; electrons; positrons; helium.

PACS No. 34.80

1. Introduction

Most of the pioneering experimental studies of the fundamental processes in electron-atom scattering such as elastic, excitation and ionization have been carried out with helium as target. Theoretically also any approximate method for a particular type of collision process before being recommended for the general use/application (i.e for heavier atoms) is first tested for hydrogen and helium. The studies on helium are more challenging due to the presence of two electrons in it which permits inter-electron repulsion to be introduced in a realistic manner. Further, helium being an inert gas is much easier to handle experimentally and because of this reason measurements with helium are more readily available than for hydrogen. In addition, the study of electron-helium scattering processes have wide ranging practical applications in the field of plasmas and lasers for their understanding. Also, helium is an abundant element and, therefore, helium emissions are widely observed in a variety of stellar and interstellar media, and are in turn used for determining abundances of this element. It is, therefore, important to provide quantitative electron collision cross sections for this target as well as to measure/calculate those scattering parameters which provide best test of a scattering theory.

In this paper we focus our attention and deal with the electron (positron)-impact excitation of the $n = 3$ states of helium from its ground state with the point of view of differential cross sections and electron-photon coincidence results. Though electron the excitation cross sections for the $n = 3$ states are very low in magnitude for measurements as compared to those for $n = 2$ states which are order of magnitude higher. Also the close proximity of the $n = 3$ states make resolution of individual 3^3D, 3^1D and 3^1P states impossible even with the best available electron energy resolution. This can be understood from the fact that the 3^1D and 3^3D states are separated by less than 1 meV and the 3^1P state is only separated from them by $\cong 13$ meV. For example, differential scattering electron-energy-loss-spectroscopy (EELS) has yielded a significant quantity of data concerning both elastic and inelastic electron scattering channels. Using this conventional EELS, the measurement of differential cross sections for the excitation of all the strong $1^1S \rightarrow n^1P$ transitions in helium in principle should be possible, but have been limited to the energetically resolvable $1^1S - 2^1P$ transition providing for it the most accurate inelastic differential cross section (DCS) measurements. Until recently, (see for example paper of Khakoo *et al* [1]), no absolute experimental differential cross sections were available for the excitation of the n^1P levels ($n > 2$) and the reasons being that conventional EELS from gaseous targets (employing electron beams of intensity of several nA) cannot provide the high energy resolution (< 13 meV) required to resolve the 3^1P and 4^1P levels from close-by levels, as well as providing adequate scattered electron signal for precise DCS measurements.

However, in recent years, progress in the electron-photon coincidence angular and polarization techniques has greatly helped and provided the study of the excitation of the individual $3^{1,3}P$ and $3^{1,3}D$ states. As the scattered electron-decay photon coincidence technique takes the advantage of the fact that photons from the decay of these states, having different life times, can be readily isolated. Thus we find that most of the work published for individual $n = 3$ excitations in helium have become available only during the last couple of years when the coincidence experiments to study such excitations have started. To compare with these experiments many theoretical calculations such as R matrix (for low energies), close-coupling, first order many body theory and distorted wave Born approximation have been reported which specifically gave the results only for the range of scattering angles and the incident energies where the experimental data are available.

In our previous papers [2, 3] we considered in detail the study of the $n = 3$ excitations in hydrogen and in continuation we give here our systematic similar detailed study of the $n = 3$ excitations in helium. We consider excitation of all the four $3^{1,3}P$ and $3^{1,3}D$ states from the ground 1^1S state by impact of both the electrons and positrons. Note that with the positron impact only excitation of the 3^1P and 3^1D states will be possible. For the present study we extend our distorted wave approximation (DWA) calculation as used for hydrogen and helium [2–4]. Though the method used here is similar to the distorted wave Born approximation (DWBA) method used earlier by Madison and co-workers [6–8] and Katiyar and Srivastava [9], we have considered and tested now some extra features such as the incorporation of exchange and polarization effects in the distortion potential. Also as the different theories and experiments have reported results in a scattered manner for different parameters i.e. only at selected energies and (or) in particular range of scattering angles we present systematic detailed calculations for differential cross sections, Stokes combined $3^1P + 3^1D + 3^3D$ states. Amongst these Chutijian and Thomas [10] made a semi empirical attempt to obtain the DCS for the $n = 3$ levels using electron-energy-loss-spectroscopy and used first order many body theory (FOMBT) to calculate the contribution, to the signal, from the 1^1S–3^1D and 3^3D. They gave results at incident electron energies of 29.7, 39.2 and 40 eV. Trajmar and co-workers [11] reported results at 30, 50, 100 eV for the combined $3^1P + 3^1D + 3^3D$ states alongwith giving an estimation for the DCS for the excitation of the 3^1P level at 80 and 100 eV. Allan [12] reported results in the low energy region i.e. 4 eV above threshold. Further, Hummer and Burns [13] carried out the only direct relative differential cross section measurements for the excitation of the 3^1P (with magnetic substate $M_f = 0$) state. To compare with these experimental data several theoretical calculations have been attempted [11, 14–16]. Madison [8] using the distorted wave Born approximation (DWBA) reported the DCS results at 80 and 100 eV. Cartwright *et al* [11] carried out the first order many body theory (FOMBT) calculations and reported the DCS for individual 3^1P, 3^1D and 3^3D states at 30, 40, 50 and 100 eV and thus also gave the DCS for combined $3^1P + 3^1D + 3^3D$ states. In a separate paper Csanak *et al* [14] reported the DCS for magnetic substates with $M_f = 0, \pm 1$ for the excitation of the 3^1P level at 50, 70, 80 and 100 eV. In this paper they also tabulated the experimental DCS data for different magnetic sublevels obtained using previously available data for DCS summed over different magnetic sublevels and the λ parameter. Recently Fursa and Bray [15] carried out a convergent close coupling (CCC) calculation for the DCS for combined He $(3^1P + 3^1D + 3^3D)$ excitations in the energy region of 30–500 eV. In the low energy region Fon *et al* ([16], and references therein) carried out 19-state and 29-state *R*-matrix calculations for the DCS of the excitation to individual $3^{1,3}P$ and $3^{1,3}D$ states of helium. In addition to these various reports of differential cross section results, the measurements and theoretical calculations have also been reported for the electron-photon coincidence studies on the excitation of the 3^1P state of helium. Eminyan *et al* [17] obtained experimental data for the λ and χ parameters at incident electron energies between 50–150 eV whereas McAdams and Williams [18] reported the λ and χ parameters at an energy of 81.2 eV. In a later paper Beijers *et al* [7] measured the alignment and orientation parameters for the 3^1P state of helium in the energy range 50–80 eV. Theoretical calculations for these parameters are those using FOMBT [19], DWBA [7] and CCC [15] methods. Further, in the low energy region Neill and Crowe [20] and Neill *et al* [21] reported the electron-photon coincidence parameters at 26.5 and 29.6 eV energies respectively. To compare with these low energy measurements Fon *et al* [22] carried out the *R*-matrix calculations for λ and χ parameters.

For the 3^3P excitation of helium from the ground 1^1S state some measurements for DCS have been carried out in the intermediate energy range viz. at 39.7 eV by Chutijian and Thomas [10], at 30, 50 and 100 eV by Trajmar *et al* [23] and at 40, 60 and 80 eV by Batelaan *et al* [24]. The results of Batelaan *et al* [24] were extracted from the existing data for electron-photon coincidence experiments. To compare with these available data in this intermediate energy range theoretical calculations using the FOMBT [23], DWBA [6] and CCC [15] have been performed. Further, in the low energy range Allan [12]

Amongst these are the experimental data of Silim *et al* [25] and Beijers *et al* [26] at 60 eV for Stokes parameters and alignment and orientation parameters, Humphrey *et al* [27] for Stokes parameters at 39.7 and 23.5 eV and Donnelley *et al* [28] for the angular correlation studies at 29.6 eV. The theoretical calculations for these parameters have been carried out using FOMBT [29] and DWBA [6] in the intermediate energy region and using CCC [15] and *R*-matrix [22] for low energies.

For the He ($1^1S - 3^{1,3}D$) excitations the only experimental data reported for DCS are due to Batelaan *et al* [24] who extracted the results from the available electron-photon coincidence experimental data as they did for 3^3P excitation. The existing theoretical calculations for $3^{3,1}D$ excitations in the intermediate energy range of 40–100 eV for the DCS are again from FOMBT [11], DWBA [6], CCC [30, 31] and multi channel eikonal theory (MET) [32, 33]. As compared to the differential cross section measurements relatively more attention has been devoted to the experimental determination of electron-photon coincidence parameters for $3^{1,3}D$ excitations. Thus the work that started from the angular correlation studies of the 3^1D states of helium (van Linden van den Heuvell *et al* [34]) has given impetus to many other studies and now various results for excitation of the $3^{1,3}D$ states in helium have been reported with increasing pace. The recent experimental papers [35–37] alongwith the reviews of Andersen *et al* [38] and Slevin and Chwirot [39] describe in a comprehensive manner the details of the angular and polarization correlation data available for these two transitions at different selected energies. Theoretically electron-photon coincidence results for the He (3^1D) excitation process are obtained using the DWBA [6], FOMBT [40, 41], MET [32, 33], CCC [30] and in the low energy region from *R*-matrix ([16] and references therein). Similarly the He (3^3D) excitation is also considered by Bartschat and Madison [6], Bray *et al* [31] and Fon *et al* [16].

2. Theoretical considerations

2.1 *T-Matrix*

The transition matrix for the electron (positron) impact excitation of helium from its initial state i to a final magnetic substate f_{M} in the distorted wave approximation (DWA) can be written as

$$T_{if_{\mathrm{M}}} = \langle \chi^-_{f_{\mathrm{M}}} | V - U_f | A \chi^+_i \rangle, \tag{1}$$

where A is the antisymmetrization operator which takes into account in case of electron impact excitation the contribution of electron exchange between projectile and target electrons, V is the total interaction potential and is given by

$$V = Z' \left(\frac{2}{\mathbf{r}_3} - \frac{1}{|\mathbf{r}_1 - \mathbf{r}_3|} - \frac{1}{|\mathbf{r}_2 - \mathbf{r}_3|} \right). \tag{2}$$

Here $Z' = -1\,(+1)$ is the projectile charge of the electron (positron), $\mathbf{r}_1$, $\mathbf{r}_2$ and $\mathbf{r}_3$ are where $\psi_{i(f_M)}$ is the initial (final) state wavefunction of the target helium atom and $S_{i(f)}(1,2;3)$ is the initial (final) state spin function for the composite system consisting of the incident projectile and the target. $F^{+(-)}_{i(f)}$ represents the initial (final) channel projectile distorted wave with the wave vector $\mathbf{k}_i(\mathbf{k}_f)$ and the associated superscript $+(-)$ indicates the usual outgoing (incoming) wave boundary condition. These distorted waves are the solution of

$$[\nabla_3^2 + \mathbf{k}^2_{i(f)} - 2U_{i(f)}(r_3)]F^{+(-)}(\mathbf{k}_{i(f)}, \mathbf{r}_3) = 0. \tag{4}$$

Here $U_{i(f)}$ is the distortion potential in the initial (final) channel.

On substituting the expressions for χ_i^+ and $\chi_{f_M}^-$ from (3) into the T-matrix (eq. (1)) we get

$$\begin{aligned} T_{if_M} =& \langle F^-(\mathbf{k}_f, \mathbf{r}_3)\psi_{f_M}(\mathbf{r}_1, \mathbf{r}_2)S_f(1,2;3)|V - U_f|F^+(\mathbf{k}_i, \mathbf{r}_3)\psi_i(\mathbf{r}_1, \mathbf{r}_2)S_i(1,2;3)\rangle \\ & - 2\delta_{Z',-1}\langle F^-(\mathbf{k}_f, \mathbf{r}_3)\psi_{f_M}(\mathbf{r}_1, \mathbf{r}_2)S_f(1,2;3)|V - U_f| \\ & \times F^+(\mathbf{k}_i, \mathbf{r}_1)\psi_i(\mathbf{r}_3, \mathbf{r}_2)S_i(3,2;1)\rangle, \end{aligned} \tag{5}$$

where $\delta_{Z',-1}$ is the Kronecker delta symbol and it goes to zero for positron impact causing the exchange term to be dropped from the T-matrix.

Further, the scattering amplitude a_{M} in the 'collision reference frame' is related to the DWA transition matrix element T_{if_M} for the electron (positron) impact excitation of helium from an initial state i to a final magnetic substate f_{M} by

$$a_{\mathrm{M}} = -\left(\frac{1}{2\pi}\right)T_{if_M}. \tag{6}$$

The expression for the T-matrix (eq. (5)) can be simplified further for a specific transition by carrying out the integrations over the spin co-ordinates. In this paper we consider two types of transitions, namely the excitation from the ground 1^1S state to excited 3^1D and 3^1P state i.e. singlet to singlet (SS) transition and the other is excitation from the ground 1^1S state to 3^3P and 3^3D states i.e. singlet to triplet (ST) excitations. We give below a brief outline how to evaluate the T-matrix for each SS and ST excitation processes.

2.2 *Singlet-singlet excitations* ($1^1S - 3^1P$ *and* 3^1D)

In the singlet-singlet excitations the scattering takes place in the doublet mode i.e. the total spin of the system $S = 1/2$. The doublet mode spin function S_i (S_f) in terms of the usual Dirac matrices α and β for the composite system is given by [42]

$$S_{i(f)}(1,2;3) = \frac{1}{\sqrt{2}}\alpha_3(\alpha_1\beta_2 - \alpha_2\beta_1). \tag{7}$$

Substituting $S_{i(f)}$ in eq. (5) and carrying out the spin integrations using the orthogonal

$$\langle\beta_i|\beta_j\rangle = \delta_{ij}, \tag{8}$$
$$\langle\alpha_i|\beta_j\rangle = 0,$$

we get

$$T_{if_\mathrm{M}} = T^{\mathrm{d}}_{if_\mathrm{M}} - \delta_{Z'-1}T^{\mathrm{ex}}_{if_\mathrm{M}}. \tag{9}$$

In equation (9) $T^{\mathrm{d}}_{if_\mathrm{M}}$ and $T^{\mathrm{ex}}_{if_\mathrm{M}}$ are the spin averaged direct and exchange T-matrices expressed as

$$T^{\mathrm{d}}_{if_\mathrm{M}} = \int F^{-*}(\mathbf{k}_f, \mathbf{r}_3)\psi^*_{f_\mathrm{M}}(\mathbf{r}_1, \mathbf{r}_2)(V - U_f(r_3))F^{+}(\mathbf{k}_i, \mathbf{r}_3)\psi_i(\mathbf{r}_1, \mathbf{r}_2)\mathrm{d}\mathbf{r}_1\mathrm{d}\mathbf{r}_2\mathrm{d}\mathbf{r}_3, \tag{10}$$

$$T^{\mathrm{ex}}_{if_\mathrm{M}} = \int F^{-*}(\mathbf{k}_f, \mathbf{r}_3)\psi^*_{f_\mathrm{M}}(\mathbf{r}_1, \mathbf{r}_2)(V - U_f(r_3))F^{+}(\mathbf{k}_i, \mathbf{r}_1)\psi_i(\mathbf{r}_3, \mathbf{r}_2)\mathrm{d}\mathbf{r}_1\mathrm{d}\mathbf{r}_2\mathrm{d}\mathbf{r}_3. \tag{11}$$

Thus the differential cross section for the singlet-singlet SS excitations is given by

$$\left|\frac{\mathrm{d}\sigma}{\mathrm{d}\Omega}\right|_{\mathrm{SS}} = \frac{1}{4\pi^2}\sum_{\mathrm{M}}\frac{k_f}{k_i}[|T^{\mathrm{d}}_{if_\mathrm{M}} - \delta_{Z',-1}T^{\mathrm{ex}}_{if_\mathrm{M}}|^2]. \tag{12}$$

2.3 *Singlet-triplet excitations* ($1^1S - 3^3P$ *and* 3^3D)

In the singlet-triplet excitations the scattering takes place in the doublet mode, i.e. in this mode also the total spin of the composite system $S = 1/2$. This is because of the conservation of the total spin of the system during the excitation process. The expressions for S_i and S_f in the ST excitation are given by

$$S_i = \frac{1}{\sqrt{2}}\alpha_3[\alpha_1\beta_2 - \alpha_2\beta_1], \tag{13}$$

$$S_f = \frac{1}{\sqrt{6}}[2\alpha_1\alpha_2\beta_3 - \alpha_3(\alpha_1\beta_2 + \alpha_2\beta_1)]. \tag{14}$$

On substituting these in the T-matrix (equation (5)) and carrying out the spin integrations we get

$$T_{if_\mathrm{M}} = \sqrt{3}\delta_{Z',-1}T^{\mathrm{ex}}_{if_\mathrm{M}}. \tag{15}$$

Here, the direct transition matrix $T^{\mathrm{d}}_{if_\mathrm{M}}$ does not appear because the ST excitation cannot take place without an interchange of the projectile and target electron. Also note that ST excitations are therefore not possible by positron impact.

Consequently the differential cross section for the ST excitation in helium atom is given by

$$\left|\mathrm{d}\sigma\right| \quad 1 \quad \sum \frac{k_f}{} |\sqrt{3}\delta \quad T^{\mathrm{ex}}|^2$$

used for the bound states of the target helium atom. These are the one configuration variational wave functions derived and used by Winter and Lin [43]. The ground state 1^1S wave function for helium is given by

$$\phi(1^1S|\mathbf{r}_1,\mathbf{r}_2) = u_0(\mathbf{r}_1)u_0(\mathbf{r}_2) \tag{17}$$

with

$$u_0(\mathbf{r}) = R_0(r)Y_{00}(\hat{r}), \tag{18}$$

where

$$R_0(r) = A\mathrm{e}^{-\alpha_1 r} + B\mathrm{e}^{-\alpha_2 r}. \tag{19}$$

The constant A, B, α_1 and α_2 can be obtained from Winter and Lin [43]. Further, the $n^{1,3}L$ states are having the following form

$$\phi(n^{1,3}LM|\mathbf{r}_1,\mathbf{r}_2) = \frac{1}{\sqrt{2}}\{u_2(n^{1,3}LM|\mathbf{r}_1)u_1(Z|\mathbf{r}_2) + u_1(Z|\mathbf{r}_1)u_2(n^{1,3}LM|\mathbf{r}_2)\} \tag{20}$$

with

$$u_1(Z|\mathbf{r}) = R_1(r)Y_{00}(\hat{r}) \tag{21}$$

and

$$u_2(n^{1,3}LM|\mathbf{r}) = R_2(n^{1,3}L|r)Y_{LM}(\hat{r}), \tag{22}$$

where

$$R_1(r) = 2Z^{3/2}\exp(-Zr) \tag{23}$$

and

$$R_2(n^{1,3}L|r) = N(n^{1,3}L)r^L\exp[-b(n^{1,3}L)r]\sum_{K=1}^{n-L}(-1)^{K-1}c(n^{1,3}L,K)r^{K-1}, \tag{24}$$

with $Z = 2$. The parameters b, c and N occurring in u_2 have been taken from the paper of Winter and Lin [43]. The helium wavefunctions $\phi(n^3L|\mathbf{r}_1,\mathbf{r}_2)$ for all n are orthonormalized to each other and to the ground state $\phi(1^1S|\mathbf{r}_1,\mathbf{r}_2)$. Further all the one-electron wavefunctions $u_2(n^{1,3}L|\mathbf{r})$ have been set orthonormalized to one another and to the wave functions $u_0(\mathbf{r})$ and $u_1(Z|\mathbf{r})$.

2.5 *Choice of distorting potential*

For the calculation of the distorted waves (using eq. (4)), the distortion potential $U_{i(f)}$ is taken as the sum of the spherical average of static potential $\langle\phi_a|V|\phi_a\rangle$, exchange distortion potential and the polarization potential i.e.

$$U_{i(f)} = V_a^{\mathrm{stat}} + \delta_{Z',-1}V_{i(f)}^{\mathrm{ex}} + V_{i(f)}^{\mathrm{pol}} \quad (\text{with } a = i \text{ or } f). \tag{25}$$

$$V_a^{\mathrm{stat}}(r_3)=\begin{cases} Z'\left[\frac{2}{r_3}-2\int_0^{\infty}\frac{|R_0(r_1)|^2}{\max(r_1,r_3)}\,r_1^2\,\mathrm{d}r_1\right] & (\text{for } 1^1S \text{ state}) \\ Z'\left[\frac{2}{r_3}-\int_0^{\infty}\frac{|R_1(r_1)|^2}{\max(r_1,r_3)}\,r_1^2\,\mathrm{d}r_1\right. & \\ \left.\qquad -\int_0^{\infty}\frac{|R_2(r_2)|^2}{\max(r_2,r_3)}\,r_2^2\,\mathrm{d}r_2\right] & (\text{for } n^{1,3}L \text{ state}). \end{cases} \tag{26}$$

$V_{i(f)}^{\mathrm{exch}}$ is the exchange distortion potential in the initial (final) channel and is taken to be that of Furness and McCarthy [44]

$$V_{i(f)}^{\mathrm{exch}}(r_3)=\tfrac{1}{2}\{(\tfrac{1}{2}k_{i(f)}^2-V_a^{\mathrm{stat}}(r_3))-[(\tfrac{1}{2}k_{i(f)}^2-V_a^{\mathrm{stat}}(r_3))^2-8\pi\tau\rho_a(r_3)]^{1/2}\}. \tag{27}$$

Here $\rho_a(r)=\int|\phi_a(\mathbf{r},\mathbf{r}')|^2\mathrm{d}\mathbf{r}'$ is the spherical average of the one electron charge density of the helium atom in the initial or final channel. The value of the parameter τ depends on the total spin of the colliding system and is taken from the paper of Vučić *et al* [45]. For the channel $e-$He (n^3L) it takes -1 for the doublet system and $+2$ for the quartet one. For $e+$ He (n^1L), $\tau=1$. To obtain V_a^{stat} and ρ_a we use the same target wave function as for the evaluation of the T-matrix. $V_{i(f)}^{\mathrm{pol}}$ is the polarization potential and is taken as the widely used simple Buckingham type polarization potential proposed by Jhanwar and Khare [46] having the form

$$V_j^{\mathrm{pol}}=\frac{-\alpha_d r^2}{2(r^2+d^2)^3}, \tag{28}$$

where α_d is the static dipole polarizability of the atom in the jth state (see Miller and Bedersen [47]). The parameter d is taken from the paper of Mittleman and Watson [48] and is given by

$$d=(\tfrac{1}{2}\alpha_d\beta^2Z^{-1/3})^{1/4} \tag{29}$$

with $\beta=1$. Usually β is considered as an adjustable (energy dependent) parameter which is determined by comparing with experimental data. Many workers (see *e.g.* Furness and McCarthy [44] and Verma *et al* [4]) took the adequate value of β such that the experimental cross section for small scattering angles (where polarization is important) can be produced fairly accurately. Since the experimental data were not sufficiently available for all the excitations and to be consistent we took β to be energy independent and equal to unity as recommended by Mittleman and Watson [48].

Similar to our previous papers [3–5] three different choices of the distortion potential are made for the present study also, that is the distortion potential of either the ground state (II) or excited state (FF) is taken in both the initial and final channels, or the distortion of the initial state in the initial channel and of the excited state in the final channel

Blum [49] gave explicit expressions for the Stokes intensities in terms of the state multipoles $\langle T(L)^{+}_{KQ}\rangle$ for the photons emitted in direction $(\theta_\gamma, \phi_\gamma)$ in coincidence with the scattered electrons after impact excitation of an atomic state with orbital angular momentum L and an electric dipole transition to a state with orbital angular momentum L_2 in the 'collision frame of reference' as

$$\begin{aligned}I = {} & \frac{C(\omega)}{\gamma}|\langle L_2\|\mathbf{r}\|L\rangle|^2(1)^{L+L_2}\left[\frac{2(-1)^{L+L_2}G_0(L)\langle T(L)^{+}_{00}\rangle}{3(2L+1)^{1/2}} - \begin{Bmatrix}1 & 1 & 2\\ L & L & L_2\end{Bmatrix}\right.\\ & \times\left(G_2(L)\langle T(L)^{+}_{22}\rangle \times \sin^2\theta_\gamma\cos 2\phi_\gamma - G_2(L)\langle T(L)^{+}_{21}\rangle\sin 2\theta_\gamma\cos\phi_\gamma\right.\\ & \left.\left.+\frac{G_2(L)\langle T(L)^{+}_{20}\rangle(3\cos^2\theta_\gamma - 1)}{\sqrt{6}}\right)\right],\end{aligned} \tag{30}$$

$$\begin{aligned}I\eta_3 = {} & \frac{C(\omega)}{\gamma}|\langle L_2\|\mathbf{r}\|L\rangle|^2(-1)^{L+L_2}\begin{Bmatrix}1 & 1 & 2\\ L & L & L_2\end{Bmatrix}\\ & \times[G_2(L)\langle T(L)^{+}_{22}\rangle(1+\cos^2\theta_\gamma)\cos 2\phi_\gamma + G_2(L)\langle T(L)^{+}_{21}\rangle\sin 2\theta_\gamma\cos\phi_\gamma\\ & + \sqrt{3/2}G_2(L)\langle T(L)^{+}_{20}\rangle\sin^2\theta_\gamma],\end{aligned} \tag{31}$$

$$\begin{aligned}I\eta_1 = {} & \frac{-C(\omega)}{\gamma}|\langle L_2\|\mathbf{r}\|L\rangle|^2(-1)^{L+L_2}\begin{Bmatrix}1 & 1 & 2\\ L & L & L_2\end{Bmatrix}\\ & \times[G_2(L)\langle T(L)^{+}_{22}\rangle 2\cos\theta_\gamma\sin 2\phi_\gamma + G_2(L)\langle T(L)^{+}_{21}\rangle 2\sin\theta_\gamma\sin\phi_\gamma],\end{aligned} \tag{32}$$

$$-I\eta_2 = \frac{-C(\omega)}{\gamma}|\langle L_2\|\mathbf{r}\|L\rangle|^2(-1)^{L+L_2}\begin{Bmatrix}1 & 1 & 1\\ L & L & L_2\end{Bmatrix}2iG_1(L)\langle T(L)^{+}_{11}\rangle\sin\theta_\gamma\sin\phi_\gamma, \tag{33}$$

where $C(\omega) = (\omega^4/2\pi c^3)$ is a constant containing the frequency ω of the transition, γ is the decay constant and $|\langle L_2\|\mathbf{r}\|L\rangle|^2$ is related to the oscillator strength of the radiative transition. $G_K(L)$ are the depolarization perturbation coefficients which account for the fine structure of the final excited state and are given by

$$G_K(L) = \frac{1}{(2S+1)}\sum_J (2J+1)^2\begin{Bmatrix}L & J & S\\ J & L & K\end{Bmatrix}^2, \tag{34}$$

where S is the electronic spin and $J = L + S$ is the total angular momentum of the atom. The $G_K(L)$ are normalized such that $G_0(L) = 1$ for all L.

$$\langle T(L)_{KQ}\rangle = \sum_{M'M} (-1) \quad (2K+1) \begin{pmatrix} & & \\ M' & -M & -Q \end{pmatrix} \langle a(M')a(M)\rangle, \qquad (35)$$

where

$$\langle a(M')a(M)^*\rangle = \frac{1}{2(2S_i+1)} \sum_{s} (2S+1)a(M')^s a(M)^{s*}. \tag{36}$$

Here $a(M)^s$ is the scattering amplitude for excitation of the magnetic substate M in the channel with total spin S and S_i is the spin of the initial target state. From the properties of the $3j$ symbol the values of rank K and component Q of the multipoles are restricted as follows:

$$K \leq 2L \quad \text{and} \quad -Q \leq K \leq Q.$$

The state multipole $\langle T(L)^+_{00}\rangle$ is a measure of the overall population of the atomic state and can be expressed in terms of the differential cross section σ as

$$\langle T(L)^+_{00}\rangle = \frac{\sigma}{(2L+1)^{1/2}}. \tag{37}$$

Further we see from equations (30–33) that $\langle T(L)^+_{1Q}\rangle$ describes the orientation of the state and thus the circular polarization of the emitted photons and the state multipole $\langle T(L)^+_{2Q}\rangle$ describes the alignment of the atomic state and thus gives the anisotropic part of the coincidence rate and the linear polarization of the emitted photon. Also note that for dipole transitions it is impossible to achieve state multipoles with rank $K > 2$ since a single photon has an angular momentum of unity.

The differential Stokes parameters for scattering of unpolarized atoms by unpolarized electrons P_i ($i = 1$–3) measured perpendicular to the scattering plane ($\theta_\gamma = \phi_\gamma = 90°$) are

$$P_1 = \frac{I(0°) - I(90°)}{I(0°) + I(90°)}, \tag{38}$$

$$P_2 = \frac{I(45°) - I(135°)}{I(45°) + I(135°)}, \tag{39}$$

$$P_3 = \frac{I(\mathrm{RHC}) - I(\mathrm{LHC})}{I(\mathrm{RHC}) + I(\mathrm{LHC})}. \tag{40}$$

Further, the Stokes parameter P_4 is measured parallel to the scattering plane ($\theta_\gamma = 90°$, $\phi_\gamma = 0°$) and is given by

$$P_4 = \frac{I(0°) - I(90°)}{I(0°) + I(90°)}, \tag{41}$$

where $I(\alpha°)$ is the intensity of the light with the polarization vector in the α direction with respect to the incident projectile direction and I (RHC) and I (LHC) are, respectively, the intensities of the right and left circularly polarized light components.

Thus using equations (30–33) the Stokes parameters P_i (i = 1, 2 and 3) for any $L \rightarrow L_2$

$$P_1 = \frac{1}{I^y}\begin{Bmatrix}1 & 1 & 2\\ L & L & L_2\end{Bmatrix}\left[\sqrt{\frac{3}{2}}G_2(L)\langle T(L)^{+}_{20}\rangle - G_2(L)\langle T(L)^{+}_{22}\rangle\right], \tag{42}$$

$$P_2 = -\frac{1}{I^y}\begin{Bmatrix}1 & 1 & 2\\ L & L & L_2\end{Bmatrix}[2G_2(L)\langle T(L)^{+}_{21}\rangle], \tag{43}$$

$$P_3 = \frac{1}{I^y}\begin{Bmatrix}1 & 1 & 1\\ L & L & L_2\end{Bmatrix}[2iG_1(L)\langle T(L)^{+}_{11}\rangle], \tag{44}$$

and the Stokes parameter $P_4(\theta_\gamma = 90°,\ \phi_\gamma = 0°)$ for the same decay is expressed as

$$P_4 = \frac{1}{I^x}\begin{Bmatrix}1 & 1 & 2\\ L & L & L_2\end{Bmatrix}\left[\sqrt{\frac{3}{2}}G_2(L)\langle T(L)^{+}_{20}\rangle + G_2(L)\langle T(L)^{+}_{22}\rangle\right], \tag{45}$$

where

$$\begin{aligned} I^y = & \frac{2(-1)^{L+L_2}}{3(2L+1)^{1/2}}G_0(L)\langle T(L)^{+}_{00}\rangle + \begin{Bmatrix}1 & 1 & 2\\ L & L & L_2\end{Bmatrix} \\ & \times\left[\frac{G_2(L)}{\sqrt{6}}\langle T(L)^{+}_{20}\rangle + G_2(L)\langle T(L)^{+}_{22}\rangle\right] \end{aligned} \tag{46}$$

and

$$\begin{aligned} I^x = & \frac{2(-1)^{L+L_2}}{3(2L+1)^{1/2}}G_0(L)\langle T(L)^{+}_{00}\rangle + \begin{Bmatrix}1 & 1 & 2\\ L & L & L_2\end{Bmatrix} \\ & \times\left[\frac{G_2(L)}{\sqrt{6}}\langle T(L)^{+}_{20}\rangle - G_2(L)\langle T(L)^{+}_{22}\rangle\right]. \end{aligned} \tag{47}$$

Further, to describe the nascent charge cloud of the atom immediately after excitation Andersen *et al* [38] defined the parameters which can be related to the Stokes parameters. These are the alignment angle, γ, linear polarization, P_l, height of charge cloud, ρ_{00}, and the angular momentum transferred perpendicular to the scattering plane, $L_\perp$. In this paper we have considered excitation from the ground 1^1S state to higher $3^{1,3}P$ and $3^{1,3}D$ states of helium which decay by photon emission to lower allowed $2^{1,3}S$ and $2^{1,3}P$ states respectively and for such cases the parameters defined by Andersen *et al* [38] are related to the Stokes parameters by the following relations

$$\gamma = \tfrac{1}{2}\arg(\bar{P}_1 + i\bar{P}_2), \tag{48}$$

$$P_l = (\bar{P}_1^2 + \bar{P}_2^2)^{1/2}, \tag{49}$$

$$L_\perp = -P_3\left(\frac{2L}{2+\kappa}\right) \tag{50}$$

and

$$(1+P_4)$$

Here $\bar{P}_1$, $\bar{P}_2$, $\bar{P}_3$, and $\bar{P}_4$, are the reduced Stokes parameters which may be obtained by using the same relations as for measured Stokes parameters P_1, P_2, P_3 and P_4 given by equations (42–47) but with all $G_k(L)$ taken as unity.

For the sake of clarity we also give below the simplified explicit expressions of the Stokes parameters for the various excitations considered in this paper.

2.6.1 *For* $3^{1,3}P$ *excitation*: The excited 3^1P and 3^3P states after excitation decay by dipole transition by photons to the lower S states viz. to 2^1S and 2^3S states. In this case $L=1$ and $L_2=0$, therefore, the Stokes parameters are given as

$$P_1 = \frac{1}{I^y}\frac{1}{3}\left[\sqrt{\frac{3}{2}}G_2\langle T(3P)^{+}_{20}\rangle - G_2\langle T(3P)^{+}_{22}\rangle\right], \tag{53}$$

$$P_2 = \frac{-1}{I^y}\frac{1}{3}[2G_2\langle T(3P)^{+}_{21}\rangle], \tag{54}$$

$$P_3 = \frac{-1}{I^y}\frac{1}{3}[2iG_1\langle T(3P)^{+}_{11}\rangle]. \tag{55}$$

Here

$$I^y = \frac{-2}{3\sqrt{3}}G_0\langle T(3P)^{+}_{00}\rangle + \frac{1}{3}\left[\frac{G_2}{\sqrt{6}}\langle T(3P)^{+}_{20}\rangle + G_2\langle T(3P)^{+}_{22}\rangle\right] \tag{56}$$

and the depolarization coefficients are given by

$G_0 = G_1 = G_2 = 1$ for 3^1P state of helium,
$G_0 = 1, G_1 = \frac{1}{2},\ G_2 = \frac{15}{54}$ for 3^3P state of helium.

In addition to the above defined parameters (eqs (48–54)), Donnelly *et al* [28] and Humphrey *et al* [27] for 3^3P excitation have also reported experimental data for the angular correlation function N i.e. the angular distribution of the coincidence photons which are collected in collision scattering plane. The expression for which can be obtained from equation (34) by taking $\phi_\gamma = 0$. However, in terms of the well known λ and χ parameters after allowing for the depolarization of the decay radiation due to the fine-structure interaction among the triplet states this can be written as

$$N = \lambda\left(\frac{41}{54} - \frac{5}{18}\cos^2\theta_\gamma\right) + \frac{1}{2}(1-\lambda)\left(\frac{67}{54} + \frac{5}{18}\cos 2\theta_\gamma\right) - \frac{5}{18}[\lambda(1-\lambda)]^{1/2}\cos\chi\sin 2\theta_\gamma\,, \tag{57}$$

where

$$\lambda = (a_0^2/(a_0^2 + 2a_1^2)) \tag{58}$$

and

$L = 2$, $L_2 = 1$ in equations (42–47) the Stokes parameter for a ${}^{1,3}D \rightarrow {}^{1,3}P$ de-excitation process can be expressed in terms of state multipoles $\langle T(3D)^{+}_{KQ}\rangle$ as

$$P_1 = \frac{1}{I^y}\frac{1}{10}\sqrt{\frac{7}{3}}\left[\sqrt{\frac{3}{2}}\langle T(3D)^{+}_{20}\rangle - G_2\langle T(3D)^{+}_{22}\rangle\right], \tag{60}$$

$$P_2 = \frac{-1}{I^y}\frac{1}{10}\sqrt{\frac{7}{3}}[2G_2\langle T(3D)^{+}_{21}\rangle], \tag{61}$$

$$P_3 = \frac{-1}{I^y}\frac{1}{\sqrt{5}}[iG_1\langle T(3D)^{+}_{11}\rangle], \tag{62}$$

$$P_4 = \frac{1}{I^x}\frac{1}{10}\sqrt{\frac{7}{3}}\left[\sqrt{\frac{3}{2}}G_2\langle T(3D)^{+}_{20}\rangle + G_2\langle T(3D)^{+}_{22}\rangle\right], \tag{63}$$

where

$$I^y = \frac{-2}{3\sqrt{5}}G_0\langle T(3D)^{+}_{00}\rangle + \frac{1}{10}\sqrt{\frac{7}{3}}\left[\frac{G_2}{\sqrt{6}}\langle T(3D)^{+}_{20}\rangle + G_2\langle T(3D)^{+}_{22}\rangle\right] \tag{64}$$

and

$$I^x = \frac{-2}{3\sqrt{5}}G_0\langle T(3D)^{+}_{00}\rangle + \frac{1}{10}\sqrt{\frac{7}{3}}\left[\frac{G_2}{\sqrt{6}}\langle T(3D)^{+}_{20}\rangle - G_2\langle T(3D)^{+}_{22}\rangle\right] \tag{65}$$

such that

$G_0 = G_1 = G_2 = 1$ for 3^1D state of helium,
$G_0 = 1, G_1 = \frac{43}{54}, G_2 = \frac{71}{150}$ for 3^3D state of helium.

3. Results and discussion

Using the distorted wave approximation method as described in earlier section the results are obtained for differential cross sections, Stokes parameters and alignment and orientation parameters for the $3^{1,3}P$ and $3^{1,3}D$ excitation in helium from the ground 1^1S state. We have carried out calculations for both electron and positron impact excitations in the energy range 40 to 100 eV. The DWA calculations are carried out in all the four versions i.e. II, IF and FF and IIP. Although as mentioned earlier there are number of calculations available we have compared our various results only with the largely available FOMBT and the accurate convergent close coupling (CCC) calculations for sake of clarity and consistency. We have not made here comparisons of our results available with the distorted wave Born approximation calculations of Madison and co-workers [6–8] and Katiyar and Srivastava [9] as our results are found to be within

Since the individual excitation of the 3^1P, 3^1D and 3^3D states could not be resolved earlier the combined measurements of the differential cross sections were reported. In figure 1 we therefore present the DCS for the combined He $(3^1P + 3^1D + 3^3D)$ excitation at incident electron energies of 40, 50, 60 and 100 eV. These are compared with the available CCC results of Fursa and Bray [15] and the FOMBT results of Cartwright *et al* [11] at 40, 50 and 100 eV electron energies. They are also compared with measurements of Chutijian and Thomas [10] at 40 eV and of Trajmar [11] at 50 eV and 100 eV. At 40 eV our DWA results obtained using the II and IIP versions alongwith FOMBT and CCC calculations are in good agreement with the experimental results only upto scattering angle of 60°. At 50 eV our DWA results in the FF model are in over all the best agreement with the experimental data though the other DWA calculations (i.e. in II, IF, IIP models), CCC and FOMBT also agree well with the experimental data below scattering angle of 50°. At 60 eV only our calculations are available which show similar features as at 50 eV. Finally, at 100 eV being the high energy as expected all the calculations agree closely almost upto scattering angle of 120° with themselves and with experiment.

In figure 2 we present our DWA results as compared with other results for the individual 3^1P excitation at 40 and 80 eV. At these energies Khakoo *et al* [1] have reported recently the experimental DCS by direct measurement. In this figure, we included the experimental data of Khakoo *et al* [1] and the CCC and FOMBT calculations. From the figure we see that at 40 eV our II and IIP results are the closest to the experimental data while at 80 eV except our IF model all other models give results which are in reasonable agreement with available experimental and other theoretical results over the entire scattering angle range.

In figure 3 the DCS results for excitation of the $M_f = 0$ substate of the 3^1P state are shown at 70 eV energy. These are compared with the directly measured relative DCS of Hummer and Burns [13] and the FOMBT calculations of Csanak *et al* [14]. Our DWA results obtained using the FF model are in reasonably good agreement with the experimental data. Note that the relative DCS of Hummer and Burns [13] have been normalized, in a manner similar to the one used by Csanak *et al* [14] to our DWA results in the FF model at scattering angle of 10°. In figures 4, 5 the DCS results for the excitation of the different magnetic substates (i.e. $M_f = 0, \pm 1$) of the 3^1P state are presented at 50, 80 and 100 eV energies. These are compared with the only available FOMBT calculations of Csanak *et al* [14] as well as with the estimated experimental data obtained utilizing the λ parameters and the DCS as explained and tabulated in their paper. Comparing the results for $M_f = 0$ in figure 4 we find our FF model results are in the best agreement with the experimental data at 50 eV whereas the FOMBT results lie in between our II and IIP calculations and differ from FF results. At 80 and 100 eV the different theoretical results have come closer and the experimental data lie in between FF and other calculations. In figure 5, the results are presented for DCS for $3^1P(M_f = 1)$ excitation. From this figure we see that our different DWA results at 50 eV compare well with the available experimental and FOMBT results below scattering angle of 60°. Beyond 60° the experimental data tend to lie above the various theoretical results. Further, on comparing the different

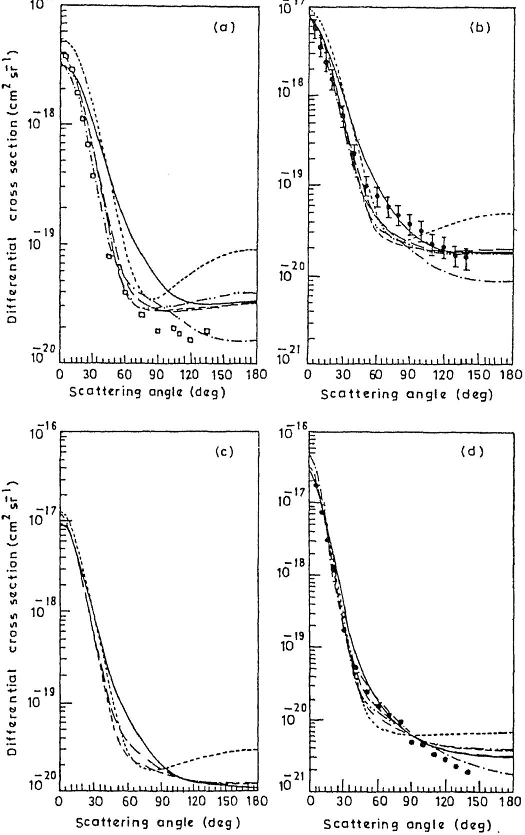
(a)
(b)
(c)
(d)
Differential cross section (cm^2 sr^{-1})
10^{-16}
10^{-17}
10^{-18}
10^{-19}
10^{-20}
10^{-21}
0
30
60
90
120
150
180
Scattering angle (deg)

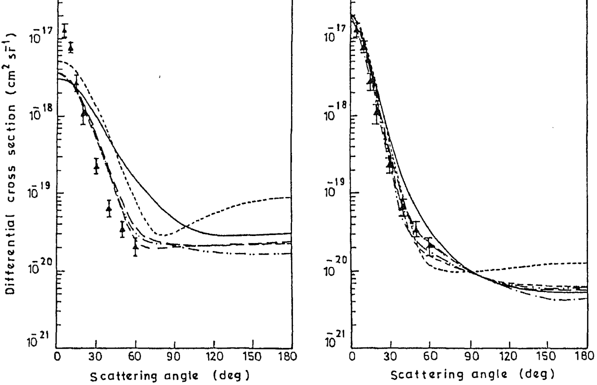

Figure 2. Differential cross section in units of cm^{2}sr^{-1} for the electron impact 1^1S–3^1P excitation in helium at E_i = (**a**) 40 eV and (**b**) 80 eV. ———— present FF results; ------- present IF results; – – – – – present II results; — — — present IIP results; -••-•• FOMBT results of Cartwright *et al* [11]; -•-•- CCC results of Fursa and Bray [15]; ▲ experimental data of Khakoo *et al* [1].

results for $M_f = 0$ and for $M_f = 1$ shows that their nature are entirely different which on combining finally show the behaviour of $M_f = 0$ (see figures 1 and 4).

In figures 6, 7 and 8 we present the Stokes parameters P_1, P_2 and P_3 for the decay of photons from 3^1P state to 2^1S state which we calculated using equations (53–56). In these figures the parameters of Andersen *et al* [38] (viz. P_l, $L_\perp$ and γ) for the excited 3^1P state obtained using equations (48–50) are also shown. The results are reported at incident electron energy of 50, 80 and 100 eV as most of the experiments and other theoretical calculations have been carried out at these energies.

In figure 6 we compare our various DWA results for Stokes parameters at 50 eV with the measurements of Eminyan *et al* [17]. The agreement between the experiment and theory is good for all Stokes parameters i.e. P_1, P_2 and P_3. As seen for the DCS results out of our different DWA results the FF model calculations are in the overall best agreement with experimental data. Further, the inclusion of the polarization potential in the distortion potential (IIP) also improves the agreement with the experimental data. In this figure the displayed alignment and orientation parameters (viz. P_l, $L_\perp$ and γ) are compared with the CCC calculations [15] and the experimental data of Beijers *et al* [7] and Eminyan *et al* [17]. On comparison for $L_\perp$ results we find our DWA calculations

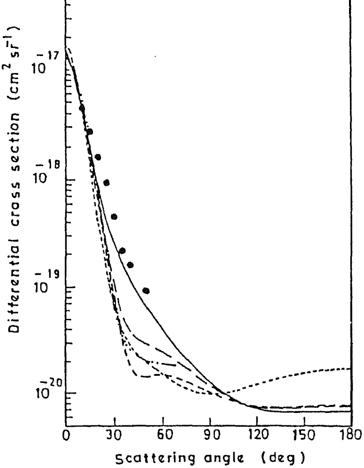

Figure 3. Differential cross section in units of cm^2 sr^{-1} for the electron impact 1^1S–$3^1P(M_f = 0)$ excitation in helium at $E_i = 70$ eV. ———— present FF results; - - - - - - - present IF results; – – – – – present II results; — — — present IIP results; -●●-●●- FOMBT results of Csanak *et al* [14]; ● experimental data of Hummer and Burns [13].

the γ parameter the CCC results alongwith the FF model are in better agreement with the experimental data as compared to other results. For the P_l parameter, again the FF model can be said to work the best in terms of overall agreement with the experimental data alongwith CCC calculations, although the second minimum of the CCC calculation is absent in our DWA results.

In figure 7 the Stokes parameters P_1, P_2 and P_3 at 80 eV are compared with the measurements of Eminyan *et al* [17] and McAdams and Williams [18]. The agreement of the DWA results with the measurements of Eminyan *et al* [17] is good for all the P_1, P_2 and P_3 Stokes parameters. Also the experimental data in the larger scattering region due to McAdams and Williams [18] though agree well with our DWA calculations for P_2 but lie below and above our results respectively for P_1 and P_3 Stokes parameters. Further in this figure the results for $L_\perp$; γ and P_l parameters are compared with the experimental data of Beijers *et al* [7], Eminyan *et al* [17] and McAdams and

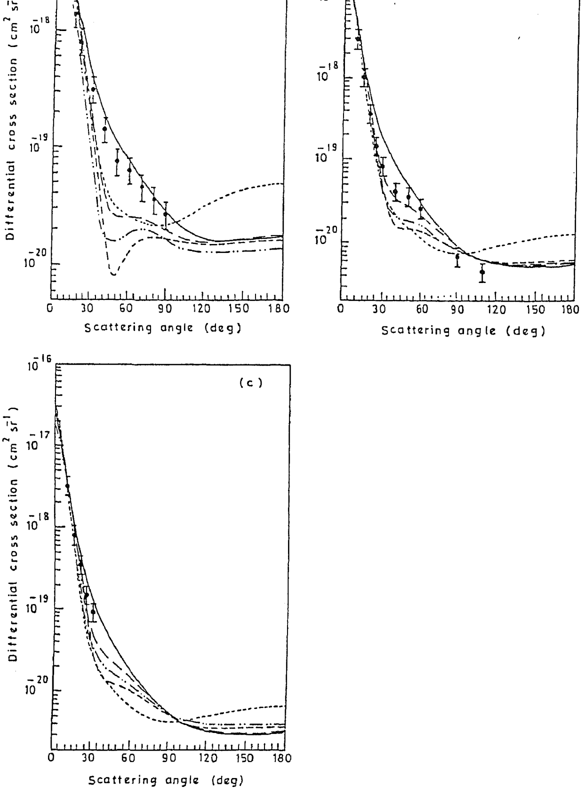

Figure 4. Differential cross section in units of cm^2 sr^{-1} for the electron impact 1^1S–$3^1P(M_f = 0)$ excitation in helium at E_i = (**a**) 50 eV, (**b**) 80 eV, (**c**) 100 eV. ——— present FF results; - - - - - - - present IF results; –·– – – – present II results; — — — present IIP results; -••-••- FOMBT results of Csanak *et al* [14]; • estimated

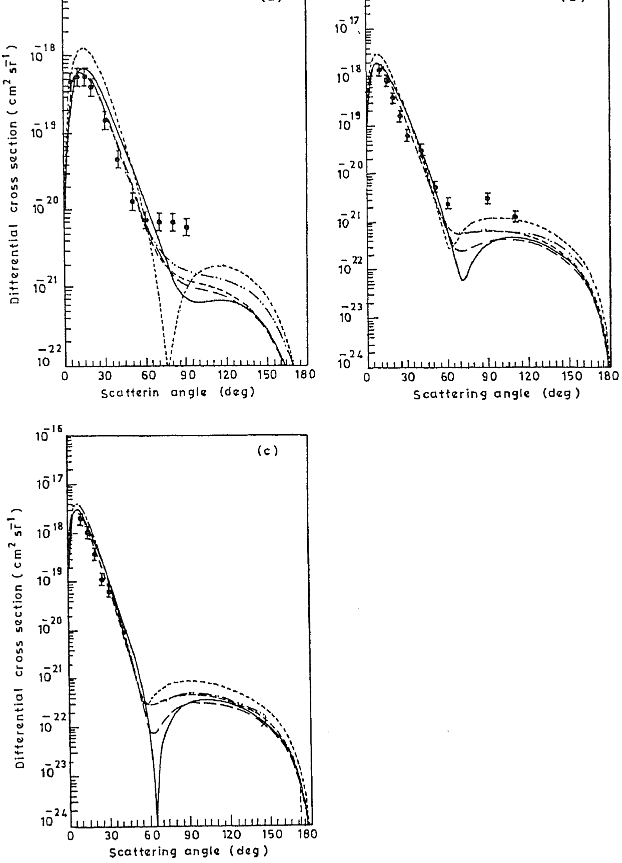

Figure [illegible]. Same as Fig. [illegible] but for electron impact 1^1S-$2^1P(M_L = 1)$ excitation in

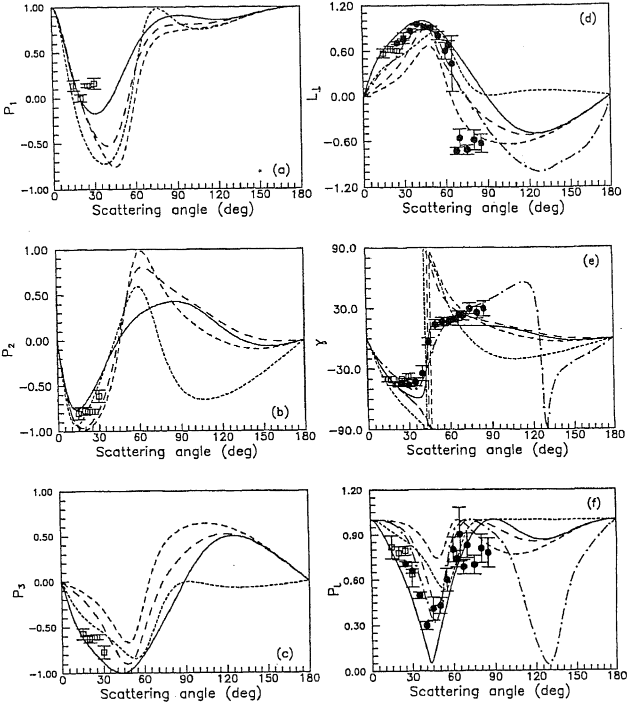

Figure 6. Stokes parameters P_1, P_2 and P_3 and alignment and orientation parameters P_l, γ and $L_\perp$ for electron impact 1^1S–3^1P excitation in helium at $E_i = 50$ eV. ———— present FF results; - - - - - - - present IF results; – – – – – present II results; — — — present IIP results; -•-•- CCC results of Fursa and Bray [15]; □ experimental data of Eminyan *et al* [17]; • experimental data of Beijers *et al* [7].

[19]. Features for these parameters are similar to figure 6. The FOMBT results are

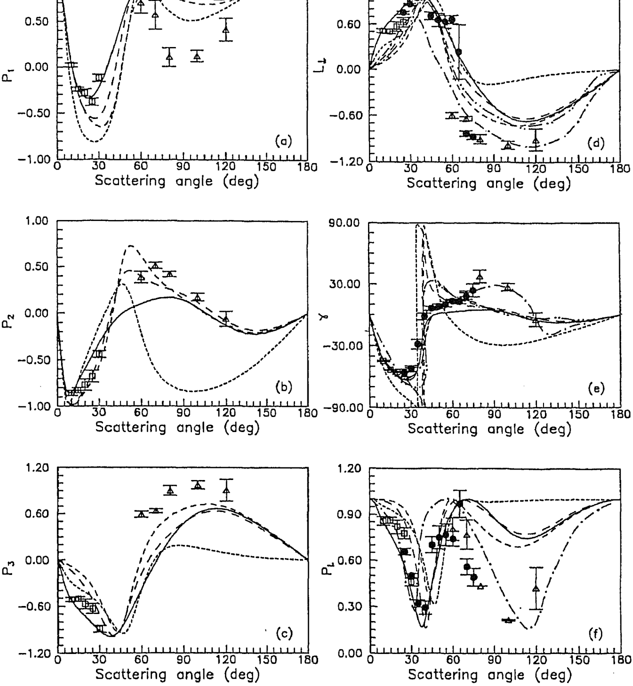

Figure 7. Same as figure 6 but for $E_i = 80\,\text{eV}$ and -••-••-, FOMBT results of Csanak and Cartwright [19]; △, experimental data of McAdams and Williams [18].

Through figures 9–12 results are presented for DCS, Stokes parameters and alignment and orientation parameters for the positron impact $1^1S - 3^1P$ excitation in helium. These results are presented at positron energies of 50 and 100 eV. Since there are no experimental results to compare we have presented only our different results.

Figure 9 shows the DCS in the different II, IF, FF and IIP models at 50 and 100 eV

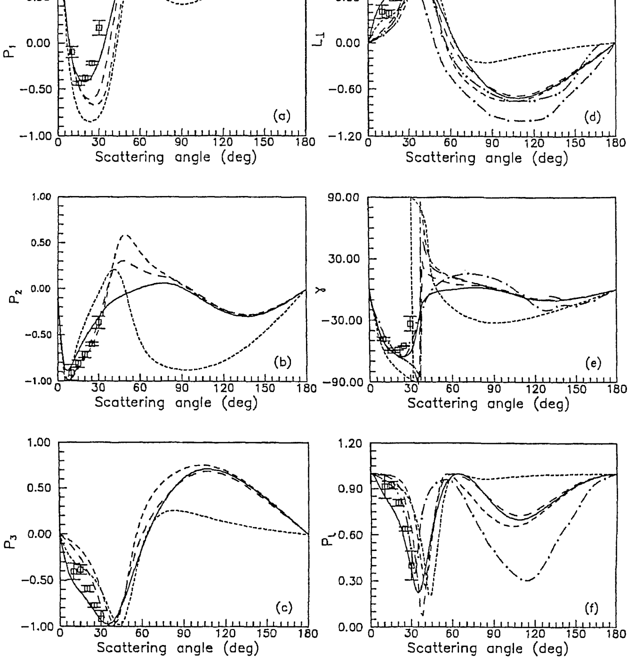

Figure 8. Same as figure 6 but for $E_i = 100\,\text{eV}$ and ·······, FOMBT results of Csanak and Cartwright [19].

corresponding electron-impact results (see figure 1) we find that the results for positron-impact fall off quickly for larger angles as compared to the results for electron-impact excitation. This may be due to absence of exchange contribution in positron-impact results. Rest other features are similar to as for electron-impact case and the positron-impact results are comparable with the electron-impact results. From figure 10 for the $3^1P(M_f = 0)$ excitation, the behaviour is similar to the DCS summed over all magnetic

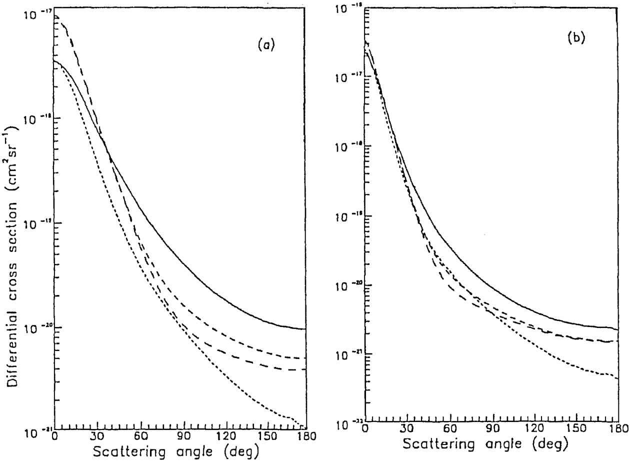

Figure 9. Differential cross section in units of cm^2 sr^{-1} for the positron impact $1^1S - 3^1P$ excitation in helium at $E_i =$ (**a**) 50 eV and (**b**) 100 eV. ———— present FF results; - - - - - - - present IF results; – – – – – present II results; — — — present IIP results.

with the electron-impact results, we find that the minimum in the electron impact results is totally missing here (see figure 4). Thus the presence of the minimum may be said to occur because of the difference in the nature of interaction potentials in both the cases of electron and positron-impact.

In figure 12 for the sake of illustration in case of positron impact, the results at positron impact energy of 50 eV are presented for Stokes parameters (P_1, P_2 and P_3) and alignment and orientation parameters ($L_\perp$, P_l and γ). Again no other results are available for these parameters to compare with our DWA results. The inter-comparison of these results with the corresponding electron impact results (see figure 6) gives the most striking feature that in contrast to the electron impact results, the P_3, $L_\perp$ and γ parameters retain the same sign throughout the angular region. Also the sharp maxima and minima observed in the electron impact case are missing in the different results for positron impact excitation.

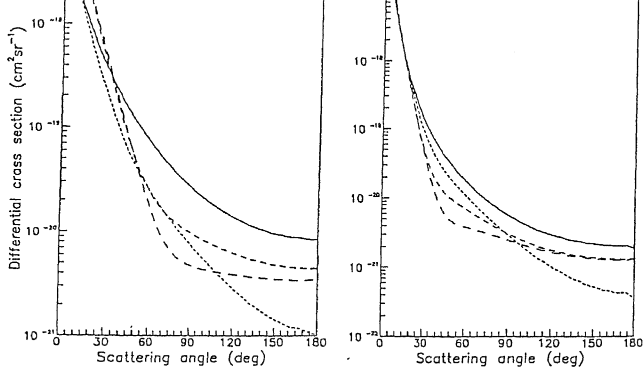

Figure 10. Differential cross section in units of $\mathrm{cm^2\,sr^{-1}}$ for the positron impact 1^1S–$3^1P(M_f = 0)$ excitation in helium at $E_i =$ (**a**) 50 eV and (**b**) 100 eV. Notation same as in figure 9.

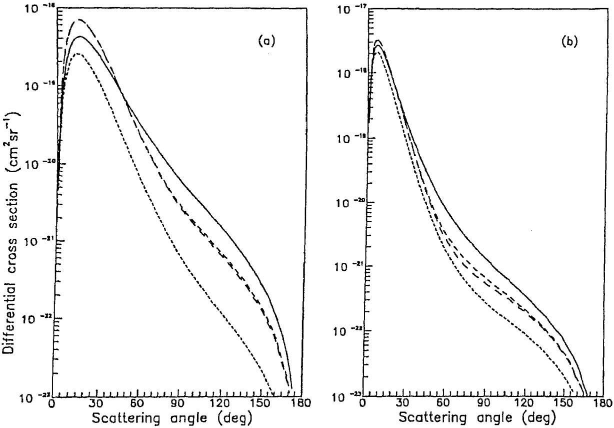

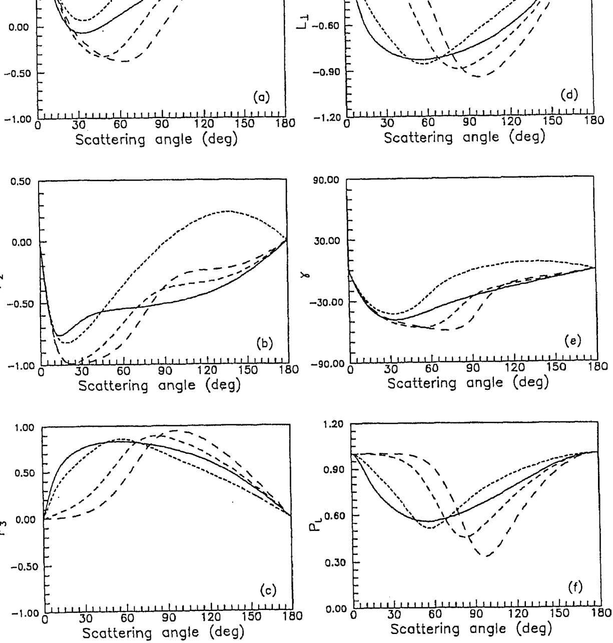

Figure 12. Stokes parameters P_1, P_2 and P_3 and alignment and orientation parameters P_l, γ and $L_\perp$ for positron impact 1^1S-3^1P excitation in helium at $E_i = 50\,\mathrm{eV}$. Notation same as in figure 10.

given. These are compared with the CCC [15] and FOMBT [23] calculations and with experimental data of Chutijian and Thomas [10] Trajmar *et al* [23] and Batelaan *et al* . Since Batelaan *et al* [24] reported relative DCS, we normalized these as best fits to DWA results in the FF model. On comparing the results at 40 eV, the DWA and MBT results tend to lie higher than the experimental data. Also, the CCC results are tively in better agreement with the measurements in the entire angular range. Since

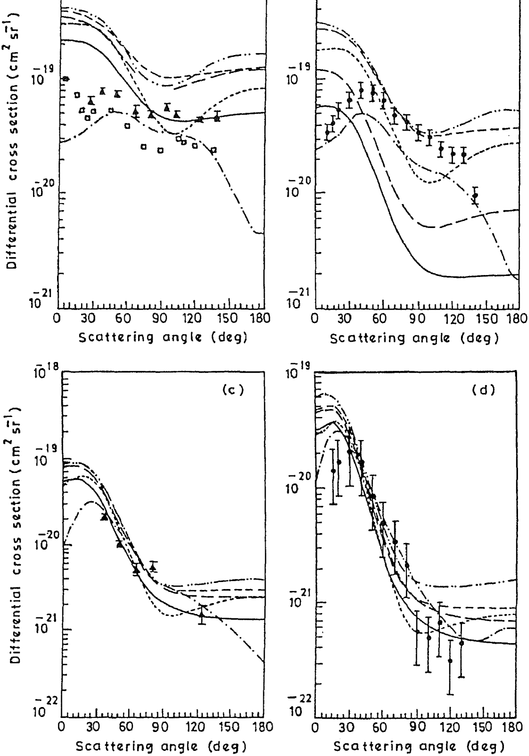

Figure 13. Differential cross section in units of cm^2 sr^{-1} for the electron impact 1^1S–3^3P excitation in helium at E_i = (**a**) 40 eV, (**b**) 50 eV, (**c**) 80 eV and (**d**) 100 eV. ———— present FF results; - - - - - - - present IF results; – – – – – present II results; — — — present IIP results; -••-•• FOMBT results of Trajmar *et al* [23]; -•-•- CCC results of Fursa and Bray [15]; □ experimental data of Chutijian and Thomas [10]; • experimental data of Trajmar *et al* [23]; ▲ relative experimental data of

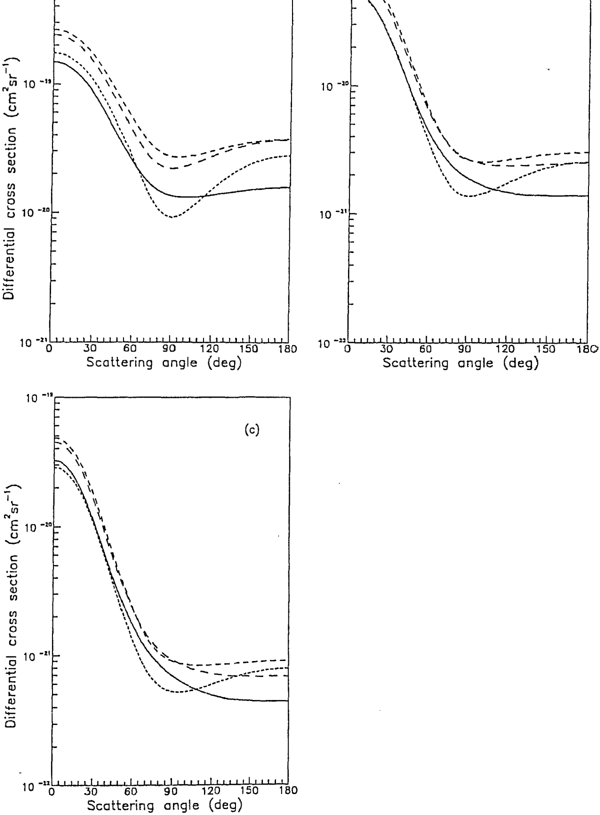

Figure 14. Differential cross section in units of cm^2 sr^{-1} for the electron impact $1^1S - 3^3P$ $(M_f = 0)$ excitation in helium at E_i = (**a**) 50 eV, (**b**) 80 eV and (**c**) 100 eV. ———— present FF results; - - - - - - - present IF results; – – – – – present II

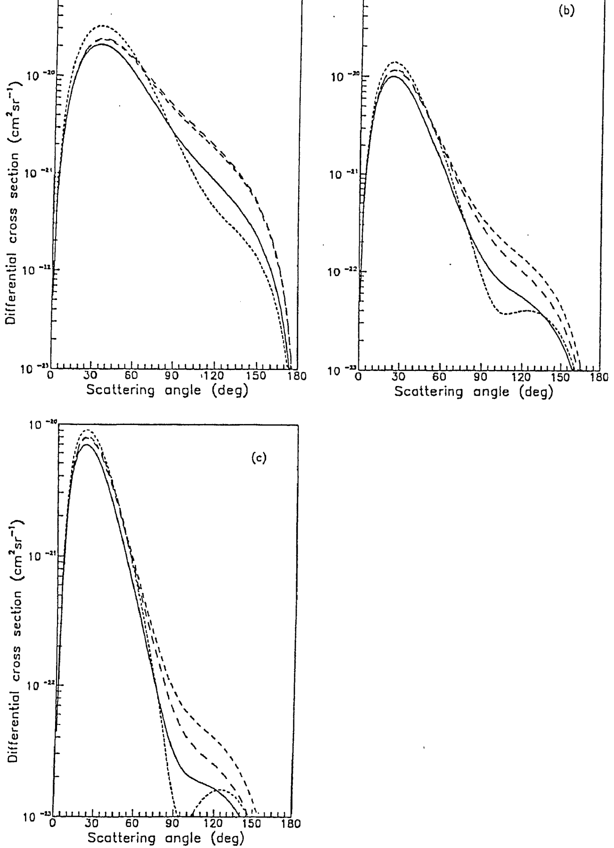

Figure 15. Same as figure 14 but for electron impact 1^1S–3^3P ($M_f = 1$) excitation

nent of our results with both the available experimental data alongwith theoretical ations is reasonably good. Next in figures 14 and 15 we present the magnetic el DCS for the 3^3P excitation in helium at 50, 80 and 100 eV energies. Since no previous DCS data are available for the individual magnetic sublevel we display ur DWA results in all the four models (viz. II, IF, FF and IIP). For the $3^3P(M_f = 0)$ tion the cross sections in the IF model only show a pronounced minimum as red with others. Further, the IIP results lie lower showing that the inclusion of zation potential tends to lower the magnitude of DCS. An interesting feature that noticed for $3^3P(M_f = 1)$ excitation is the very small magnitude of DCS for small and then the appearance of maxima in the scattering angle range of 20–30° which ll off rapidly with the increase of scattering angle. Further, the maximum is shifted ds lower angles and the width of the maximum also decreases with the increase in . Also note that in contrast to the singlet-singlet scattering where all the four s give nearly the same values of DCS at low scattering angles, for the singlet-triplet ing the results obtained by different models (*viz.* II, IF, FF and IIP) differ ciably. The difference in the DCS results for the singlet-singlet ($1^1S - 3^1P$) and t-triplet $1^1S - 3^3P$ transitions can be due to reason that the singlet-triplet transition present system (e + He) is caused only by the electron exchange interaction.

igure 16 we show the coincidence count rate (N) calculated using equation (57) in figures 17 and 18 our DWA calculations respectively at incident electron energies d 60 eV are shown as compared with other available results for Stokes parameters $_2$, P_3 and alignment and orientation parameters ($L_\perp$, γ and P_l). The results in 16 show the coincidence count rate N as a function of photon angle θ_γ. We have our DWA results compared at an energy of 40 eV and scattering angle 60° with the rements of Donnelly *et al* [28] and Humphrey *et al* [27] which have been carried

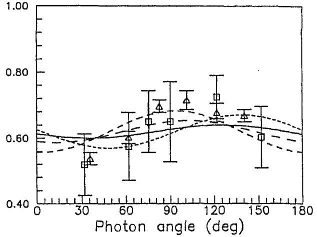

Figure 16. Coincidence count rate N as a function of photon angle for the electron impact 1^1S–3^3P excitation in helium at $E_i = 40$ eV. Same as figure 14 and △ experimental data of Donnelly *et al* [28]; □ experimental data of Humphrey *et al* [27].

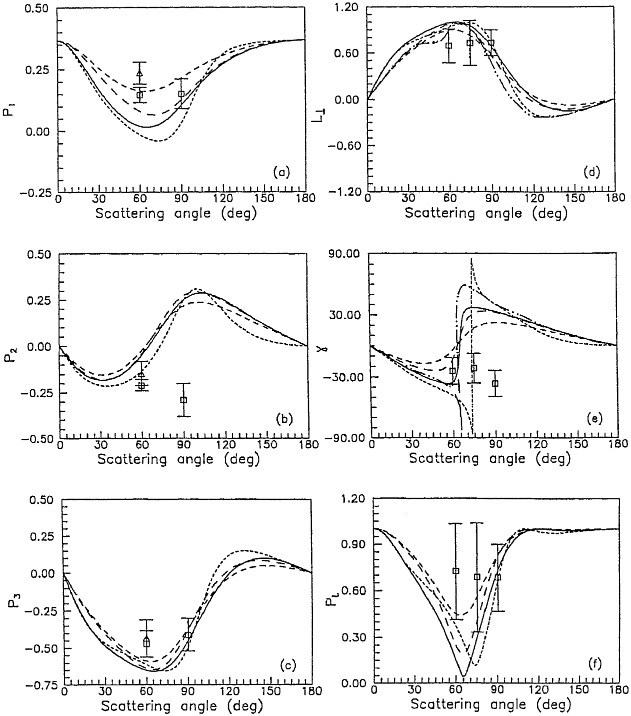

Figure 17. Stokes parameters P_1, P_2 and P_3 and alignment and orientation parameters P_l, γ and $L_\perp$ for electron impact 1^1S–3^3P excitation in helium at $E_i = 40\,\text{eV}$. Notation same as in figure 16 and -·-·-·- FOMBT results of Csanak and Cartwright [29].

out at 39.7 eV energy and 60° scattering angle. From the figure we find that the different

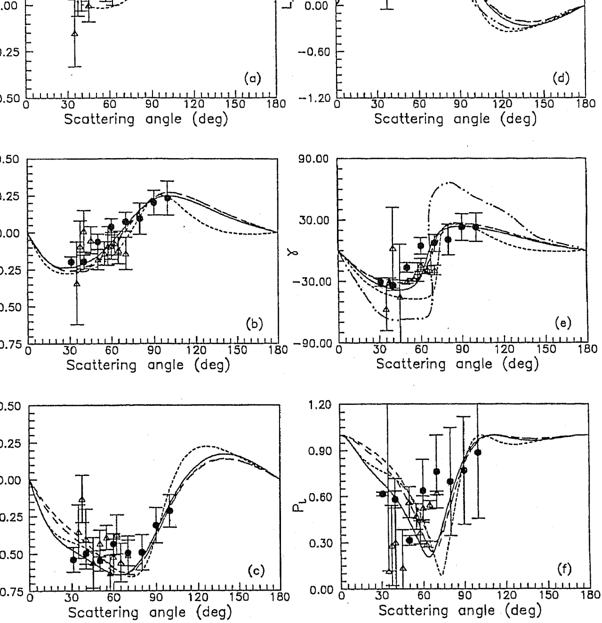

Figure 18. Same as figure 3.18 but for $E_i = 60$ eV. Notation same as in figure 17 and -••-••- FOMBT results of Csanak and Cartwright [29]; • experimental data of Beijers *et al* [26]; △ experimental data of Silim *et al* [25].

on energy of 39.7 eV. Our various DWA results qualitatively agree with the available imental data for P_1 and P_3 parameters although for P_2 the measurements of phrey *et al* [27] at 90° are not in so good agreement with our results. Further for $L_\perp$, d P_l parameters our results are compared with the reported experimental data of phrey *et al* [27] and the FOMBT [29] results for $L_\perp$ and γ. The agreement for $L_\perp$ een the different theories and the experimental data is good whereas for the ment angle γ, the experimental data above 40° lie much below all theoretical results for P_l the depth of minima in the experimental results is not so sharp and is less

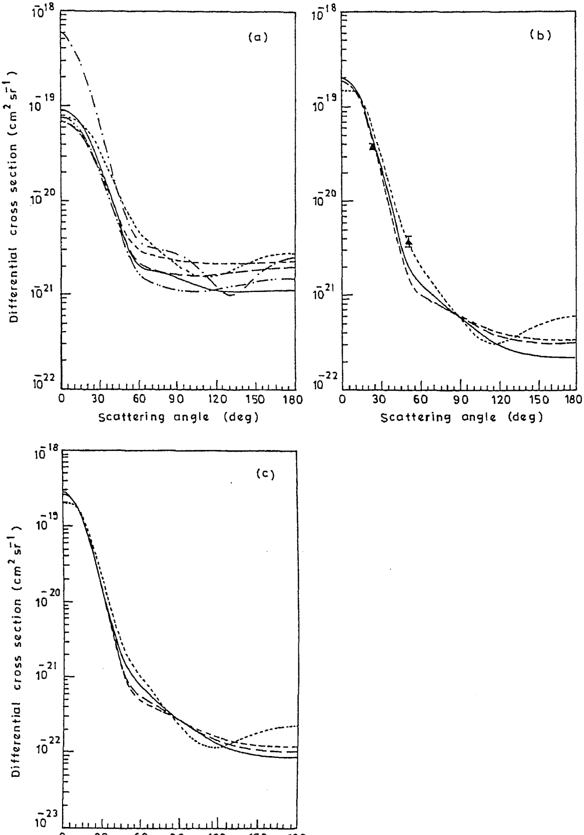
(a)
(b)
(c)
Differential cross section ($cm^2 sr^{-1}$)
10^{-18}
10^{-19}
10^{-20}
10^{-21}
10^{-22}
10^{-23}
0
30
60
90
120
150
180
Scattering angle (deg)

results. In figure 18 our results for the various Stokes parameters and the $L_\perp$, γ and P_l parameters are presented at 60 eV alongwith the data of Beijers *et al* [26] and Silim *et al* [25] as well as the FOMBT [29] results available for $L_\perp$ and γ. Our DWA results agree well with the experimental data for all these parameters alongwith the FOMBT results. Further as expected with the increase in energy the various DWA results tend to come closer.

3.3 3^1D *excitation*

In figure 19 the DCS results are presented for the 3^1D excitation in helium at electron energies of 40, 60 and 80 eV. These are compared with the only available CCC calculations of Bray *et al* [30] and the FOMBT calculations of Cartwright *et al* [11] at 40 eV. The relative DCS data of Batelaan *et al* [24] at 60 eV are also reported which we compared after normalizing them as best fit to our results of FF model. We see from the figure at 40 eV that all the theoretical results are in reasonable agreement among themselves except CCC results which are much larger at smaller angles. At 60 eV our DWA results are in agreement with the experiments of Batelaan *et al* [24] while rest of

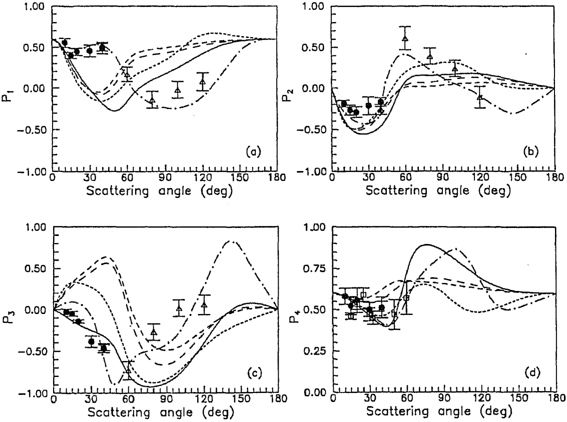

Figure 20. Stokes parameters P_1, P_2, P_3 and P_4 for the electron impact 1^1S–3^1D excitation in helium at $E_i = 40$ eV. ———— present FF results; - - - - - - - present IF results; – – – – – present II results; — — — present IIP results; -●-●- CCC results of

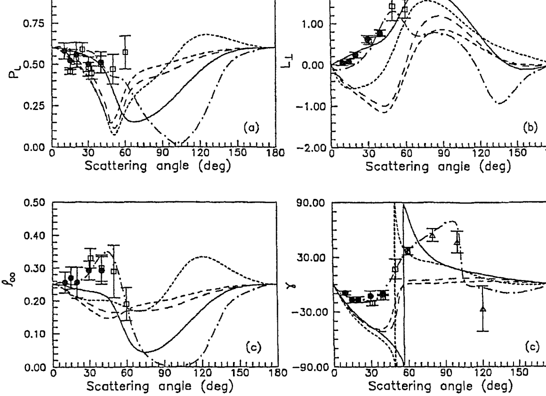

Figure 21. The alignment and orientation parameters P_l, γ, $L_\perp$ and ρ_{00} for electron impact 1^1S–3^1D excitation in helium at $E_i = 40\,\text{eV}$. Notation is same as figure 20.

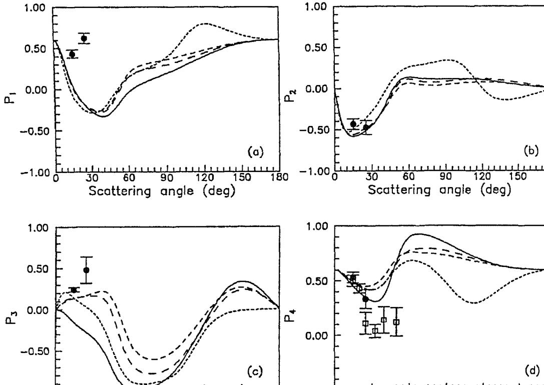

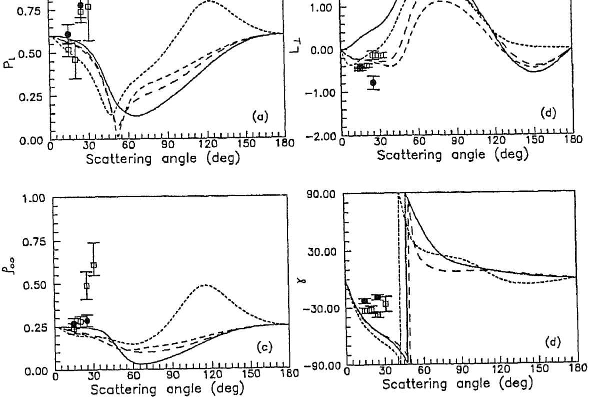

Figure 23. Same as figure 21 but for $E_i = 60\,\text{eV}$.

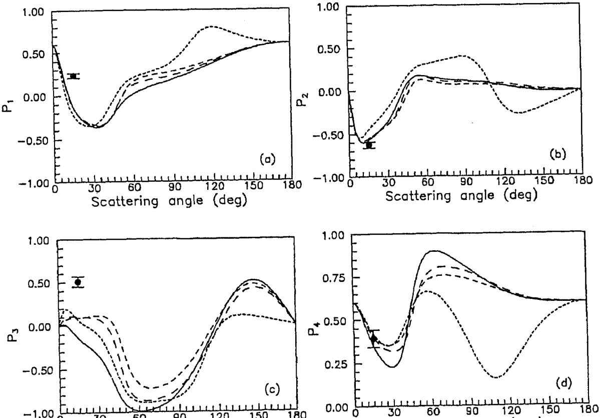

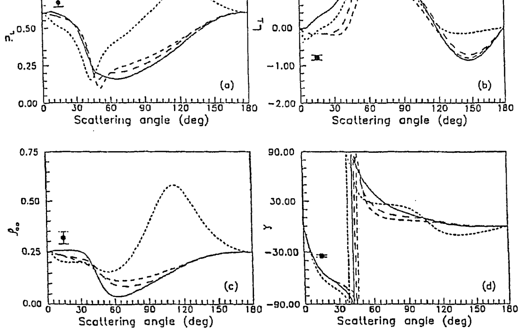

Figure 25. Same as figure 21 but for $E_i = 80\,\text{eV}$.

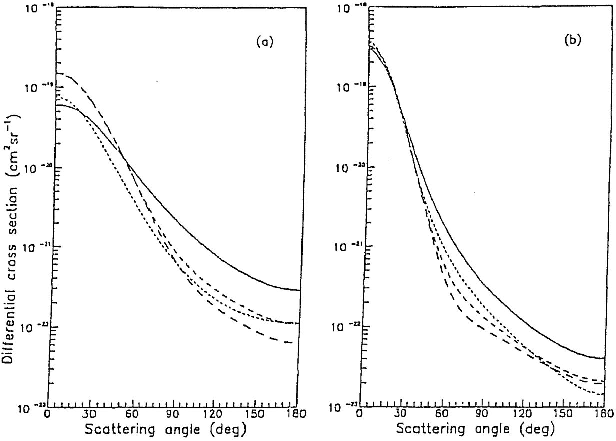

Figure 26. Differential cross section in units of cm^2 sr^{-1} for the positron impact 1^1S–3^1D excitation in helium at E_i = **(a)** 40 eV and **(b)** 80 eV. ———— present FF

and P_4) and coherence parameters (γ, P_l, $L_\perp$ and ρ_{00}) for the 1^1S-3^1D excitation in helium. These are compared with the experimental data of Donnelly *et al* [36], Mikosza *et al* [37] and Batelaan *et al* [35] and the CCC results of Bray *et al* [30]. Our DWA results are in reasonably good agreement with the experimental data though for the P_l and γ parameters the experiments tend to lie qualitatively higher than our results. Further, as expected from other previous calculations using the distorted wave approximation our FF model results are found to give best agreement with the experimental data. Similar to the results presented in figures 20 and 21, we give in figures 22 and 23 our corresponding various DWA results at 60 eV electron energy which are compared with the only available experiments of Batelaan *et al* [35] and Mikosza *et al* [37]. The features observed are as at 40 eV. Finally, in figures 24 and 25, similar results at 80 eV are given and compared with the single available experimental data of Mikosza *et al* [37]. As expected with the increase in energy the different DWA results come closer and are in good agreement with experiment. As can be seen from all the figures 19–25 and comparing our calculations in different models we find that the results are quite sensitive to the choice of the distortion potentials in the initial and final channels. In addition, on comparing the results in the IIP and II models (i.e. with and without the polarization potential) it is noted that the inclusion of the polarization effect in the distortion potential improves the agreement with the experimental data slightly.

In figure 26, the DCS results are presented for positron-impact 3^1D excitation at 40 and 80 eV incident positron energy. Here the FF results are higher than the II and IF results whereas as seen for the electron-impact excitation the results in FF model were lowest with respect to the other models.

3.4 3^3D *excitation*

In figure 27 the DCS results for 3^3D excitation at 40, 60 and 80 eV are shown. Our DWA calculations in all the models are given. At 40 eV they are compared with the available CCC [31] and FOMBT [11] results. The relative DCS normalized as best fit to our FF model results of Batelaan [24] are also presented at this energy. We find the CCC results lie lower than the DWA results in the smaller angular region and fall rapidly in large angular region. The FOMBT results are similar to the DWA results in small scattering angles. At 60 and 80 eV electron energies since no other results are available for comparison only our DWA results are presented which behave like the results at 40 eV. In figures 28 and 29, respectively the results for electron-impact excitation of the 3^3D state are presented for the Stokes parameters (P_1, P_2, P_3 and P_4) and the parameters (γ, P_l, $L_\perp$ and ρ_{00}) in all the different models of DWA. These are compared with the experimental results of Batelaan *et al* [35] and Crowe *et al* [31] and the CCC results as given in Crowe *et al* [31]. For this transition the CCC results are found to have better overall agreement with the experimental data than our DWA results. In figures 30 and 31 similar results for these parameters at 60 eV are shown. Due to non-availability of any other measurement or calculation we have presented only our DWA results. The observed features are similar to those for 40 eV.

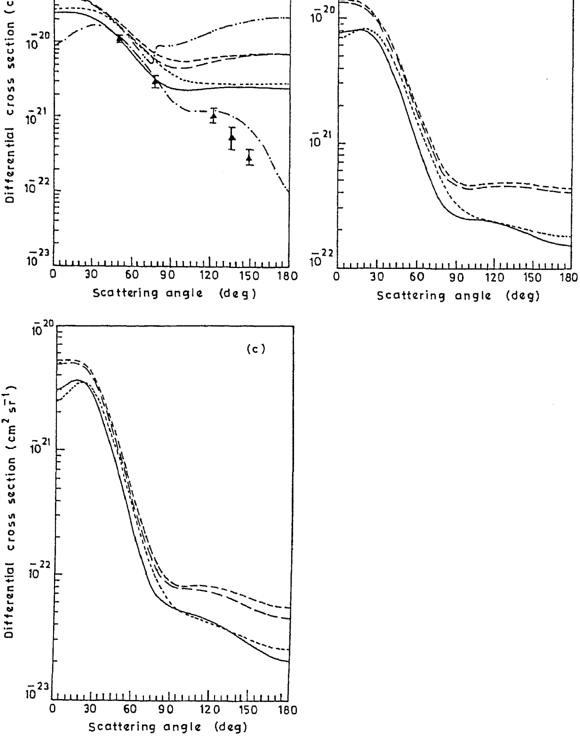

Figure 27. Differential cross section in units of cm^2 sr^{-1} for the electron impact 1^1S–3^3D excitation in helium at E_i = (**a**) 40 eV, (**b**) 60 eV and (**c**) 80 eV. ——— present FF results; - - - - - - - present IF results; – – – – – present II results; — — — present IIP results. -●-●- CCC results of Bray *et al* [31]; -●●-●●- FOMBT results of Cartwright *et al* [77]; ▲ relative experimental data of Batelaan *et al* [24].

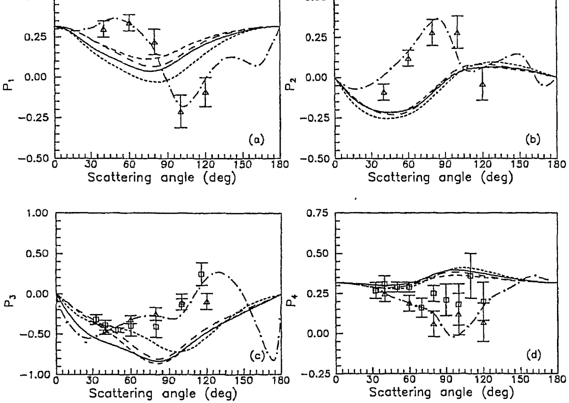

Figure 28. Stokes parameters P_1, P_2, P_3 and P_4 for the electron impact 1^1S–3^3D excitation in helium at $E_i = 40$ eV. ———— present FF results; - - - - - - - present IF results; – – – – – present II results; — — — present IIP results; -●-●- CCC results of Bray *et al* [31]; □ experimental data of Batelaan *et al* [35]; △ experimental data of Crowe *et al* [31].

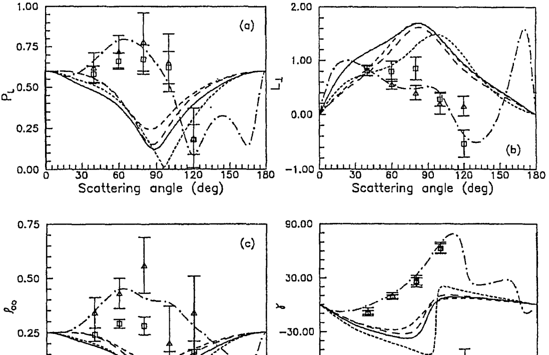

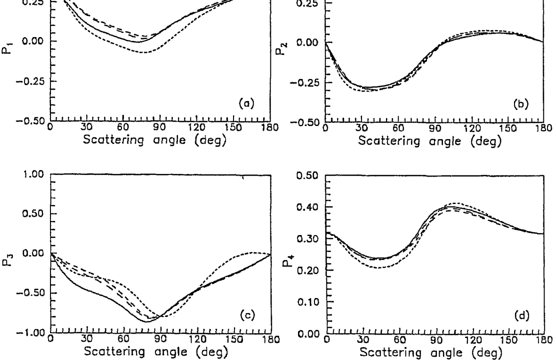

Figure 30. Stokes parameters P_1, P_2, P_3 and P_4 for the electron impact 1^1S–3^3D excitation in helium at $E_i = 60$ eV. ———— present FF results; - - - - - - - present IF results; – – – – – – present II results; — — — present IIP results.

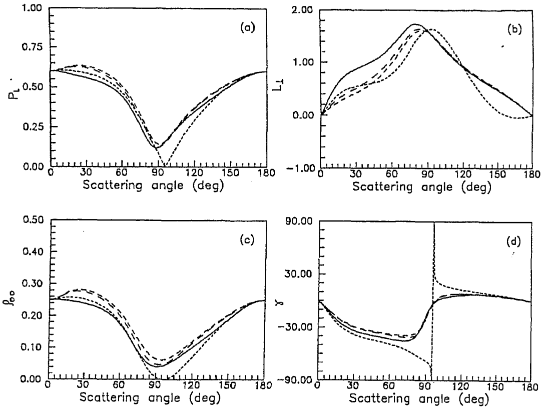

4. Conclusion

An extensive theoretical study in the distorted-wave approximation has been carried out for the electron impact $3^{1,3}P$, $3^{1,3}D$ excitations from the ground 1^1S state in helium. Results are reported for the Stokes parameters and alignment and orientation parameters and DCS in the energy range of 40–100 eV. These are compared with recent theoretical and experimental results. The DWA results are found sensitive to the choice of the distortion potential used in the calculations of the distorted waves. As well known through the comparison of first Born results and distorted wave results that the effect of distortion potential which is dominated by static and exchange potentials is reflected in the results for the differential cross sections and different parameters more at the intermediate and backward scattering angles except that the part of polarization potential effects the forward scattering only which is not very dominant. Further the results for Stokes parameters and alignment and orientation parameters are more sensitive in comparison to the DCS results to the model employed for the calculation and hence these provide a better test for the usefulness of the various models. The calculation has also been extended to positron-impact $1^1S - 3^1P$, 3^1D excitations. In contrast to the electron impact case, we see the striking feature that P_1, P_2, P_3 and $L_\perp$ retain the same sign throughout the entire angular range for positron-impact scattering.

Acknowledgements

Financial assistance from the Council of Scientific and Industrial Research (CSIR), New Delhi and University Grants Commission (UGC), New Delhi is gratefully acknowledged. One of the authors (SV) is also thankful to CSIR, New Delhi for the Senior Research Fellowship.

References

- [1] M A Khakoo, D Roundy and F Rugamas, *Phys. Rev.* **A54**, 4004 (1996)
- [2] S Verma and R Srivastava, *Phys. Rev.* **A50**, 2269 (1994)
- [3] S Verma and R Srivastava, *J. Phys.* **B30**, 1293 (1997)
- [4] S Verma, R Srivastava and Y Itikawa, *J. Phys.* **B28**, 1023 (1995)
- [5] S Verma and R Srivastava, *J. Phys.* **B29**, 3215 (1996)
- [6] K Bartschat and D H Madison, *J. Phys.* **B21**, 153 (1988)
- [7] J P M Beijers, D H Madison, J van Eck and H G M Heideman, *J. Phys.* **B20**, 167 (1987)
- [8] D H Madison *J. Phys.* **B12**, 3399 (1979)
- [9] A K Katiyar and R Srivastava, *Phys. Rev.* **A38**, 2767 (1988)
- [10] A Chutijian and L D Thomas, *Phys. Rev.* **A11**, 1583 (1975)
- [11] D C Cartwright, G Csanak, S Trajmar and D F Register, *Phys. Rev.* **A45**, 1602 (1992)
- [12] M Allan, *J. Phys.* **B25**, 1559 (1992)

(1975)

[18] R McAdams and J F Williams, *J. Phys.* **B15**, L247 (1982)

[19] G Csanak and D C Cartwright, *Phys. Rev.* **A38**, 2740 (1988)

[20] P A Neill and A Crowe, *J. Phys.* **B21**, 1879 (1988)

[21] P A Neill, B P Donnelly and A Crowe, *J. Phys* **B22**, 1417 (1989)

[22] W C Fon, K P Lim and P M J Sawey, *J. Phys.* **B26**, L747 (1993)

[23] S Trajmar, D F Register, D C Cartwright and G Csanak, *J. Phys.* **B25**, 4889 (1992)

[24] H Batelaan, F Vercoulen, J van Eck and H G M Heideman, *J. Phys.* **B25**, 4911 (1992)

[25] H A Silim, H J Beyer, A El-Sheikh and H Kleinpoppen, *Phys. Rev.* **A35**, 4454 (1987)

[26] J P M Beijers, S J Doornenbal, J van Eck and H G M Heideman, *J. Phys.* **B20**, 5529 (198

[27] I Humphrey, J F Williams and E L Heck, *J. Phys.* **B20**, 367 (1987)

[28] B P Donnelly, P A Neill and A Crowe, *J. Phys.* **B21**, L321 (1988)

[29] D C Cartwright and G Csanak, *J. Phys.* **B19**, L485 (1986)

[30] I Bray, D V Fursa and I E McCarthy, *Phys. Rev.* **A51**, 500 (1995)

[31] A Crowe, B P Donnelly, D T McLaughlin, I Bray and D V Fursa, *J. Phys.* **B27**, L795 (19

[32] E J Mansky and M R Flannery, *J. Phys.* **B20**, L235 (1987)

[33] E J Mansky and M R Flannery, *J. Phys.* **B24**, L551 (1991)

[34] H B van Linden van den Heuvell, G Nienhuis, J van Eck and H G M Heideman, *J. Phys.* **B** 2667 (1981)

[35] H Batelaan, J van Eck and H G M Heideman, *J. Phys.* **B24**, L397 (1991)

[36] B P Donnelly and A Crowe, *J. Phys.* **B21**, L637 (1988)

[37] A G Mikosza, R Hippler, J B Wang and J F Williams, *Z. Phys.* **D30**, 129 (1994)

[38] N Andersen, J W Gallagher and I V Hertel, *Phys. Rep.* **165**, 1 (1988)

[39] J A Slevin and S Chwirot, *J. Phys.* **B23**, 165 (1990)

[40] D C Cartwright and G Csanak, *J. Phys.* **B20**, L583 (1987)

[41] G Csanak and D C Cartwright, *J. Phys.* **B20**, L603 (1987)

[42] L I Schiff, *Quantum Mechanics* (McGraw-Hill, New York, 1968)

[43] T G Winter and C C Lin, *Phys. Rev.* **A12**, 434 (1975)

[44] J B Furness and I E McCarthy, *J. Phys.* **B6**, 2280 (1973)

[45] S Vučić, R M Potvliege and C J Joachain, *J. Phys.* **B20**, 3157 (1987)

[46] B L Jhanwar and S P Khare, *J. Phys.* **B9**, L527 (1976)

[47] T M Miller and B Bederson, *Adv. At. Mol. Phys.* **13**, 1 (1977)

[48] M H Mittleman and K M Watson, *Ann. Phys. (NY)* **10**, 268 (1960)

[49] K Blum, *Density Matrix Theory and Applications* (Plenum Press, New York, 1981)

Dissociation energy of diatomic molecules

SARVPREET KAUR and C G MAHAJAN
Centre of Advanced Study in Physics, Panjab University, Chandigarh 160014, India
E-mail: spectphys@ch1.vsnl.net.in

MS received 3 March 1998

Abstract. The dissociation energy of twelve diatomic molecules has been determined by fitting four-parameter potential function $U(r) = D_e[[1 - \exp\{-b(r - r_e)\}]/[1 - C\exp\{-b(r - r_e)\}]]^2$ to the true Rydberg–Klein–Rees (RKR) curves for their fifteen electronic states using the mean square deviation as the criterion for the selection of the best fit. Average deviation of D_e has been found to be 2.7% as compared to 20.5% obtained with Lippincott's potential function for these molecules. In addition the anharmonocity constant $\omega_e x_e$ has also been calculated for the same electronic states yielding average mean deviation 8.9%.

Keywords. Dissociation energy; four-parameter potential; anharmonicity constant.

PACS No. 33.15

1. Introduction

The spectroscopic data for most of the diatomic molecules is available for vibrational levels which are considerably below the dissociation limit. So different extrapolation methods have been employed to find the dissociation energy of these molecules and Birge–Sponer [1] approach is most commonly used for this purpose. Obviously, the results inherently suffer from an uncertainty determined by the extrapolation gap and the method of extrapolation. In addition, it has long been known [2] that vibrational energies near the dissociation limit and hence the vibrational spacings depend on the functional form of the long range potential. This, in turn, leads to a marked deviation of graphical extrapolation from the accurate estimate of the dissociation limit. Using asymptotic approximation for long range potentials of the form

$$V(r) = D_e - \sum_n \frac{C_n}{r^n}, \tag{1}$$

where D_e is the dissociation limit of the potential and C_n is given by

$$E(v) = D_e - \frac{C_n}{(r_{\max}(v))^2}. \tag{2}$$

LeRoy and co-workers [2–4] have developed WKB based extrapolation technique to

state	(A)	(cm^{-1})	(cm^{-1})	$10^3(\mathrm{cm}^{-1})$	(cm^{-1})	(cm^{-1})	(a.m.u.)	Ref.
$\mathrm{Li_2X^1\Sigma_g^+}$	2.6729	8516.780	351.430	7.040	0.6726	2.6100	3.5080	[19]
$\mathrm{Na_2X^1\Sigma_g^+}$	3.0788	6022.600	159.177	0.873	0.1547	0.7254	11.4949	[20]
$\mathrm{K_2X^1\Sigma_g^+}$	3.9244	4440.000	92.405	0.212	0.0562	0.3276	19.4800	[11]
$\mathrm{Cl_2X^1\Sigma_g^+}$	1.9872	20276.440	559.751	1.516	0.2442	2.6943	17.4844	[21]
$\mathrm{Cl_2B^3\Pi}$	2.4311	3341.170	255.3800	2.511	0.1631	4.8000	17.48442	[22]
$\mathrm{I_2XO_g^+}$	2.6664	12547.335	214.520	0.113	0.0373_7	0.6079	63.4522	[23]
$\mathrm{IClX^1\Sigma^+}$	2.3209	17557.600	384.275	0.532	0.1142	1.4920	27.4147	[16]
$\mathrm{IClA^3\Pi_1}$	2.6850	3814.700	211.030	0.744	0.0852_9	2.1200	27.4147	[16, 17]
$\mathrm{IClA^3\Pi_2}$	2.6651	4875.520	224.571	0.674	0.0865	1.8823	27.4147	[17]
$\mathrm{HFX^1\Sigma^+}$	0.9168	49384.000	4138.320	772.400	20.9557	89.8800	0.9571	[24]
$\mathrm{H_2X^1\Sigma_g^+}$	0.7416	38297.000	4401.265	3051.300	60.8477	120.6020	0.5039	[25]
$\mathrm{COX^1\Sigma^+}$	1.1283	90529.000	2169.813	17.504	1.93137	13.2883	6.8562	[13, 14]
$\mathrm{XeOd^1\Sigma^+}$	2.8523	693.000	156.832	5.400	0.1456	9.8678	14.2327	[26]
$\mathrm{Cs_2X^1\Sigma_g^+}$	4.6480	3649.500	42.020	0.022	0.0117	0.0826	66.4527	[27]
$\mathrm{Rb_2X^1\Sigma_g^+}$	4.2099	3950.000	57.7807	0.055	0.0224	0.1391	42.4559	[12]

be pointed out that a proper RKR analysis yields a much more accurate estimate of D_e [5].

In 1990, Wei Hua introduced a four-parameter (FP) potential function [6],

$$U(r) = D_e\left[\frac{1-\exp\{-b(r-r_e)\}}{1-C\exp\{-b(r-r_e)\}}\right]^2, \tag{3}$$

where $b = (1 - C)a$, and C is an adjustable parameter having $|C| < 1$ with $a = \sqrt{k_e/2D_e}$.

The FP potential fits very closely to the RKR curves compared to Morse and other analytical functions [6], when the potential domain extends to near dissociation limit. It is, therefore, natural to expect that FP potential would predict the dissociation limit precisely. We have made an attempt to investigate this aspect of the FP potential and the results constitute the content of this communication. Wei Hua considered fifteen electronic states of twelve molecules to examine his FP potential and the same electronic states have been used in the present studies as the spectroscopic constants, the RKR potential curves and the dissociation energies are known very accurately for these states. The molecular constants and respective dissociation energies are given in table 1.

2. Estimation of the dissociation energy

Because of the anharmonocity the molecules in the highly excited vibrational levels spend most of their time in the neighborhood of outer turning points. Therefore, the vibrational by using iteration method such that mean square deviation, given by

$$\Delta Y_j = \frac{\sqrt{\overline{(U_j - U_{\mathrm{RKR}})^2}}}{D_e}, \tag{4}$$

where j stands for various potential functions, has minimum value. With the rough estimated values of D_e from the linear extrapolation method, i.e., $D_e = \omega_e^2/4\omega_e x_e$ and C from the relation [9]

$$C_{\mathrm{rel}} = \left(-\frac{1}{12} + x\right) - \sqrt{\frac{120}{144} - \frac{37}{48}x^2 - \frac{2}{12}x + \frac{17}{144}\frac{G}{ar_e^2}}, \tag{5}$$

where

$$x = \frac{1+F}{ar_e}, \quad F = \frac{\alpha_e \omega_e}{6B_e^2}, \quad \text{and} \quad G = \frac{8\omega_e x_e}{B_e}$$

for the whole potential curve as the starting points, the potential energies corresponding to FP potential have been obtained by changing D_e and C in steps of $\pm 100\,\mathrm{cm}^{-1}$ and ± 0.1, respectively. The resulting values are correlated with the experimental results and the values of D_e and C corresponding to minimum value of Y_j are chosen for the second scan. In the second and subsequent scans, the values of D_e and C are varied in steps of decreasing magnitudes. The process is continued till Y_j is minimum. The last scan has been carried out by changing D_e by $\pm 1\,\mathrm{cm}^{-1}$ and C by ± 0.001. The value of D_e that corresponds to minimum deviation Y_j in the final scan is regarded as the best estimate of D_e and relevant C value.

3. Results and discussion

Dissociation energies of fifteen electronic states of molecules Li_2, Na_2, K_2, Rb_2, Cs_2, Cl_2, I_2, ICl, HF, H_2, CO, XeO have been obtained employing the molecular constants listed in table 1 and the results are presented in table 2. For comparison, values of D_e obtained from Lippincott's analytical potential function [10]

$$U(r) = D_e(1 - \mathrm{e}^{-x})\{1 - abx^{1/2}\exp[-bx^{1/2}]\}, \tag{6}$$

where

$$F = \frac{\alpha_e \omega_e}{6B_e^2}, \quad a = \frac{F}{1 + (5F/4)}, \quad N = \frac{2}{r_e}\left(\frac{F}{ab}\right)^2 \quad \text{and}$$

$$x = \frac{N(r - r_e)^2}{2r}, \quad b = 1.065;$$

which is considered to be best among the three parameter potential functions for the

Table 2. Comparison of experimental values of D_e with calculated values and the mean deviations $\Delta X = (D_e(\text{exptl}) - D_e(i))/(D_e($ where $D_e(i)$ stands for, $D_e(\text{FP})$, FP; $D_e(\text{Lipp})$, Lippincot; for fifteen electronic states.

	$D_e(\text{exptl})$ (cm^{-1})	$C_{\min}$	$D_e(\text{FP})$ (cm^{-1})	$D_e(\text{Lipp})$ (cm^{-1})	ΔX_{FP} (%)	ΔX_{Lipp} (%)	$C_{\min}(1/3)$	$D_e(\text{FP}_{1/3})$ (cm^{-1})	$\Delta X_{\text{FP}}(1/3)$ (%)	E
Σ_g^+	8516.78	−0.350	8613	10111	1.1	18.7	−0.472	8514	0.03	0.
${}^1\Sigma_g^+$	6022.00	−0.482	6015	7032	0.1	16.7	−0.489	6013	0.15	0.
${}^1\Sigma_g^+$	4440.00	−0.359	4646	8130	4.6	83.1	−0.391	4580	3.15	0.
Σ_g	20276.40	−0.349	20574	23213	1.5	14.5	−0.509	20283	0.03	0.
Π	3341.17	+0.018	3282	3300	1.8	1.3	+0.228	3327	0.42	0.
$^+$	12547.00	−0.368	12497	14102	0.4	12.4	−0.346	12492	0.44	0.
${}^1\Sigma^+$	17557.00	−0.316	17831	20067	1.6	14.2	−0.458	17548	0.05	0.
${}^3\Pi_1$	3814.00	−0.248	3719	4125	2.5	8.3	−0.030	3766	1.25	0.
${}^3\Pi_2$	4875.00	−0.288	4746	5338	2.6	9.5	−0.191	4780	1.95	0.
$X^1\Sigma^+$	49384.00	+0.000	51387	48468	4.0	1.9	−0.110	50261	1.77	0.
Σ_g^+	38297.00	−0.009	39983	38109	4.4	0.5	−0.134	38860	1.47	0.
${}^1\Sigma^+$	90529.00	+0.069	95712	78612	5.7	13.2	+0.077	96250	6.31	0.
$d^1\Sigma^+$	693.00	+0.196	660	619	4.8	10.7	+0.368	687	0.86	0.
${}^1\Sigma_g^+$	3649.50	−0.450	3658	5055	0.24	38.5	−0.450	3635	0.40	0.
$X^1\Sigma_g^+$	3950.00	−0.370	4172	6447	5.6	63.2	−0.390	4131	4.58	0.
ge					2.7	20.5			1.5	

ues are derived from: *NDE long range technique; **RKR potential curve; $^+$Extrapolation from the RKR curve; $^{++}$Limiting curve of disso electronic states given in table 1.

$\omega_e x_e$(exptl.) cm^{-1}	$\omega_e x_e$(FPC$_{\mathrm{rel}}$) cm^{-1}	$\omega_e x_e$(FPC$_{\mathrm{min}}$) cm^{-1}	$\Delta X_{\mathrm{FPC_{rel}}}$ (%)	$\Delta X_{\mathrm{FPC_{min}}}$ (%)
2.6100	3.2150	2.7680	23.1	6.1
0.7254	0.8816	0.7895	21.5	6.4
0.3276	0.3859	0.3536	17.8	7.9
2.6943	3.5437	2.9418	31.5	9.2
4.8000	4.4261	5.0540	7.8	5.2
0.6079	0.7973	0.7063	31.2	16.2
1.4920	1.9104	1.6220	28.0	8.7
2.1210	2.4911	2.4340	17.4	14.7
1.8823	2.2354	2.1110	18.8	12.2
89.8800	98.4446	83.3050	9.5	7.3
120.6020	152.4790	120.2257	26.4	0.3
13.2883	13.6250	13.2027	2.5	0.6
9.8678	8.3081	11.5570	15.8	17.1
0.0826	0.0950	0.0911	15.1	10.3
0.1391	0.1678	0.1540	20.6	10.8
Average			17.4	8.9

have been computed for these electronic states using the relation

$$\omega_e x_e = \frac{h}{8\pi^2 c\mu} a^2(1 + C + C^2) = B_e\Delta(1 + C + C^2) \tag{7}$$

obtained in our earlier work [9]. Here, we have used C calculated above for the outer limb. These results together with the experimental values of $\omega_e x_e$ and the ones found by us in ref. [9], are compiled in table 3.

Earlier works on the studies of electronic states of the molecules subjected to the present analysis (see the references in table 1) show that the properly executed NDE method of LeRoy *et al* [2–4] and RKR approach yield accurate values of D_e. So we have taken these D_e values as experimental (being the best prediction) to compare our findings and have given these in the second column of the table 2. It may be mentioned that D_e for HF included in this table has been obtained earlier from the limiting curve of dissociation.

A comparison of our results constituting third column of table 2 with experimental values listed in column 2 shows that the extent of agreement depends on the method. For the electronic states $\mathrm{Li_2(X^1\Sigma_g^+)}$, $\mathrm{Na_2(X^1\Sigma_g^+)}$, $\mathrm{Cl_2(X^1\Sigma_g^+)}$, $\mathrm{I_2(X^1\Sigma_g^+)}$, $\mathrm{ICl(X^1\Sigma_g^+)}$ and $\mathrm{Cs_2(X^1\Sigma_g^+)}$ for which experimental D_e values have been found with NDE technique (that includes the long range forces) the difference is less than 2%. However, in A and A' electronic states of ICl the deviations are respectively 2.5% and 2.6%. The deviation in the case of the electronic state A can be viewed in the light of reported vibrational perturbations near dissociation and the merging approach (merging the constants from individual absorption band and emission band through least square fit) used to obtain D_e [16]. Similar explanation is valid for state A' also since there is a possibility of perturliterature, it is found that the highest observed vibrational levels in K_2, CO and Rb_2 viz. $v = 37$ at 63334.333 cm^{-1} for CO [13,14], $v = 50$ at 3687.749 cm^{-1} for K_2 [11], $v = 72$ at 3313.143 cm^{-1} for Rb_2 [12], giving $E_{\text{max}}/D_e \sim 0.70$, 0.83, and 0.84 respectively, where E_{max} denotes the energy of highest observed level, are fairly below the respective dissociation limits. That means, RKR potential curve has been drawn accurately only up to the observed levels. Moreover, since RKR does not provide any direct means of extrapolation beyond the observed levels [2], indirect methods have been employed to obtain D_e values which are likely to be at the variance from the accurate values. In the case of XeO and H_2 the levels are observed only up to $v = 8$ and $v = 14$, respectively, so that D_e are expected to be more erroneous.

Long range forces have dominant influence [2] on the vibrational levels close to dissociation limit ($\sim$ top 10% of the potential well). With a view to examine the performance of the FP potential function close to the dissociation limit, D_e (denoted as D_e $(\text{FP}_{1/3})$ in table 2) and C (referred to as $C_{\text{min}}(1/3)$ in table 2) have been derived considering only the highest one-third of the known vibrational levels. But for the CO electronic state, the results (given in column 10 of table 2) for all other states have been improved significantly. The slight adverse result of CO is understandable since the known data constitute only 70% of the potential well starting from equilibrium position. This observation, besides providing better accuracy of D_e, also strengthens the earlier findings [6], that FP potential describes experimental potential curves more accurately especially when the potential domain extends to near the dissociation limit.

Values of vibrational constant $\omega_e x_e$, when computed from the outer limb of the RKR curve show a marked improvement over the ones calculated using inner wall as well as the outer wall (i.e. $r_{\text{min}} < r < r_{\text{max}}$) of the potential curve (table 3). The average mean deviation from the experimental values has been reduced to 8.9% from 17% [9]. Furthermore, since $\omega_e x_e$ has been calculated using outer limb of the potential curve, the findings are in conformity with the fact that, because of anharmonocity, the vibrational spacings and other properties of diatomic molecules [2, 7, 8] are explained mainly by the outer limb of the potential curve.

4. Conclusion

FP potential function of Wei Hua can be used to predict dissociation energy of the electronic states of diatomic molecules. The accuracy of prediction is close to the one obtained by NDE long range expansion technique or by RKR potential curve constructed up to near dissociation limit. Besides, FP potential function, through equation (7), predicts $\omega_e x_e$ value better than the known three parameter analytical functions.

Acknowledgment

[1] R T Birge and H Sponer, *Phys. Rev.* **28**, 259 (1926)
R T Birge, *Trans. Faraday Soc.* **25**, 707 (1928)
A G Gaydon, *Dissociation Energies* 3rd edition (Chapman and Hall Ltd., London, 1968)

[2] R J Le Roy and R B Bernstein, *J. Chem. Phys.* **52**, 3869 (1970); *Chem. Phys. Lett.* **5**, 42 (1970)

[3] R J Le Roy and W Lam, *Chem. Phys. Lett.* **71**, 544 (1980)

[4] J W Tromp and R J Le Roy, *Can. J. Phys.* **60**, 26 (1982)

[5] E A Mason and L Monchick, *Adv. Chem. Phys.* **12**, 329 (1967)

[6] H Wei, *J. Phys.* **B23**, 2521 (1990)
H Wei, *Phys. Rev.* **A42**, 2524 (1990)

[7] R J LeRoy, *Can. J. Phys.* **50**, 953 (1972)

[8] W C Stwalley, *J. Chem. Phys.* **58**, 3867 (1973); in *Energy, structure and reactivity* edited by D W Smith and W B Mac Rae (Wiley, New York, 1973) p. 259

[9] S Kaur and C G Mahajan, *J. Quantit. Spectrosc. Radiat. Transfer* (communicated)

[10] D Steele, E R Lippincott and J T Vanderslice, *Rev. Mod. Phys.* **34**, 239 (1962)
D Steele and E R Lippincott, *J. Chem. Phys.* **35**, 2065 (1961)

[11] A J Ross, P Crozet, J D'Incan and C Effantin, *J. Phys.* **B19**, L145 (1986)

[12] C Amiot, P Crozet and J Verges, *Chem. Phys. Lett.* **121**, 390 (1985)

[13] S M Kirscnner and J K G Watson, *J. Mol. Spectrosc.* **51**, 321 (1974)

[14] B R Won and K N Rao, *J. Mol. Spectrosc.* **49**, 317 (1974)

[15] G Herzberg, *Molecular Spectra and Molecular Structure* (Von Nostrand Reinhold Co., 2nd edition, 1950) vol. 1

[16] J A Coxon and M A Wickramaaratchi, *J. Mol. Spectrosc.* **79**, 380 (1980)

[17] J C D Brand, D Bussieres and A R Hoy, *J. Mol. Spectrosc.* **113**, 388 (1985)

[18] R S Mullikien, *J. Chem. Phys.* **55**, 288 (1971)

[19] B Barakat, R Bacis, F Carrot, S Churassy, P Crozet, F Martin and J Verges, *J. Chem. Phys.* **102**, 215 (1986)

[20] K K Verma, J T Bhans, A R Rajaei-Rizi and W C Stwalley, *J. Chem. Phys.* **78**, 3599 (1983)

[21] A E Douglas and A R Hoy, *Can. J. Phys.* **53**, 1965 (1985)

[22] J A Coxon, *J. Mol. Spectrosc.* **82**, 264 (1980)

[23] F Martin, R Bacis, S Churassy and J Verges, *J. Mol. Spectrosc.* **113**, 388 (1986)
R Bacis, D Cerny and F Martin, *J. Mol. Spectrosc.* **118**, 434 (1986)

[24] G Di Lonardo and A E Douglas, *Can. J. Phys.* **51**, 434 (1973)

[25] R J Spindler, *J. Quant. Spectrosc. Radiat. Transfer* **9**, 597 (1969)

[26] J D Simmons, A G Maki and J T Hougen, *J. Mol. Spectrosc.* **74**, 70 (1979)

[27] W Weickenmeier, U Diemer, M Wahl, M Raab, W Demtroder and W Muler, *J. Chem. Phys.* **82**, 5354 (1985)

Stark splitting and energy transfer between Dy^{3+}–Ho^{3+} and between Tb^{3+}–Er^{3+} in calcium–lithium borate glass

BRAJESH SHARMA, V B SINGH, D K RAI and S B RAI
Department of Physics, Banaras Hindu University, Varanasi 221 005, India
Email: sbrai@banaras.ernet.in

MS received 15 April 1997; revised 15 January 1998

Abstract. Fluorescence spectrum of Dy^{3+}, Dy^{3+}–Ho^{3+}, Tb^{3+} and Tb^{3+}–Er^{3+} doped in calibo glass have been studied using Ar^+ and excimer lasers. Non-radiative energy transfer from trivalent dysprosium and terbium (donors) to holmium and erbium (acceptors) respectively has been observed on the basis of decrease in the life time of the levels and reduction in fluorescence intensity of Dy^{3+} and Tb^{3+} on increasing Ho and Er concentrations. The interaction mechanism of donor and acceptor ions is found to be dipole–dipole in both cases. Various parameters such as donor-acceptor distances, non-radiative energy transfer efficiency (η) and energy transfer probability (P_{da}) have been computed. Stark splitting have also been marked in several intense transition of the two.

Keywords. Fluorescence; non-radiative; dipole–dipole; transfer efficiency; Stark components.

PACS Nos 78.66; 78.60

1. Introduction

The mechanism of donor-acceptor energy transfer is important in the study of phosphors and laser materials. The energy transfer may be through radiative or non-radiative processes. The non-radiative energy transfer processes are major factors in determining the long wavelength operating limits for the solid state lasers [1].

The non-radiative energy transfer has been studied by several authors [2–8] in different glasses with different rare-earth ions as dopant. A mechanism for energy transfer from donor to acceptor was first suggested by Forster [6] and then extended by Dexter [7]. This theory was however found inadequate to explain all concentration regimes of the acceptor. Fong and Diestler [8] developed a theory which takes into account the fact that for low acceptor concentrations there is usually a one-to-one correspondence between donor and acceptor while at higher acceptor concentrations one donor ion may interact with two or more neighbouring acceptor ions.

The non-radiative energy transfer from Dy^{3+} to Pr^{3+} in calibo and phosphate glasses has been reported by Joshi and coworkers [9, 10]. Similarly energy transfer from Tb^{3+} to Er^{3+} in sodium borate glass has also been studied by Joshi and Pandey [11]. At low glass lattice has been studied by Pant *et al* [13] and from Tb^{3+} to Er^{3+} in phosphate glass by Van Uitert [14] and a dipole–dipole transfer mechanism was reported.

In this paper we report the fluorescence spectra of Dy, Dy + Ho, Tb and Tb + Er doped in calibo glass host. We have been able to resolve the Stark components in the case of the intense transitions in Dy^{3+} and Tb^{3+}. We have also measured the life time of the fluorescing levels of the two in the presence and abscence of the acceptor. A significant energy transfer from the excited Dy^{3+} (Tb^{3+}) to Ho^{3+} (Er^{3+}) was noticed from the weakening of the fluorescent lines and decrease in life time of Dy^{3+} (Tb^{3+}) level in the presence of Ho^{3+} (Er^{3+}) as acceptor. The mechanism was found to be dominated by dipole–dipole interaction. These changes have also been used to estimate the energy transfer efficiency (η) and transfer probability (P_{da}) in the two cases.

2. Experimental

The Dy^{3+} and Dy^{3+}+Ho^{3+}, Tb^{3+} and Tb^{3+}+Er^{3+} doped glasses were prepared from the spectral grade reagents with 99% stated purity by mixing 20% CaO, 10% Li_2O_3 and 70% B_2O_3. Keeping the Dy^{3+} concentration (1 wt%) fixed the concentration of Ho^{3+} was varied from 0.5 to 3 wt.%. Similarly the concentration of Tb^{3+} was held (2 wt.%) fixed and Er^{3+} concentration was varied from 0.5 to 5 wt.%. The mixture powder was melted in platinum crucible heated up to 1000°C in an electric furnance and the melt was poured into a suitable cast. The moulded glass was grinded and polished carefully to make it amenable to spectroscopic studies.

The density and refractive index were measured and other related physical properties were calculated following the procedure outlined in our previous paper [15] and

Table 1. Various physical parameters of Dy, Dy + Ho, Tb and Tb + Er in calibo glass.

Donor (Dy^{3+}) and (Tb^{3+}) concentration (N) = 0.42×10^{20} and 1.02×10^{20} ions per cc (fixed).
Donor–donor separation = 28.76 A and 21.04 A for Dy and Tb respectively.

Acceptor				Ho^{3+}				Er^{3+}		
Conc. (wt %)	0.0	0.5	1.0	1.5	2.0	3.0	1.0	2.0	3.0	5.0
Acceptor ion conc. ($N \times 10^{22}$ ions/cc)	–	0.45	0.86	1.02	1.56	2.22	0.92	1.56	2.91	4.5
Acceptor–acceptor separation	–	28.11	22.65	21.40	18.57	16.51	22.15	18.57	15.09	13.22
Acceptor ionic-radius (A)	–	17.94	14.45	13.66	11.85	10.54	14.13	11.85	9.63	8.44
Ref. index	1.56	1.53	1.57	1.55	1.52	1.57	1.49	1.50	1.52	1.49
Density	3.12	2.95	3.00	3.11	3.10	2.86	2.91	2.87	3.23	3.51
Thickness	0.15	0.16	0.15	0.14	0.15	0.16	0.25	0.24	0.24	0.26
Dielectric const.	2.43	2.34	2.46	2.40	2.31	2.46	2.22	2.20	2.21	2.24

temperature using Ar^+ laser lines as exciting line. Ne emission lines from Fe–Ne hollow cathode lamp recorded simultaneously were used for wavelength calibration. It is interesting to note that the fluorescence intensity increases even up to 6 mol % of the Dy^{3+} and Tb^{3+} in the calibo glass host.

The life time measurements were made using excimer (XeCl) laser at 308 nm at 10 Hz repetition rate and a 5001 model EG&G box car averager with 5 ns gate width.

3. Results and discussion

The optical properties of trivalent Dy^{3+} and Tb^{3+} in glassy and other host matrices have been studied extensively [16–18]. From these studies it is well known that Dy^{3+} and Tb^{3+} give broad emissions in the visible region.

The fluorescence spectra of Dy^{3+}, $Dy^{3+} + Ho^{3+}$, Tb^{3+} and $Tb^{3+} + Er^{3+}$ in calibo glass are shown in figures 1 and 2. Though both Dy^{3+} and Tb^{3+} ions show fluorescence at all the lines emitted by the Ar^+ laser, the fluorescence yield is maximum at 488.0 nm

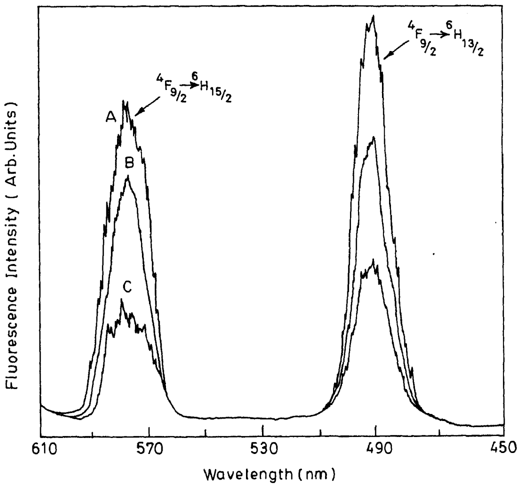

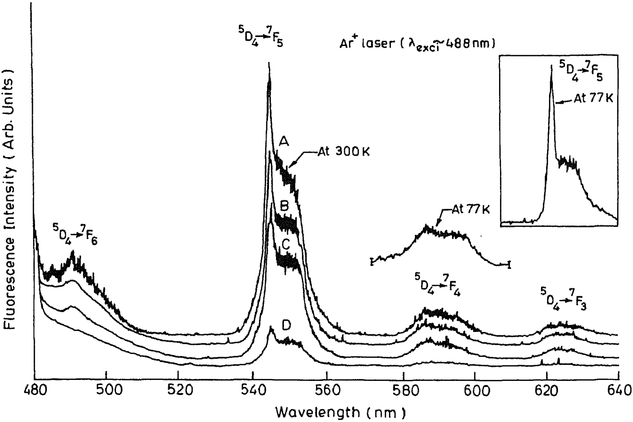

Figure 2. **(A)** Fluorescence spectrum of Tb^{3+} (2 wt %), **(B)** Tb^{3+} (2 wt %) + Er^{3+} (1 wt %), **(C)** Tb^{3+} (2 wt %) + Er^{3+} (2 wt %) and **(D)** Tb^{3+} (2 wt %) + Er^{3+} (5 wt %) doped in calibo glass at 300 K.

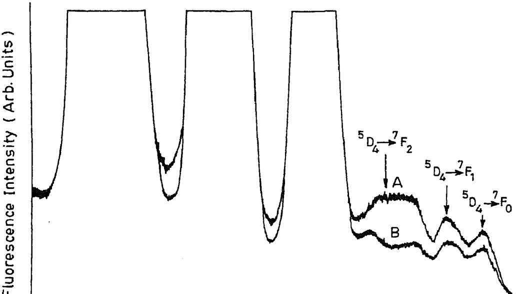

Ion	Wavelength (A)	Energy (cm^{-1})	Assignment	R.I.	FWHM (cm^{-1})	Ratio of int. of the peak at different conc. of Ho^{3+} (wt %)		
						(1)	(2)	(3)
Dy^{3+}	5720	17477	${}^4F_{9/2} \rightarrow {}^6H_{13/2}$	49	470	1	0.62	0.42
	4820	20741	${}^4F_{9/2} \rightarrow {}^6H_{15/2}$	39	710	1	0.61	0.42
						At different conc. of Er^{3+} (wt %)		
						(2)	(3)	(5)
Tb^{3+}	4911	20357	${}^5D_4 \rightarrow {}^7F_6$	12	350	0.53	0.40	0.20
	5451	18340	${}^5D_4 \rightarrow {}^7F_5$	30	290	0.52	0.39	0.19
	5881	17003	${}^5D_4 \rightarrow {}^7F_4$	6.6	600	0.52	0.39	0.18
	6242	16015	${}^5D_4 \rightarrow {}^7F_3$	5.3	500	0.53	0.40	0.20
	5609	15360	${}^5D_4 \rightarrow {}^7F_2$	1.6	470	0.52	0.39	0.19
	6670	14988	${}^5D_4 \rightarrow {}^7F_1$	1.3	140	0.53	0.39	0.20
	6788	14725	${}^5D_4 \rightarrow {}^7F_0$	1.1	70	0.52	0.39	0.20

for Tb^{3+} and at 457.9 nm for Dy^{3+}. We observed two emission lines for Dy^{3+} and four lines for Tb^{3+} at 25 mW of exciting laser power (see figures 1 and 2). However on increasing the laser power to 50 mW some additional lines are seen in the case of Tb^{3+} (see figure 3), but there is no such effect in Dy^{3+}. From the recorded fluorescence profiles at two temperatures (300 and 77 K) in the two cases we notice that at liquid nitrogen temperature the peak fluorescence intensity is increased and the bands appear sharper. Fluorescence lines and their assignments in the two cases are presented in table 2.

Incorporating Ho^{3+} and Er^{3+} ions along with Dy^{3+} and Tb^{3+} respectively (in calibo glass) decreases the intensities of the Dy^{3+} and the Tb^{3+} emission peaks by different ratios (see figures 1 and 2).

3.1 *Fluorescence spectra of Dy^{3+} and $Dy^{3+} + Ho^{3+}$*

The fluorescence spectra of Dy^{3+} and $Dy^{3+}+Ho^{3+}$ in calibo glass excited by the 457.9 nm line of the Ar^+ laser are shown in figure 1. The excited Dy^{3+} ion from ${}^4I_{15/2}$ state decays rapidly to the ${}^4F_{9/2}$ metastable state. The ${}^4F_{9/2}$ level decays by fluorescence to the ground ${}^6H_j$ multiplet (${}^4F_{9/2} \rightarrow {}^6H_{13/2}$ and ${}^4F_{9/2} \rightarrow {}^6H_{15/2}$) giving emission lines at 572 nm and 482 nm respectively. The observed line widths are large probably owing to inhomogeneous local fields in the glass. One observes the same two lines in the fluorescence from other glasses doped with Dy though the observed wavelengths in calibo glass are slightly different than for the other glasses (borate, phosphate and heavy metal fluoride glasses [19]). It appears that the transition probability from ${}^4F_{9/2}$ to other components of the ground levels are very small. A look at the fluore-

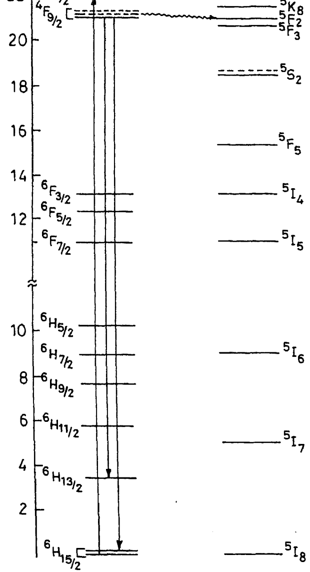

Figure 4. Energy level diagram and energy transfer scheme of Dy^{3+} and Ho^{3+} in calibo glass.

as the concentration of Ho increases. No fluorescence lines attributable to Ho are observed even up to 800 nm. This latter observation indicates that the Ho level being excited through energy transfer from Dy^{3+} decays non-radiatively. The energy separation between the $^4F_{9/2}$ level of Dy^{3+} and its ground state (21097 cm^{-1}) is almost the same as the height of the non-radiative level $^5F_2$ (21073 cm^{-1}) of Ho^{3+} over its ground state. So the energy can be transferred easily from the excited Dy^{3+} level to the Ho^{3+} level (see figure 4). There are a large number of other non-radiative levels in Ho^{3+} viz, $^3K_8$, $^5G_6$ close to the $^5F_2$ state while the Ho^{3+} states known to decay radiatively have energies 18650–15550 cm^{-1} [19–21] above the Ho^{3+} ground state. Therefore, the presence of Ho ion in the same lattice as the Dy ion depletes the population of $^4F_{9/2}$ level of Dy^{3+} in a non-radiative manner. The depletion of the upper $^4F_{9/2}$ level of Dy^{3+} is established by

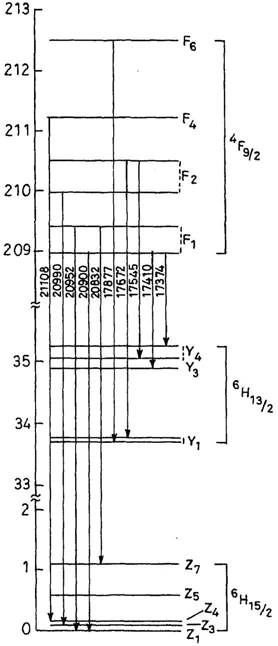

Figure 5. Stark splitting in different energy levels and observed transitions in Dy^{3+} doped in calibo glass.

fact that in our study no additional fluorescence lines due to the presence of Ho are observed is probably due to

(i) no direct excitation of the Ho ions as the exciting line is far removed in energy from suitable Ho^{3+} levels
(ii) Absorption of the emitted radiation from the Dy^{3+} ions is not possible as Ho^{3+} absorption lines are far removed in energy

20694 –	17374 $(F_1 - Y_4)$	18440 $(A_4 - X_1)$	17265 $(A_6 - Y_1)$
20832 $(F_1 - Z_7)$	17410 $(F_1 - Y_3)$	18400 $(A_1 - X_1)$	17143 $(A_1 - Y_2)$
20900]	17545 $(Y_2 - Y_4)$	18388 $(A_3 - X_2)$	17100 –
20952] $(F_1 - Z_1)$	17672 $(F_2 - Y_1)$	18310 $(A_3 - X_5)$	
20990 $(F_2 - Z_3)$	17877 $(F_6 - Y_1)$	18290 $(A_4 - X_7)$	
21108 $(F_4 - Z_4)$	17980 –		

been observed at considerably high Dy concentrations in various crystalline and glassy [20] hosts. The Dy concentration in our case is probably too small to cause any self-quenching.

The two observed fluorescence lines are seen to split into several Stark components when the slit width of the spectrometer is reduced and the laser power is increased. The spectral peaks observed at 482 nm and at 572 nm show five components each. The individual components could be assigned on the basis of the energy level data from Dieke [21] and they are shown in figure 5. Their assignments are given in table 3.

3.2 *Fluorescence spectra of Tb^{3+} and Tb^{3+}-Er^{3+}*

The fluorescence spectra of Tb^{3+} doped calibo glass recorded at room and at liquid nitrogen temperature show seven emission lines at 491.1, 545.1, 588.1, 624.2, 654.0, 667.0 and 678.8 nm corresponding to all the seven components of ${}^7F_j$ which is rare. They are assigned to ${}^5D_4 \rightarrow {}^7F_j$ $(j = 6, 5, 4, \ldots, 0)$ transitions of Tb^{3+} and are shown in figures 2 and 3. The fluorescence spectrum at liquid nitrogen temperature is sharper than the one at room temperature thereby emphasizing the role of the host matrix lattice vibrations in causing the line broadening. The fluorescence yield in Tb^{3+} is maximum for an excitation wavelength of 488.0 nm because the energy of the ${}^5D_4$ $(\sim 20462\,\mathrm{cm}^{-1})$ level of Tb^{3+} above its ground state is closed to the exciting photon energy $(\sim 20491\,\mathrm{cm}^{-1})$.

Addition of Er^{3+} reduces the intensity of the fluorescence lines of Tb^{3+}. At 5 mol % of Er^{3+}, the ${}^5D_4 \rightarrow {}^7F_2$ peak of Tb^{3+} which appears as a single broad peak at lower Er^{3+} concetrations split into two well defined peaks. Though ${}^4F_{7/2}$ level of Er^{3+} lie very close to the ${}^5D_4$ level of Tb^{3+}, it is difficult to say that the extra peak is due to transition from ${}^4F_{7/2}$ level of Er^{3+} to its lower level. The near equality of the energy difference between the ${}^5D_4$ level $(\sim 20462\,\mathrm{cm}^{-1})$ of Tb^{3+} from its ground state to that of the ${}^4F_{7/2}$ level of the Er^{3+} (see figure 6), permits efficient energy transfer from Tb^{3+} to Er^{3+}. The slight mismatch in the two energy differences may be compensated for by the host lattice phonons. The ${}^4F_{7/2}$ level of Er^{3+} is a fluorescing level but it is surprising that it does not give any line due to its de-excitation in the spectral region 480–740 nm in calibo host. Joshi and Joshi [22] and Joshi *et al* [23] have made a similar study for energy transfer from Eu^{3+} to Er^{3+} and from Tb^{3+} to Er^{3+} in calibo and sodium phosphate glasses

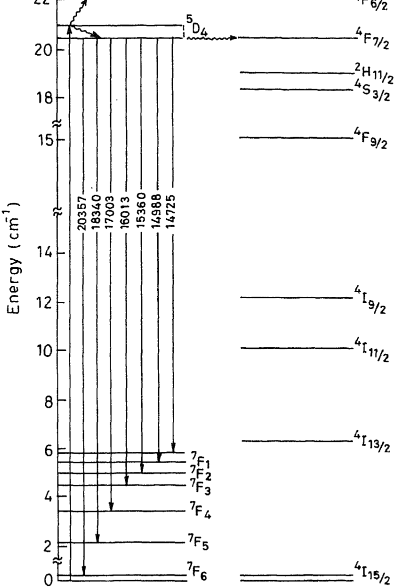

Figure 6. Energy transfer scheme of Tb^{3+} and Er^{3+} in calibo glass.

observed. It appears that Er^{3+} in the $^4F_{7/2}$ level relaxes rapidly to the $^4I_{13/2}$ level (metastable state) which then decays through the transition $^4I_{13/2} \rightarrow ^4I_{15/2}$ at 1.5 µm in the IR region which is a lasing transition. The energy levels of Tb^{3+} and Er^{3+} are shown in figure 6.

The spectral peak observed at 545.1 nm ascribed to the transition $^5D_4 \rightarrow ^7F_5$ of Tb^{3+} is very intense and we have succeeded in recording Stark splittings in it by increasing the input laser power and by reducing the slit width of the monochromator. Five Stark components are seen in this line while for the other $^5D_4 \rightarrow {}^7F_4$ transition two lines are seen at 583.3 nm and 579.2 nm. Assignments of the observed Stark splitted components, have been made on the basis of the known energy levels of the triply

Donor (%)	Acceptor (%)	Average distance (A)	Lifetime (τ) ms	Intensity (I_d)	n_τ	$P_{da} \times 10$ sec^{-1}
Dy^{3+}	Ho^{3+}					
1	0	—	1.012	39 (I_{d0})		
	1	19.8	0.726	28	0.28	0.389
	2	17.2	15.5	20	0.48	0.814
	3	15.5	0.427	16	0.58	1.354
Tb^{3+}	Er^{3+}					
2	0	—	1.4825	27 (I_{d0})		
	1	17.27	1.24	19	0.29	0.155
	2	15.70	1.01	19	0.35	0.317
	3	13.65	0.820	15	0.45	0.546
	5	12.32	0.510	4.2	0.85	1.766

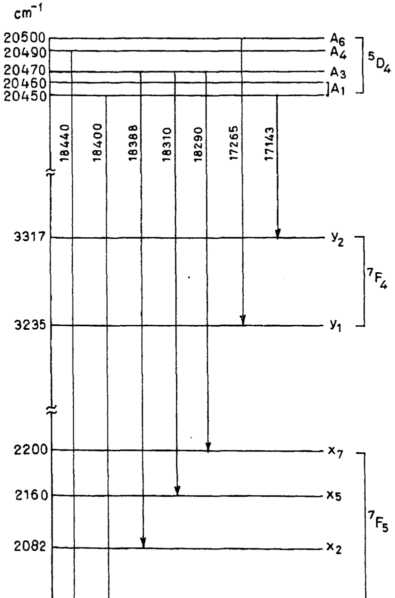

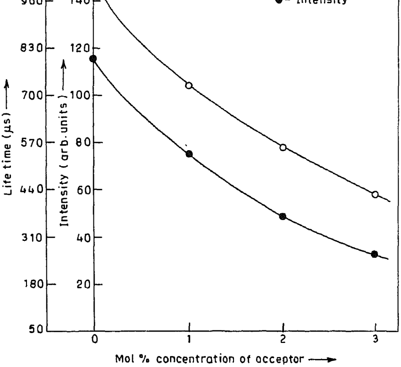

Figure 8a. Variation of life time and intensity with acceptor concentration for the ${}^4F_{9/2} - {}^4I_{13/2}$ transition of Dy^{3+} (with Dy^{3+} concentration 1% fixed).

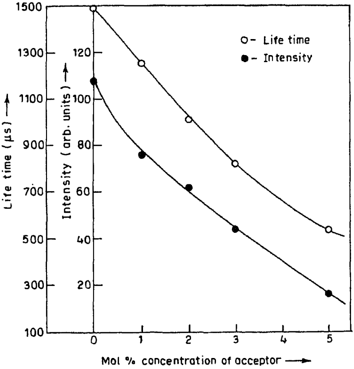

d absence of acceptor ions Ho^{3+} and Er^{3+} respectively. The life time of ${}^4F_{9/2}$ level of y^{3+} were found to be 1.012 ms and of ${}^5D_4$ level of Tb^{3+} 1.485 ms in the absence of ceptors. The life time of these levels were found to decrease in the presence of the ceptor. The life time decreases rapidly on increasing the acceptor concentrations. The riation of intensity and life time with acceptor concentration are shown in figures 8a d 8b. The absence of any line due to acceptor in the spectra indicates that the energy ansfer is non radiative.

The energy transfer probabilities (P_{da}) and energy transfer efficiencies (η_T) have been lculated employing the formula given by Reisfeld [24]

$$P_{\mathrm{da}} = 1/\tau_{\mathrm{d}}((\eta_{\mathrm{d0}}/\eta_{\mathrm{d}}) - 1) = 1/\tau_{\mathrm{d}}((I_{\mathrm{d0}})/I_{\mathrm{d}}) - 1) = (1/\tau_{\mathrm{d}} - 1/\tau_{\mathrm{d0}})$$
$$\eta_T = 1 - (\eta_{\mathrm{d}}/\eta_{\mathrm{d0}}) = 1 - (I_{\mathrm{d}}/I_{\mathrm{d0}})$$

here η_{d} and η_{d0} are the donor fluorescence quantum efficiencies in the presence and sence of the acceptor respectively (for the same donor concentration) and I_{d}, I_{d0} are the rresponding fluorescence intensities. τ_{d} and τ_{d0} are the measured decay time of the nor fluorescence in the presence and absence of the acceptor. The measured values are ven in table 4. The calculated values for the energy transfer efficiencies and energy ansfer probabilities are also given in the same table.

The mechanism responsible for energy transfer from donor to acceptor may be entified by plotting energy transfer probability (P_{da}) against the square of the donor + ceptor concentration $(C_{\mathrm{d}} + C_{\mathrm{a}})^2$. This type of plot in the two cases are given in figure 9.

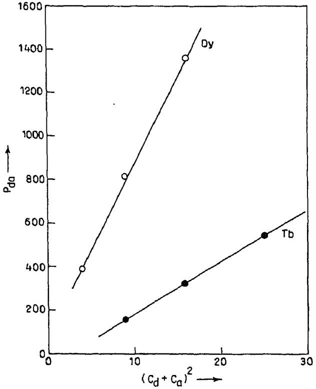

of $S = 6$ indicates that electric dipole–dipole coupling is the predominant interaction mechanism for energy transfer. At very large concentration of acceptor a deviation from the linearity is marked. Such a deviation may be due to some other mechanism which has started taking place in the glass with the larger acceptor concentration. This is also supported by an abrupt decrease in fluorescence intensity of Tb^{3+} when the concentration of Er^{3+} is 5%.

5. Conclusion

Fluorescence spectra of Dy^{3+}, $Dy^{3+} + Ho^{3+}$, Tb^{3+} and $Tb^{3+} + Er^{3+}$ have been studied at different concentration of Ho^{3+} and Er^{3+}. From the variation in intensity of the spectral lines it is concluded that Dy^{3+} and Tb^{3+} are good sensitizers for Ho^{3+} and Er^{3+} ions in calibo glass hosts. The lifetime of the ${}^4F_{9/2}$ level of Dy^{3+} and ${}^5D_4$ level of Tb^{3+} in presence and absence of acceptor Ho^{3+} and Er^{3+} respectively have been measured. From this it is concluded that a non-radiative energy transfer is taking place and the mechanism is electric dipole–dipole. Stark splitting have been marked in some of the strong transitions of the two.

Acknowledgement

The authors are grateful to CSIR and DST (under National Laser Centre Programme) for financial assistance.

References

[1] R Reisfeld and C K Jorgensen, *Lasers and excited states of rare earths* (Springer Verlag, 1977) vol. 1, p. 77
[2] R Reisfeld and Y Eckstein, *J. Non-Cryst. Solids* **11**, 611 (1973)
[3] H B Tripathi, A K Agarwal, H C Kandpal and R Belwal, *Solid State Commun.* **28**, 807 (1978)
[4] J C Bourcet and F K Fong, *J. Chem. Phys.* **60**, 34 (1974)
[5] J P Vander Ziel, L Kopt and L G Van Uitert, *Phys. Rev.* **B6**, 615 (1972)
[6] T Forster, *Ann. Phys.* **2**, 55 (1948)
[7] D L Dexter, *J. Chem. Phys.* **21**, 836 (1953)
[8] F K Fong and D J Diestler, *J. Chem. Phys.* **56**, 2815 (1972)
[9] B C Joshi *J. Non-Cryst. Solids* **45**, 1 (1981)
[10] J C Joshi, B C Joshi, N C Pandey, U C Pandey and J Joshi, *J. Solid State Chem.* **2**, 26 (1978)
[11] B C Joshi and U C Pandey, *Phys. Chem. Solids* **50**, 599 (1989)
[12] E Nakazava and S Shionoya, *J. Chem. Phys.* **47**, 3211 (1967)
[13] T C Pant, B C Bhatt and D D Pant, *J. Lumin.* **10**, 323 (1975)
[14] L G Van Uitert, *J. Lumin.* **4**, 1 (1971)
[15] B Sharma, S B Rai, D K Rai, and S Buddhudu, *Indian J. Engg. Mat Sci.* **2**, 297 (1995)
[16] R Reisfeld, A Hanigbaum, G Michaeli, L Harel and M Shalom, *Ish. Israel J. Chem.* **7**, 613 (1969)

[22] J Joshi and J C Joshi, *Indian J. Phys.* **60**, 217 (1986)
[23] J C Joshi, B C Joshi, N C Pandey, R Belwal and J Joshi, *Solid State Chem.* **22**, 439 (1977)
[24] R Reisfeld, *Structure and Bonding* **30**, 65 (1976)

Laser optogalvanic spectroscopy of argon in the wavelength region 605–740 nm

R C SHARMA, T KUNDU* and S N THAKUR
Laser Spectroscopy Laboratory, Physics Department, Banaras Hindu University, Varanasi 221 005, India
* Department of Physics, Indian Institute of Technology, Mumbai 400 076, India

MS received 5 November 1996; revised 23 January 1998

Abstract. Two-photon optogalvanic transitions in Ar glow discharge with Nd : YAG laser pumped dye laser excitation in the frequency range 13520–16520 cm^{-1} has been studied using linear and circular polarization. The intensities of two-photon optogalvanic transitions are very sensitive to changes in the incident laser power which is not the case with one-photon transitions. Intensity ratio for circular and linear polarized light for two photon transitions $6s'[1/2]^\circ 1 \leftarrow 4s[3/2]^\circ 2$, $6s'[1/2]^\circ 0 \leftarrow 4s[3/2]^\circ 2$, and $5d[1/2]^\circ 0 \leftarrow 4s[3/2]^\circ 2, 5d[1/2]^\circ 1 \leftarrow 4s[3/2]^\circ 2$ are quite different from the other two-photon transitions. This has been explained as due to near one photon resonance of $4p'[3/2]1$ level for the first pair and $4p'[1/2]1$ for the second pair of transitions. The ratio of optogalvanic intensity for circular to linear polarized light has been theoretically estimated and compared with the observed results.

Keywords. Optogalvanic spectrum; two-photon transitions; laser spectroscopy.

PACS Nos 52.80; 42.60

1. Introduction

Optogalvanic spectroscopy of glow discharges is based on the detection of small changes in the plasma-impedance, with high signal to noise ratio. This change of impedance is caused by resonant absorption of monochromatic radiation from the tunable laser, by atomic or molecular species in the plasma. Hollow cathode discharges have been found particularly suitable for such studies on the excited electronic states and rare gas filled commercial hollow cathode lamps have also been used for the wavelength calibration of dye lasers [1–3]. Extensive studies of neon optogalvanic spectra have led to a great deal of information on its one-photon and two-photon transitions [2, 3]. In contrast, there are no reports on the two-photon optogalvanic transitions in argon in spite of several studies of its one-photon optogalvanic spectra [4–7]. There are also no systematic investigations of the extreme red end of the Ar optogalvanic spectrum apart from identification of about ten one-photon lines spread over the 695–795 nm region [4]. We report here, for the first time, two-photon optogalvanic transitions in Ar with Nd : YAG laser pumped dye laser excitation in the wavelength transitions region 605–740 nm (16520–13520 cm^{-1}). The (model YG681C) pumped a Lambda Physik dye laser (model LPD3002) at 10 Hz with energy per pulse 250 mJ. Three different laser dyes in methanol were used: LDS-730 (740–720 nm, region I), LDS-698 (720–670 nm, region II) and DCM (670–605 nm, region III). The spectral bandwidth of the dye laser was 0.2 cm^{-1} with energies (at the peak of the dye laser output) per pulse (5 ns duration) of 35 mJ in region I, 70 mJ in region II and 45 mJ in region III. Approximately 20% of the dye laser radiation was coaxially directed into a Hamamatsu Ar-hollow cathode lamp (model L233-Fe) which was connected to a regular d.c. power supply (Keithley model 246) through a current limiting resistance of 2.5 kΩ. The voltage across the lamp could be set between 180 and 200 volts for normal glow discharge and the optogalvanic voltage change of the discharge was monitored across a 2.5 kΩ resistance using a coupling capacitor of 5 μF. The laser beam spot was smaller than the cathode diameter of the lamp and the unfocused laser beam was carefully aligned so as not to fall on the metal surface. Our attempts to focus the laser beam (even weakly), in the glow discharge, led to pronounced instabilities in the optogalvanic signal.

The optogalvanic signal were monitored on an oscilloscope (Tektronix model 2465A) and simultaneously processed by a boxcar averager (model SR250); both units were

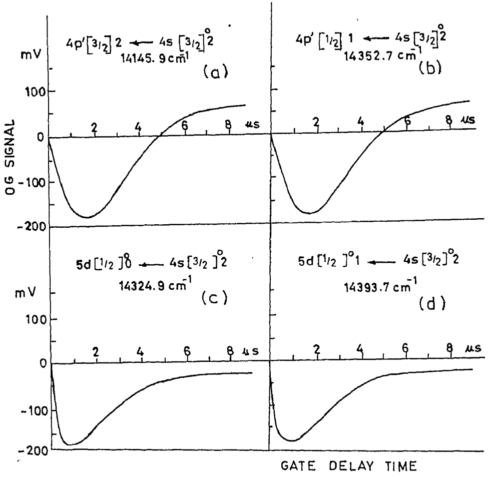

Figure 1. Oscilloscope traces of optogalvanic signals in argon corresponding to composite negative and positive voltage profiles (a and b) and only negative voltage

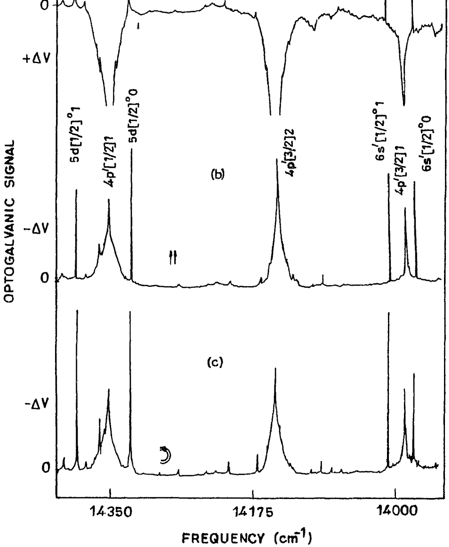

Figure 2. Optogalvanic spectra of Ar with a boxcar gate delay of (**a**) 13 μs (linear polarization) (**b**) 2 μs (linear polarization) and (**c**) 2 μs (circular polarization).

triggered by a photodiode receiving a small fraction of the incident dye laser pulse. A general survey of the temporal profile of the signals at several wavelengths showed that they could be grouped into two types as shown in oscilloscope traces in figure 1. The first group of transitions exhibit a negative voltage profile with a minimum at 1 μs from the excitation laser pulse and asymptotically increase to 0 after about 20 μs (figure 1c, d). The second group of optogalvanic transitions exhibit a composite voltage profile which starts with the negative voltage signal, becomes minimum after 2 μs then increases to a maximum positive voltage after 10 to 15 μs and asymptotically decreases to 0 at the end of 50 μs (figure 1a, b). The boxcar processed optogalvanic signals were recorded on a chart recorder with the dye laser grating scan rate of 0.3 nm/min. Figure 2 shows the optogalvanic spectra in the frequency region 13950–14400 cm^{-1} (717–694 nm) recorded with the boxcar gate width of 2 μs and two different gate delays from the exciting laser

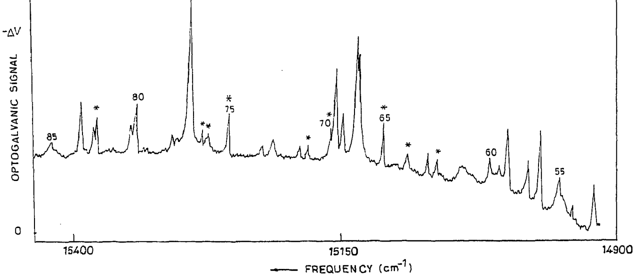

Figure 3. Optogalvanic spectrum of argon with a boxcar gate delay of 4 μs (linear polarization). The numbers within brackets correspond to serial number of transitions as in table 1 and (*) denote two-photon lines.

transitions are greatly diminished for the longer boxcar delay (figure 2a) and the optogalvanic signals for the second group become positive in polarity. It was found that the maximum number of Ar lines (all with the negative voltage signals) in any dye laser region were simultaneously recorded by setting the boxcar gate delay between 2 μs and 4 μs. The spectrum shown in figure 3 in the frequency region 14900–15400 cm^{-1} (650–670 nm) is a part of the optogalvanic spectra in the DCM dye region (region III) recorded with the gate delay of 4 μs.

3. Spectroscopic assignments

The frequencies of the observed spectral lines were determined by fitting a second degree polynomial to the measured line positions with a maximum uncertainty of 1 cm^{-1}, these are given in the first column of table 1. The relative optogalvanic intensities (estimated from peak height for linearly polarized light) are given in the second column but these are not normalized for the spectral power variations of the dye laser output and in the case of overlapping transitions the relative intensities in the two dye regions are also shown (within bracket). The upper and lower energy levels of the transition, in Racah notation [8], are given in the third and fourth columns respectively and the transition type (one or two-photon) is shown in the fifth column. In region II, the relative intensities of two-photon transitions were also determined for circularly polarized light and the ratio (Ω) of circular to linear polarization intensities is included in the fifth column along with the corresponding uncertainty. The spectroscopic assignments are quite straight forward in terms of the known energy levels of argon [9] and all, except ten of 142, observed lines have been satisfactorily assigned (see table 1). Some of the observed lines have two

Frequency (cm^{-1})	Relative intensity	Assignment		Transition type (Ω)
		Upper state	Lower state	
Region I (Dye LDS-730)				
13523.2	03	$6s[3/2]^{\circ}1$	$4p[3/2]2$	OP
13539.9	18	$4p'[3/2]2$	$4s[3/2]^{\circ}1$	OP
		$7s[3/2]^{\circ}1$	$4s'[1/2]^{\circ}1$	TP
13561.4	10	$4d[7/2]^{\circ}4$	$4p[5/2]3$	OP
13595.3	12	$4d[7/2]^{\circ}3$	$4p[5/2]2$	OP
13610.5	04	$4d[3/2]^{\circ}1$	$4p[3/2]2$	OP
13664.8	07	$6s'[1/2]^{\circ}1$	$4p'[1/2]1$	OP
13673.2	04	$6s[3/2]^{\circ}1$	$4p[3/2]1$	OP
13705.4	14	$6s'[1/2]^{\circ}1$	$4s[3/2]^{\circ}1$	TP
13722.1	05	$4d'[3/2]^{\circ}1$	$4p'[3/2]2$	OP
13745.8	35	$4p'[1/2]^{\circ}1$	$4s[3/2]^{\circ}1$	OP
13749.9	17	$4d[7/2]^{\circ}3$	$4p[5/2]3$	OP
13757.1	03	$7s[3/2]^{\circ}1$	$4p'[1/2]0$	OP
13760.5	05	$4d[3/2]^{\circ}1$	$4p[3/2]1$	OP
13804.9	06	$4d'[5/2]^{\circ}3$	$4s[3/2]^{\circ}2$	TP
13827.5	09	$4d[5/2]^{\circ}2$	$4p[5/2]2$	OP
13872.0	17(b)	$6s'[1/2]^{\circ}1$	$4p'[3/2]2$	OP
13880.0	05	$4d'[3/2]^{\circ}1$	$4p'[3/2]1$	OP
13930.0	05(b)	—	unassigned	
13944.4	05	$7s[3/2]^{\circ}2$	$4s'[1/2]^{\circ}0$	TP
13948.3	07	$4d[5/2]^{\circ}3$	$4p[5/2]2$	OP
Region II (Dye-LDS-698)				
13976.6	70	$6s'[1/2]^{\circ}0$	$4s[3/2]^{\circ}2$	TP (0.9 ± 0.1)
13988.3	60	$4p'[3/2]1$	$4s[3/2]^{\circ}2$	OP
14008.8	80	$6s'[1/2]^{\circ}1$	$4s[3/2]^{\circ}2$	TP (1.3 ± 0.1)
14079.2	06	$5d'[5/2]^{\circ}3$	$4s'[1/2]^{\circ}1$	TP (2.0 ± 0.1)
14091.6	11	$5d[1/2]^{\circ}1$	$4s[3/2]^{\circ}1$	TP (0.7 ± 0.2)
14104.3	04	$4d[5/2]^{\circ}3$	$4p[5/2]3$	OP
14128.2	06		unassigned	
14145.9	100	$4p'[3/2]2$	$4s[3/2]^{\circ}2$	OP
14168.4	07	$5d[3/2]^{\circ}2$	$4s[3/2]^{\circ}1$	TP (2.1 ± 0.2)
14204.5	06	$5d[7/2]^{\circ}3$	$4s[3/2]^{\circ}1$	TP (1.9 ± 0.2)
14222.3	03	$4d[5/2]^{\circ}3$	$4p[5/2]3$	OP
14231.8	02	$4d[3/2]^{\circ}1$	$4p[5/2]2$	OP
14266.5	04	$5d[5/2]^{\circ}2$	$4s[3/2]^{\circ}1$	TP (2.1 ± 0.1)
14290.5	02	$5d'[5/2]^{\circ}3$	$4s[3/2]^{\circ}1$	TP (2.0 ± 0.1)
14297.8	02	$6s[3/2]^{\circ}1$	$4p[5/2]3$	OP

(cm^{-1})	intensity	Upper state	Lower state	type (Ω)
14324.9	100	$5d[1/2]^{\circ}0$	$4s[3/2]^{\circ}2$	TP (1.1 ± 0.1)
14352.7	65	$4p'[1/2]1$	$4s[3/2]^{\circ}2$	OP
14365.0	15	$7s[3/2]^{\circ}1$	$4s[3/2]^{\circ}1$	TP (0.9 ± 0.2)
14382.0	06	$5d[3/2]^{\circ}1$	$4s[3/2]^{\circ}1$	TP (0.8 ± 0.2)
14393.7	65	$5d[1/2]^{\circ}1$	$4s[3/2]^{\circ}2$	TP (1.5 ± 0.1)
14410.0	07	$5d'[3/2]^{\circ}2$	$4s'[1/2]^{\circ}0$	TP (2.0 ± 0.2)
14445.9	13	$5d[7/2]^{\circ}4$	$4s[3/2]^{\circ}2$	TP (2.1 ± 0.2)
14471.7	20	$5d[3/2]^{\circ}2$	$4s[3/2]^{\circ}2$	TP (0.7 ± 0.2)
14475.7	05	$5d'[5/2]^{\circ}2$	$4s'[1/2]^{\circ}0$	TP (1.9 ± 0.2)
14508.7	03	$5d[7/2]^{\circ}3$	$4s[3/2]^{\circ}2$	TP (2.0 ± 0.2)
14515.3			(unassigned)	
14550.5	03	$4d[1/2]^{\circ}1$	$4p[1/2]1$	OP
14592.8	15	$5d[3/2]^{\circ}2$	$4p'[1/2]1$	OP
14592.8	04	$5d[5/2]^{\circ}3$	$4s[3/2]^{\circ}2$	TP (2.0 ± 0.2)
14648.7	09	$7s[3/2]^{\circ}2$	$4s[3/2]^{\circ}2$	TP (0.7 ± 0.2)
14785.7	10	$5d[5/2]^{\circ}2$	$4p'[1/2]1$	OP
14803.1			(unassigned)	
Region III (Dye-DCM)				
14924.5	25	$4d'[3/2]^{\circ}1$	$4p[3/2]1$	OP
		$6s'[1/2]^{\circ}1$	$4p[3/2]2$	OP
14944.5	08	$7s[3/2]^{\circ}2$	$4p'[1/2]1$	OP
14956.2	20	$5d[3/2]^{\circ}2$	$4p'[3/2]1$	OP
14972.5	40	$4p'[1/2]0$	$4s[3/2]^{\circ}1$	OP
14983.5	18	$4d'[3/2]^{\circ}2$	$4p[5/2]2$	OP
		$7s[3/2]^{\circ}1$	$4p'[1/2]1$	OP
15002.0	35	$4d'[5/2]^{\circ}2$	$4p[5/2]2$	OP**
15010.1	04	$6s'[1/2]^{\circ}0$	$4p[3/2]1$	OP
15018.1	08	$5d[3/2]^{\circ}1$	$4p'[1/2]1$	OP
15039.7	10 (b)	$5d[5/2]^{\circ}3$	$4p'[3/2]2$	OP
15065.5	09	$7s'[1/2]^{\circ}1$	$4s[3/2]^{\circ}1$	TP
15074.7	09	$6s'[1/2]^{\circ}1$	$4p[3/2]1$	OP
15093.2	08	$8s[3/2]^{\circ}1$	$4s[3/2]^{\circ}1$	TP
15114.5	30	$5d'[3/2]^{\circ}2$	$4s[3/2]^{\circ}2$	TP
15136.2	70	$4d'[5/2]^{\circ}3$	$4p[5/2]2$	OP
15137.8	75	$4d'[3/2]^{\circ}2$	$4p[5/2]3$	OP
15150.2	28	$4d[5/2]^{\circ}2$	$4p'[3/2]1$	OP
15155.7	60	$4d'[5/2]^{\circ}2$	$4p[5/2]3$	OP**
15161.2	06	$6d[1/2]^{\circ}1$	$4s[3/2]^{\circ}2$	TP
15181.8	06	$6d[1/2]^{\circ}0$	$4s[3/2]^{\circ}2$	TP
15190.1	06	$7s[3/2]^{\circ}1$	$4p'[3/2]2$	OP

Frequency (cm^{-1})	Relative intensity	Assignment		Transition type (Ω)
		Upper state	Lower state	
15213.7	09	$8s[3/2]^{\circ}1$	$4p'[1/2]0$	OP
15224.8	06	$5d[3/2]^{\circ}1$	$4p'[3/2]2$	OP
15254.0	20	$6d[7/2]^{\circ}4$	$4s[3/2]^{\circ}2$	TP
15273.6	07	$10d[5/2]^{\circ}2$	$4s'[1/2]^{\circ}1$	TP
15279.2	07	$6d'[5/2]^{\circ}2$	$4s'[1/2]^{\circ}0$	TP
15290.4	90	$4d'[5/2]^{\circ}3$	$4p[5/2]3$	OP**
15308.1	07	$7s[3/2]^{\circ}2$	$4p'[3/2]1$	OP
15342.2	25	$4d[5/2]^{\circ}2$	$4p'[1/2]1$	OP
15347.0	12	$7s[3/2]^{\circ}2$	$4p'[3/2]1$	OP
15379.1	14	$8s[3/2]^{\circ}2$	$4s[3/2]^{\circ}2$	TP
15382.5	12	$5d[3/2]^{\circ}1$	$4p'[3/2]1$	OP
15394.4	28	$4d'[3/2]^{\circ}1$	$4p[5/2]2$	OP
15426.1	05	$7s[3/2]^{\circ}1$	$4p[1/2]0$	OP
15449.2	03	$7d[7/2]^{\circ}3$	$4s[3/2]^{\circ}1$	TP
15460.8	08	$5d[3/2]^{\circ}1$	$4p[1/2]0$	OP
15491.7	03 (b)		unassigned	
15515.9	03	$9s[3/2]^{\circ}1$	$4s[3/2]^{\circ}1$	TP
15544.3	25	$6s'[1/2]^{\circ}1$	$4p[5/2]2$	OP
15580.9	100	$6s[3/2]^{\circ}2$	$4p[1/2]1$	OP
15624.8	02 (b)		unassigned	
15641.7	03 (b)		unassigned	
15657.3	75	$6s[3/2]^{\circ}1$	$4p[1/2]1$	OP
15695.1	50	$5d[1/2]^{\circ}1$	$4p[3/2]2$	OP
15706.4	30	$5d[1/2]^{\circ}0$	$4p[3/2]1$	OP
15729.8	08	$7d[3/2]^{\circ}2$	$4s[3/2]^{\circ}2$	TP
15732.8	14	$7d[7/2]^{\circ}4$	$4s[3/2]^{\circ}2$	TP
15744.8	35	$4d[3/2]^{\circ}1$	$4p[1/2]1$	OP
15785.1	03	$7d[5/2]^{\circ}3$	$4s[3/2]^{\circ}2$	TP
15790.2	03	$10s[3/2]^{\circ}1$	$4s[3/2]^{\circ}1$	TP
15813.6	13	$9s[3/2]^{\circ}2$	$4s[3/2]^{\circ}2$	TP
15832.6	07	$7d[1/2]^{\circ}1$	$4p'[1/2]0$	OP
15845.6	50	$5d[1/2]^{\circ}1$	$4p[3/2]1$	OP
15849.8	70	$5d[3/2]^{\circ}2$	$4p[3/2]2$	OP
15877.0	25	$5d'[3/2]^{\circ}2$	$4p'[1/2]1$	OP
15922.6	40	$5d[7/2]^{\circ}3$	$4p[3/2]2$	OP
15961.7	04	$6d'[7/2]^{\circ}2$	$4s[3/2]^{\circ}2$	TP
15972.1	15	$6d[1/2]^{\circ}1$	$4p'[1/2]1$	OP
16000.7	25	$5d[3/2]^{\circ}2$	$4p[3/2]1$	OP
16009.9	12	$8d[1/2]^{\circ}0$	$4s[3/2]^{\circ}2$	TP
16013.0	12	$6d[1/2]^{\circ}0$	$4p'[1/2]1$	OP

m^{-1})	intensity	Upper state	Lower state	type (Ω)
6045.4	35	5*d*[5/2]°2	4*p*[3/2]2	OP
6083.5	60	5*d*′[3/2]°2	4*p*′[3/2]2	OP
6092.9	75	5*d*[5/2]°3	4*p*[3/2]2	OP
		10*s*[3/2]°2	4*s*[3/2]°2	TP
6127.2	03		unassigned	
6165.5	25 (b)		unassigned	
6178.8	13	6*d*[1/2]°1	4*p*′[3/2]2	OP
6195.5	40	5*d*[5/2]°2	4*p*[3/2]1	OP
6202.7	55	7*s*[3/2]°2	4*p*[3/2]2	OP
		11*d*[7/2]°3	4*s*[3/2]°1	TP
6216.4	40	5*d*′[5/2]°2	4*p*′[3/2]2	OP
6242.4	50	7*s*[3/2]°1	4*p*[3/2]2	OP
6267.8	30	5*d*′[5/2]°3	4*p*′[3/2]2	OP
6276.7	17	5*d*[3/2]°1	4*p*[3/2]2	OP
6312.3	14	6*d*[3/2]°2	4*p*′[1/2]1	OP
6315.5	28	5*d*[1/2]°1	4*p*[5/2]2	OP
6318.7	14	5*d*′[3/2]°1	4*p*′[1/2]1	OP
6329.9	13	6*d*[5/2]°2	4*p*′[1/2]1	OP
6336.3	14	6*d*[1/2]°1	4*p*′[3/2]1	OP
6353.1	13	7*s*[3/2]°1	4*p*[3/2]1	OP
6376.3	50	6*d*[1/2]°0	4*p*′[3/2]1	OP
6386.0	45	7*s*′[1/2]°1	4*p*′[1/2]1	OP
6391.2	40	7*s*[3/2]°1	4*p*[3/2]1	OP
6406.2	05	8*s*[3/2]°2	4*p*′[1/2]1	OP
6413.3	30	6*d*[1/2]°1	4*p*[1/2]0	OP
6426.2	10	5*d*[3/2]°1	4*p*[3/2]1	OP
6439.1	10	8*s*[3/2]°1	4*p*′[1/2]1	OP**
6453.0	15 (b)		unassigned	
6483.9	12	6*d*[7/2]°3	4*p*′[3/2]2	OP
6498.5	25	4*d*′[3/2]°2	4*p*[1/2]1	OP**
6516.0	18	4*d*′[5/2]°2	4*p*[1/2]1	OP

b): Broad feature; **: Revised assignment from those in Ref [6].

The metastable 4*s*[3/2]°2 level accounts for more than half of the 44 two-photon esonant transitions whereas 14 of them originate in 4*s*[3/2]°1, four in 4*s*′[1/2]°0 and nly three in 4*s*′[1/2]°1 level. A partial energy level diagram of argon is given in figure 4 o explain the origin of some very intense spectral lines. The intensities of two-hoton optogalvanic transitions are very sensitive to changes in incident laser power, nlike the one photon transition. The strongest two-photon lines are observed at

Table 2. Intensity ratio (Ω) circular to linear polarized radiation of the two-photon transitions.

ition ency $^{-1}$)	Assignment		Observed (Ω)	Calculated (Ω)
	Upper state	Lower state		
.6	$6s'[1/2]^\circ 0$	$4s[3/2]^\circ 2$	(0.9 ± 0.1)	1.5
.8	$6s'[1/2]^\circ 1$	$4s[3/2]^\circ 2$	(1.3 ± 0.1)	1.5
.2	$5d'[5/2]^\circ 3$	$4s'[1/2]^\circ 1$	(2.0 ± 0.1)	1.5
.6	$5d[1/2]^\circ 1$	$4s[3/2]^\circ 1$	(0.7 ± 0.2)	1.0
.4	$5d[3/2]^\circ 2$	$4s[3/2]^\circ 1$	(2.1 ± 0.2)	1.5
.5	$5d[7/2]^\circ 3$	$4s[3/2]^\circ 1$	(1.9 ± 0.2)	1.5
.5	$5d[5/2]^\circ 2$	$4s[3/2]^\circ 1$	(2.1 ± 0.1)	1.5
.5	$5d'[5/2]^\circ 3$	$4s[3/2]^\circ 1$	(2.0 ± 0.1)	1.5
.9	$5d[1/2]^\circ 0$	$4s[3/2]^\circ 2$	(1.1 ± 0.1)	1.5
.0	$7s[3/2]^\circ 1$	$4s[3/2]^\circ 1$	(0.9 ± 0.2)	1.0
.0	$5d[3/2]^\circ 1$	$4s[3/2]^\circ 1$	(0.8 ± 0.2)	1.0
.7	$5d[1/2]^\circ 1$	$4s[3/2]^\circ 2$	(1.5 ± 0.1)	1.5
.0	$5d'[3/2]^\circ 2$	$4s'[1/2]^\circ 0$	(2.0 ± 0.2)	1.5
.9	$5d[7/2]^\circ 4$	$4s[3/2]^\circ 2$	(2.1 ± 0.2)	1.5
.7	$5d[3/2]^\circ 2$	$4s[3/2]^\circ 2$	(0.7 ± 0.2)	0.6
.7	$5d'[5/2]^\circ 2$	$4s'[1/2]^\circ 0$	(1.9 ± 0.2)	1.5
.7	$5d[7/2]^\circ 3$	$4s[3/2]^\circ 2$	(2.0 ± 0.2)	1.5
.8	$5d[5/2]^\circ 3$	$4s[3/2]^\circ 2$	(2.0 ± 0.2)	1.5
.7	$7s[3/2]^\circ 2$	$4s[3/2]^\circ 2$	(0.7 ± 0.2)	0.6

$s[3/2]^\circ 2$ level. The relative intensities of these transitions under linear and cir-
polarizations are shown in figures 2b and 2c respectively and discussed in the next
on.

ly ten of the one-photon transitions have been observed in the region II (table 1) of
h three have metastable states as their lower energy levels. They originate in
$/2]^\circ 2$ level and are very strong, probably power broadened due to high laser intensity
figure 2). The transitions originating in $4p[5/2]2$, $4p[5/2]3$ and $4p[1/2]1$ give rise to
optogalvanic signals. All the one-photon optogalvanic transitions in regions I and II
many of them in region III have been observed for the first time; for some of the
itions in region III reported earlier [6] we have noticed printing or assignment errors
ked ** in table 1).

iscussion and results

range of 10–20 ns. Temporal profile of the optogalvanic voltage signal resulting from a transition between two excited states is given by [11]:

$$\Delta V = -V_0(n_1 - n_2)[a_2 \exp(-t/T_2) - a_1 \exp(-t/T_1)], \qquad (1)$$

where a_2, $a_1 (a_2 > a_1)$ are characteristic phenomenological constants, T_2, T_1 the relaxation times and n_2, n_1 the atomic populations of the upper and lower energy levels respectively. V_0 is a constant for a particular transition and depends on its optical absorption cross section as well as the discharge and circuit parameters.

In temporal profile of the optogalvanic signals immediately after the laser excitation pulse ($t = 0$) the voltage is negative because of the dominance of the first term within the square brackets of eq. (1). This is exemplified by all the transitions shown in figure 2b. For the optogalvanic transitions with $4s[3/2]^\circ 2$ as the lower state and $4p'[3/2]2$, $4p'[3/2]1$, $4p'[1/2]1$ as upper states, the signals are positive for long time delay (figure 2a) but negative for short delay (figure 2b) after the exciting laser pulse. The composite negative and positive optogalvanic signals appear because of $T_2 < T_1$, so that the first term in eq. (1) dominates at short delays and the second term becomes more dominant for longer delays after the exciting laser pulse. This implies that the upper states of these transitions have relaxation times comparable to those of the lower states in accordance with eq. (1).

The observed ratio Ω of two-photon intensities with circular and linear polarization can be broadly grouped into two categories. For transitions with equal J for the upper and lower states $\Omega \approx 0.7$ and for those with unequal J values, it is close to 2. Four of the strongest two-photon lines, however, do not show this polarization behaviour (see table 1).

Grynberg *et al* [12] have carried out a detailed analysis of optogalvanic intensity, arising from the scalar and the quadrupolar components of the two-photon transition tensor for Doppler-free two-photon spectrum of neon. They conclude that the experimental observations on polarization characteristics do not agree with theoretical prediction unless one makes use of accurate wavefunctions for the initial, final and various intermediate states. We also qualitatively account for the observed ratio (Ω) in the following way. We have calculated the optogalvanic intensity ratios of circular to linear polarized light ($\Omega =$ circular/linear) by evaluating the contributions of scalar and quadrupolar components using the two-photon matrix given by Grynberg *et al* [12];

$$\begin{aligned}\Gamma_g &= \frac{A}{2J_g + 1} \sum_{k=0,2} \frac{|\langle eJ_e||Q^k||gJ_g\rangle|^2}{2k+1} \left(\sum |a_q^k(\varepsilon_1, \varepsilon_2)|^2\right) \\ &= \frac{A}{2J_g + 1} \Bigg[\frac{|\langle eJ_e||Q^0||gJ_g\rangle|^2}{1} (|a_0^0(\varepsilon_1, \varepsilon_2)|^2) \\ &\qquad + |\langle eJ_e||Q^2||gJ_g\rangle|^2 \left(\sum |a^2(\varepsilon_1, \varepsilon_2)|^2\right) \Bigg] \qquad (2)\end{aligned}$$

$$\left.\sum |a_q^2(\varepsilon_1,\varepsilon_2)|^2 = 2/3 \right| \quad \text{for linear polarization,} \tag{3}$$

$$\left.\begin{array}{r} |a_0^0(\varepsilon_1,\varepsilon_2)|^2 = 0 \\ \sum |a_q^2(\varepsilon_1,\varepsilon_2)|^2 = 1 \end{array}\right| \quad \text{for circular polarization,} \tag{4}$$

we get

$$\Gamma_{g(\text{circular})} = \frac{A}{2J_g+1}\left[\frac{|\langle eJ_e\|Q^2\|gJ_g\rangle|^2}{5}\right], \tag{5}$$

$$\Gamma_{g(\text{linear})} = \frac{A}{2J_g+1}\left[\frac{1}{3}\,\frac{|\langle eJ_e\|Q^0\|gJ_g\rangle|^2}{1} + \frac{2}{15}\,\frac{|\langle eJ_e\|Q^2\|gJ_g\rangle|^2}{1}\right] \tag{6}$$

and hence

$$\begin{aligned}\Omega &= \Gamma_{g(\text{circular})}/\Gamma_{g(\text{linear})} \\ &= \frac{1/5C}{1/3B + 2/15C},\end{aligned} \tag{7}$$

where

$$\begin{aligned}B &= |\langle eJ_e\|Q^0\|gJ_g\rangle|^2,\\ C &= |\langle eJ_e\|Q^2\|gJ_g\rangle|^2.\end{aligned}$$

The following derivations of Ω are valid only when there is only one intermediate real level with energy close to that of one photon.

Case 1. When J_e is different from J_g, then $|\langle eJ\|Q^0\|gJ\rangle|^2 = 0$ so that

$$\Omega = \frac{1/5}{2/15} = 1.5. \tag{8}$$

Case 2. When J_e is equal to J_g and greater than or equal to 1, then

$$R = \frac{|\langle eJ_e\|Q^0\|gJ_g\rangle|^2}{1/5|\langle eJ_e\|Q^2\|gJ_g\rangle|^2} = \frac{B}{1/5C}, \tag{9}$$

where R is the ratio of scalar to quadrupolar components, the value of R has been calculated from the Racah coefficients according to the following relation:

$$R(g, e.J_r) = \frac{1}{3(2J_g+1)\begin{bmatrix} J_e & J_g & 2 \\ 1 & 1 & J_r \end{bmatrix}^2},$$

$$R = 1 \quad \text{if } J_e = J_g = 1; \quad R = 3 \quad \text{if } J_e = J_g = 2, \tag{10}$$

$$1/15R + 2/15$$

$$\Omega = 1 \quad \text{if } R = 1; \quad \Omega = 0.6 \quad \text{if } R = 3. \tag{11}$$

The observed values of Ω for transitions at 14471.7 cm^{-1} and 14648.7 cm^{-1} as shown in table 2 are in good agreement with the calculated value of 0.6 corresponding to transitions between two levels with $J' = J'' = 2$. Similarly the observed values of Ω for transitions at 14365.0 cm^{-1} and 14382.0 cm^{-1} agree well with the calculated value of 1.0 corresponding to transitions with $J' = J'' = 1$. However, the calculated value of Ω for transitions corresponding to $J' \neq J''$ do not agree with the observations except for that at 14393.7 cm^{-1} with $\Omega = 1.5 \pm 0.1$ compared to the theoretical value of 1.5. Thus it is found that a single intermediate level approximation is not very successful in the calculation of Ω for two photon transition intensities between levels with unequal J values.

The enormously large intensity of two pairs of two-photon transitions shown in figures 2b and 2c must be due to the near resonance intermediate state (figure 4). The

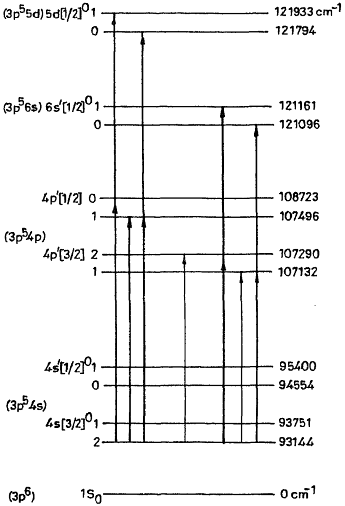

Figure 4. Partial energy level diagram of Ar showing (i) the $3p^5 4s$ metastable states, (ii) the strongest two-photon (heavy arrows) and one-photon (light arrows) transitions

tions around 14353 cm^{-1} (figure 4). Biraben *et al* [13] have also made parallel observations in optogalvanic spectrum of neon. The effects of linear and circular polarization on these two-photon optogalvanic signals are shown in figures 2b and 2c respectively. The one-photon lines located between the two pairs of two photon transition may be used as calibration marks for the change in relative intensities of the two-photon lines. The two-photon intensity ratio Ω (circular/linear) is found to be 1.5, 1.1, 1.3 and 0.9 for transitions to $5d[1/2]^\circ 1$, $5d[1/2]^\circ 0$, $6s'[1/2]^\circ 1$ and $6s'[1/2]^\circ 0$ upper levels respectively from the metastable $4s[3/2]^\circ 2$ level. This observation does not follow the polarization behaviour found for other two-photon transitions with unequal J for upper and lower states (see preceding paragraph). The near resonance of the intermediate states and the important role of collision induced ionization [14] in the generation of optogalvanic signals may be responsible for unusual polarization characteristics of these transitions.

5. Conclusion

One-photon transitions exhibit a composite temporal profile with both negative and positive voltage signal whereas the two-photon transition profiles have negative voltage signal only. Linear and circular polarization studies have been carried out to distinguish different types of two-photon transitions.

A near resonant observation has been made for the first time where intermediate level in the two-photon transition happens to be a real level. This gives rise to intensity changes in the circular and linear polarizations as compared to two-photon transitions with nonresonant intermediate levels.

Acknowledgements

Experimental work was carried out in Rutgers University, USA, while (TK) and (SNT) were visiting scientists. The authors are thankful to Prof. J Philis and Dr D Guo for many suggestions to improve the manuscript. They gratefully acknowledge financial support from the Petroleum Research Fund administered by the American Chemical Society and National Science Foundation.

Reference

[1] M-C Su, S R Oritz and D L Monts, *Opt. Commun.* **61**, 257 (1987)
[2] G A Bickel and K K Innes, *Appl. Opt.* **24**, 3620 (1985)
[3] S N Thakur and K Narayanan, *Opt. Commun.* **94**, 59 (1992)
[4] J R Nestor, *Appl. Opt.* **21**, 4154 (1982)
[5] M H Bergemann and R J Saykally, *Opt. Commun.* **40**, 277 (1982)
[6] B R Reddy, P Venkateswarlu and M C George, *Opt. Commun.* **75**, 267 (1990)

[11] R Shuker, A Ben-Amar and G Erez, *J. Phys (Paris)* **44**, C7-35 (1983)
[12] G Grynberg, F Biraben, E Giacobino and B Cagnac, *J. Phys. (Paris)* **38**, 629 (1977)
[13] F Biraben, E Giacobino and G Grynberg, *Phys. Rev* **A12**, 2444 (1975)
[14] P R Berman, *Phys. Rev.* **A13**, 2191 (1976)

An electrostatic charge state selector for ion-atom collisions: Design, spectral line-shapes and performance

AMAL K SAHA, K V THULASI RAM, L C TRIBEDI, W A FERNANDES,
S D NARVEKAR, V NANAL[1], M B KURUP, K G PRASAD[2] and P N TANDON
Tata Institute of Fundamental Research, Homi Bhabha Road, Colaba, Mumbai 400 005, India
[1]Present address: Argonne National Laboratory, Argonne, Illinois 60439, USA
[2]Present address: H-316, Vaishali Garden Apartments, Tarnaka, Secunderabad 500 017, India
Email: amal@tifr.res.in

MS received 12 February 1998

Abstract. An electrostatic charge state selector has been constructed for charge transfer studies in ion atom collisions. Its design and performance have been discussed illustrating with examples of some data taken using heavy ion beams from the pelletron accelerator. Expressions for the determination of charge state fractions from the observed charge spectrum in voltage scanning mode of operation and also the line shapes have been discussed analytically in detail.

Keywords. Ion-atom collision; charge state fractions; electrostatic charge state selector; spectral line-shapes.

PACS Nos 39.90; 34.70; 34.50

1. Introduction

In ion-atom collisions several single or multi-electron transfer processes occur between the projectile and the target atoms resulting invariably in a change of the charge carried by the incident ion. It is often required to associate the observable event in the collision process to the corresponding charge state of the ion after the collision has taken place. Thus analysis of the charge state of the ion after the collision becomes necessary. The final charge state information on the ion also provides vital information in some special cases. In the case of energetic heavy ions channeled through a thin crystal, for example, the 'frozen' fraction of the incident charge state is an important parameter in deriving capture cross sections (see e.g. ref. [1]). In recent years our group has undertaken a series of investigations concerning various aspects of ion-atom collisions in a solid target. A charge state selector was required to resolve the charge states of the ion after the collision process. We describe here the construction of a simple electrostatic charge state selector and illustrate its performance with examples of some of the data taken using BARC–TIFR pelletron accelerator. Analytical derivations of the possible line-shapes of the charge spectrum and procedure for voltage up to ±50 kV could be applied. One of the plates was arranged at an inclination with respect to the other in order to avoid restrictions imposed by the parallel plate geometry thus effectively achieving higher charge dispersion than in a parallel plates arrangement. The plates were mounted in such a way that a positively charged particle is deflected in the vertical direction. The deflector electrodes were made from highly polished 74.5 cm long, 30 mm wide, and 0.5 cm thick SS plates. The distance between the plates was maintained to be 16 mm and 42 mm at the entrance and exit, respectively, by means of three sets of appropriately machined ceramic insulators. A drift space of 51 cm, which also accommodated the pumping system, was kept between the exit of the deflector plates and the Faraday cup. The vertically deflected ions were collected in a electron suppressed Faraday cup placed just behind a 2 mm high and 10 mm wide slit kept at a vertical distance of 45 mm from the undeflected beam position. A slit 1.5 mm wide and 10 mm high was placed at the entrance of the charge state selector to restrict the acceptance angle of the beam. A line drawing of the charge selector assembly is shown in figure 1. The high voltage on the plates was provided by a shielded cable which was connected via specially made high vacuum teflon feed-throughs (figure 2). The Faraday cup, behind the slits, was directly fitted to a standard vacuum feed-through which was also electrically isolated. Two externally programmable high voltage supplies were employed for providing the required voltages to the plates.

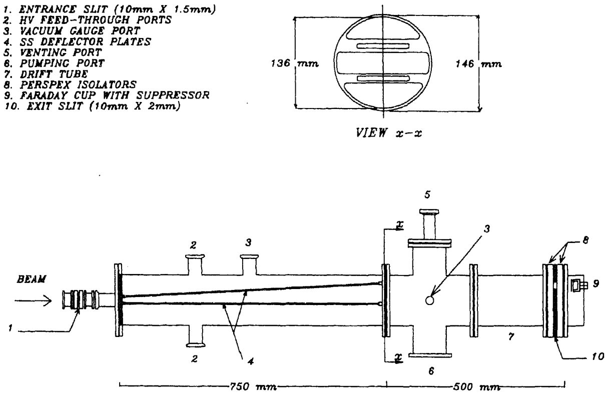

CHARGE STATE SELECTOR

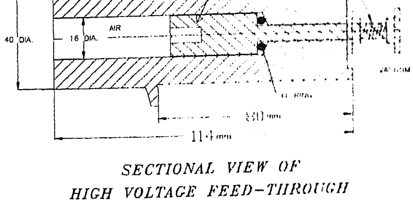

Figure 2. Details of the high voltage feed-through.

3. Control and data collection

3.1 *Modes of operation of the charge state selector*

The charge spectra can be obtained either by recording the spectra at a fixed plate voltage in conjunction with a position sensitive particle detector at the exit of the charge selector (to be incorporated in near future) or, as is done in the present case, by recording the charge transmitted through a narrow vertical slit kept at a fixed distance, as a function of the plate voltage. Let us call the first mode of operation, PSD mode and the present one, voltage scanning (VS) mode. In VS mode, the charge is collected via a specially designed Faraday cup, kept just behind the slit. The charge collected by the Faraday cup is measured using an electrometer whose output was digitized. For incident charge normalization, the electrons emitted by the rotating wire of a beam profile monitor (BPM) mounted before the scattering chamber were collected and measured in similar way by another electrometer. This arrangement was particularly suitable while using very small currents which are inevitable in the case of fully stripped ions.

3.2 *Hardware*

In order to vary the voltage on the plates of the charge selector in finite steps and collect the data at each step, a PC based system was designed. Figure 3 shows the flow chart and the functional block diagram of the control and data collection system.

The interface (I/F) board consists of address, data and control signal buffer IC's, (2 × 74 ALS 244, 74 ALS 245), an address decoder (74 ALS 138), magnitude comparator 74LS6881, two 8255 programmable peripheral I/O devices, two 8254 count down counter ICs, a 10 bit D/A converter (AD561J) along with a fast settling time (5 μs) operational amplifier (LF396) along with a sample and hold amplifier (LF 398). The buffered address lines, BA5 to BA9, are used to select the group address (300 Hex in our

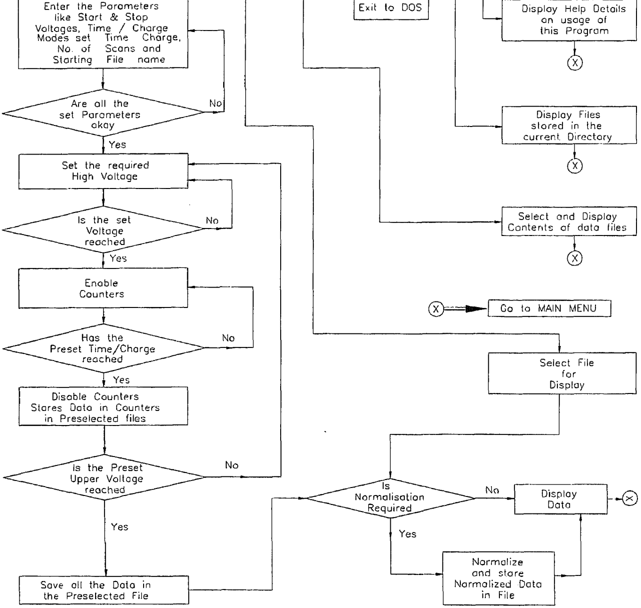
Enter the Parameters like Start & Stop Voltages, Time / Charge Modes set Time Charge, No. of Scans and Starting File name
Are all the set Parameters okay
No
Yes
Set the required High Voltage
Is the set Voltage reached
No
Yes
Enable Counters
Has the Preset Time/Charge reached
No
Yes
Disable Counters Stores Data in Counters in Preselected files
Is the Preset Upper Voltage reached
No
Yes
Save all the Data in the Preselected File
Exit to DOS
Display Help Details on usage of this Program
X
Display Files stored in the current Directory
X
Select and Display Contents of data files
X
X
Go to MAIN MENU
Select File for Display
Is Normalisation Required
No
Yes
Display Data
X
Normalize and store Normalized Data in File

Figure 3. Flow chart and the functional block diagram of the control and data collection system of the charge state selector.

address lines BA0 and BA1. Each of the two 8255 ICs on the I/F board has three ports (A, B and C). One of the 8255 (CS1) is used to operate the D/A converter (8 bits of port A and 2 bits of port B together form 10 bits to drive the DAC). The output from the DAC is given to the operational amplifier LF 356, which gives a +ve output in the range of (0–5 V) or (0–10 V) selectable by a dip switch. An inverter is provided for −ve analog voltages of the same range. A sample and hold (S/H) amplifier serves to generate a steady DC signal for driving the programmable HV supplies. The functions of the S/H amplifier are: (i) to isolate the output signal from the input signal while the input bits of incorporated for limiting the high voltage on the plate to a safe level. This also protects the high voltage supply from software mistakes and hardware faults which would lead to full 50 kV on each plate causing sparks. We have provided one more 8255 (CS0) for control and operation of other devices (like stepper motors etc.) in future.

In order to collect data from various devices like Faraday cups, detectors, current integrators, timers etc., six 16 bit count down counters are provided using two 8254 ICs (CS2 and CS3). As soon as the plate voltage is set, the counters are loaded with maximum count length (max value of 16 bits) and are enabled. These counts are down counted. The data is fed at the i/p of each counter in the form of serial TTL pulses. After a preset time or counts is reached, the counters are disabled, the data from the counters are read to obtain the actual counts and stored in files. All the data IN and OUT are transferred using the buffered data lines BD0–BD7. The read and write instructions from the PC are given by the BIOR and BIOW lines through the decoder. Simultaneously, the plate voltage is incremented to the next value and the cycle is repeated. The counters are enabled or disabled using the PC1 and PC0 lines of the port C of the first 8255 (CS1) device. After the data collection at the highest preset value of the plate voltage, the complete data is transferred to a previously named file in the PC. Also the data from counters 1 and 3 are displayed on the monitor. It is also possible to interactively normalize the data of counter 3 to the corresponding data counter 1 and display the normalized data. The whole set of data collection with same parameter can be repeated interactively by a single key.

3.3 *Software*

A user friendly menu driven interactive software using 'Basic' was written. This software provides several options, which are briefly described below:

Scan: Using this option the plate voltages (both positive and negative) can be set to vary simultaneously with a common control between two limits in finite steps. Six set of charge data collected on various slits, FC etc. or particles detected in the counters can be recorded at each step for a given time interval or for a preset number of incident particles. Once the selected voltage scan is completed, the number of contents of the two counters are displayed as a function of the applied voltage. Simultaneously, the data from all counters are stored in a file. The data of one of the counters could be normalized with respect to the other counter at each voltage step and can be viewed. The scan with same input parameters can be repeated several times either automatically or interactively.

Display: This option allows the data of two files stored earlier to be displayed.

View: In this option the data from all counters recorded earlier in a file along with various parameters used are displayed on the monitor screen of the PC.

Files: Various files existing in a directory can be viewed using this option.

Help for Menu: This option describes the details of various options in the menu.

beam of charge q and energy E in the plates of length l and a drift region l_{drift} can be expressed as

$$s = y_{\text{inc}} + (l + l_{\text{drift}}) \tan \alpha_{\text{inc}} + \frac{qV}{2E} \frac{l^2}{d_e - d_0} \left[\left\{ \frac{d_e}{d_e - d_0} + \frac{l_{\text{drift}}}{l} \right\} \ln \left(\frac{d_e}{d_0} \right) - 1 \right], \tag{1}$$

where V is the applied voltage difference between the plates and d_0 and d_e are the distances between the plates of the charge selector at the entrance and exit, respectively. y_{inc} is the transverse displacement of the charged particle from the optic axis and α_{inc} is the angle of incidence with respect to the optic axis. Let us introduce the constants C_1 and C_2 so that s can be expressed as

$$s = y_{\text{inc}} + C_1 \tan \alpha_{\text{inc}} + C_2 \left(\frac{qV}{E} \right). \tag{2}$$

C_1 and C_2 are functions of the geometrical parameters of the charge state selector only. The deflection s can be obtained directly in mm when one expresses l, d_e, d_0, and l_{drift} in mm, the projectile energy E in MeV, the voltage V in kilo-Volts and the projectile charge q in eletronic unit.

As already mentioned, the charge state of the incident ion may change during the collision with the target atoms and a distribution of charge states is produced after the collision. In this section we derive the fractions of post-collision charge states which enter the selector and also their spectral line shapes.

Typical charge spectra normalized to the number of ions incident on the target are shown in figures 4, 5 and 7. In the absence of any spread in the transverse position and the angle of the beam, the charge spectrum would have been a step function of the applied plate voltage (V). It is the distribution of transverse position and the angular spread of the beam with respect to the exit slit that determines the shape of the spectrum. In the PSD mode of operation, the spectrum would be the exact map of the distribution of transverse position of the particles. In the voltage scanning mode, however, at each voltage point, a position integral, between the edges of the exit slit, of the position distribution of the beam on the exit slit plane is obtained. It should be noted that there is always some overlap in the integrals of the position distribution at successive voltage points. One needs, therefore, to deconvolute the voltage mode spectrum to find the fraction of particles of different charge states.

Let us assume that there are particles of different charge states q's passing through the charge selector. Let N_q be the number of particles of charge state q entering the selector at any plate voltage. In the voltage mode charge spectrum, $F(V)$ is the total charge passing through the exit slit at the applied plate voltage V and collected by the Faraday cup behind the exit slit.

If $f_q\,(V)$ be defined as the contribution of particles of charge state q to the total charge $F(V)$ at the voltage point V, then

$$F(V) = \sum f_q(V) \tag{3}$$

Let $p(y_{\text{inc}}, \alpha_{\text{inc}})$ be the probability density function describing the charge independent distribution of the divergence parameters y_{inc} and α_{inc}.

$$f_q(V) = \iiint q \cdot N_q \cdot \mathrm{d}y_{\text{inc}}\, \mathrm{d}\alpha_{\text{inc}}\, p(y_{\text{inc}}, \alpha_{\text{inc}}) \mathrm{d}s \times \delta\left(s - \left(y_{\text{inc}} + C_1 \tan\alpha_{\text{inc}} + C_2 \frac{qV}{E}\right)\right) W(s), \tag{4}$$

where

$$W(s) = \theta(s - s_1) - \theta(s - s_2) \tag{5}$$

is the window function representing the exit slit with edges at s_1 and s_2, $s_2 > s_1$. Here

$$\begin{aligned} \theta(x) &= 1 \quad \text{if } x > 0 \\ &= 0 \quad \text{otherwise.} \end{aligned}$$

Therefore, by change of variable $u = C_2(qV/E)$

$$\int f_q(V)\mathrm{d}V = qN_q \iiiint \mathrm{d}y_{\text{inc}}\, \mathrm{d}\alpha_{\text{inc}}\, \mathrm{d}V\, \mathrm{d}s\; p(y_{\text{inc}}, \alpha_{\text{inc}}) W(s) \times \delta\left(s - \left(y_{\text{inc}} + C_1 \tan\alpha_{\text{inc}} + C_2 \frac{qV}{E}\right)\right) \tag{6}$$

$$= \frac{EqN_q}{C_2 q} \iiiint \mathrm{d}y_{\text{inc}}\, \mathrm{d}\alpha_{\text{inc}} \mathrm{d}s\, \mathrm{d}u\; p(y_{\text{inc}}, \alpha_{\text{inc}}) W(s) \times \delta(s - (y_{\text{inc}} + C_1 \tan\alpha_{\text{inc}} + u)). \tag{7}$$

And

$$\int f_q(V)\mathrm{d}V = \frac{EN_q}{C_2} I, \tag{8}$$

where

$$I \equiv \iiiint \mathrm{d}y_{\text{inc}}\, \mathrm{d}\alpha_{\text{inc}}\, \mathrm{d}s\, \mathrm{d}u\; p(y_{\text{inc}}, \alpha_{\text{inc}}) W(s) \delta(s - (y_{\text{inc}} + C_1 \tan\alpha_{\text{inc}} + u)). \tag{9}$$

The value of the integral I is independent of the charge state and depends only on $p(y_{\text{inc}}, \alpha_{\text{inc}})$ and the geometrical constants of the charge selector.

By similar change of variable, it is easy to show that (for a given energy)

$$\int f_q(V) g(qV) \mathrm{d}V = kN_q, \tag{10}$$

$$g(qV) = \text{any function of } qV, \tag{11}$$

$$k = \text{constant independent of } q. \tag{12}$$

suggested. The charge state fractions i.e. $N_q/\sum_q N_q$ can therefore be obtained directly from the areas under the peaks for different charge states. It may be noted that in PSD mode, the area under individual charge profile obtained by integrating the profile over the variable s would also be proportional to N_q.

In the special case of Gaussian distribution

$$p(y_{\text{inc}}, \alpha_{\text{inc}}) = \frac{1}{\sqrt{2\pi\sigma^2_{\alpha_{\text{inc}}}}} \exp\left[-\frac{\alpha^2_{\text{inc}}}{2\sigma^2_{\alpha_{\text{inc}}}}\right] \frac{1}{\sqrt{2\pi\sigma^2_{y_{\text{inc}}}}} \exp\left[-\frac{y^2_{\text{inc}}}{2\sigma^2_{y_{\text{inc}}}}\right], \tag{13}$$

it can be shown by explicit evaluation of the integral that

$$f_q(V) = qN_q \frac{1}{2}\left[\operatorname{erf}\left(\frac{s_2 - C_2\frac{qV}{E}}{\sqrt{\sigma^2_{y_{\text{inc}}} + \sigma^2_{\alpha_{\text{inc}}} C_1^2}}\right) - \operatorname{erf}\left(\frac{s_1 - C_2\frac{qV}{E}}{\sqrt{\sigma^2_{y_{\text{inc}}} + \sigma^2_{\alpha_{\text{inc}}} C_1^2}}\right)\right]. \tag{14}$$

It is worth investigating two limits of the above results.

I. *Narrow exit window*: When $(s_2 - s_1) \ll \sqrt{\sigma^2_{y_{\text{inc}}} + \sigma^2_{\alpha_{\text{inc}}} C_1^2}$,

$$f_q(V) = \frac{qN_q}{2} \frac{(s_2 - s_1)}{\sqrt{\sigma^2_{y_{\text{inc}}} + \sigma^2_{\alpha_{\text{inc}}} C_1^2}} \frac{1}{\sqrt{2\pi}} \cdot \exp\left[-\frac{\left(V - \frac{s_1+s_2}{2}\frac{E}{C_2 q}\right)^2}{2\left(\frac{E\sqrt{\sigma^2_{y_{\text{inc}}} + C_1^2\sigma^2_{\alpha_{\text{inc}}}}}{C_2 q}\right)^2}\right]. \tag{15}$$

That is, $f_q(V)$ is a Gaussian with peak at

$$V_q = \frac{s_1 + s_2}{2} \frac{E}{C_2 q} \tag{16}$$

and

$$\text{FWHM} = 2.35\, \frac{E\sqrt{\sigma^2_{y_{\text{inc}}} + C_1^2\sigma^2_{\alpha_{\text{inc}}}}}{C_2 q}. \tag{17}$$

It may be noted that the peak height of $f_q(V)$ is proportional to qN_q with the constant of proportionality being equal for all the charge states. So the peak heights can also be used to find the charge state fractions.

II. *Wide exit window*: When $(s_2 - s_1) \gg \sqrt{\sigma^2_{y_{\text{inc}}} + \sigma^2_{\alpha_{\text{inc}}} C_1^2}$,

$$f_q(V) = qN_q \quad \text{at } V \text{ around } V_q \equiv \left(\frac{s_1 + s_2}{2}\right) \cdot \frac{E}{C_2 q} \tag{18}$$

5.1 *Experimental setup*

The performance of the charge selector was checked using a setup discussed in our earlier papers [1, 2]. Briefly, a highly collimated beam of energetic heavy ions in a given charge state obtained from the 14 MV pelletron accelerator at Mumbai was made to fall on a target mounted inside an electrically isolated scattering chamber. In some cases the ions were further stripped using a post accelerator foil stripper [3]. The targets used were thin carbon foils of varying thicknesses mounted on a target wheel [4]. The scattered beam at 0° entered the charge selector through an isolated vertical $1.5 \times 12\,\mathrm{mm}^2$ slit, mounted just before the plates. The charge state distribution of the scattered beam was measured by deflecting it as a function of the voltage on the plates. The deflected beam, transmitted through a horizontal slit 10×2 mm, was collected on a Faraday cup. A beam profile monitor, placed before the scattering chamber, was used to normalize the charge of the incident beam by measuring the number of emitted electrons from the BPM cathode wire. All the charge collected were digitized using AD converters which were specially designed and made such that they could be used even when the incident beam intensity is very low in the measurement. Since the AD converters were sensitive to only one polarity, a dc offset was helpful in averaging out small negative pickup by the electrometer. The charge spectra as a function of the plate voltage were recorded several times for a particular incident charge state and energy. They were normalized for a fixed incident charge for further analysis.

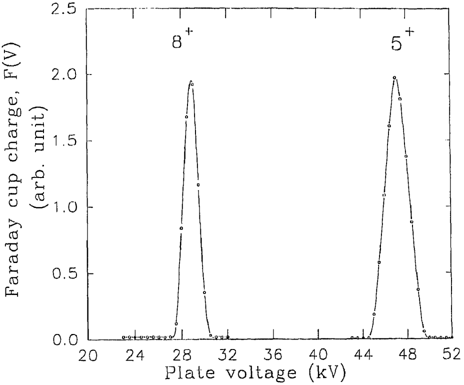

by direct acceleration or by allowing the beam to go through a post-stripper [4] and

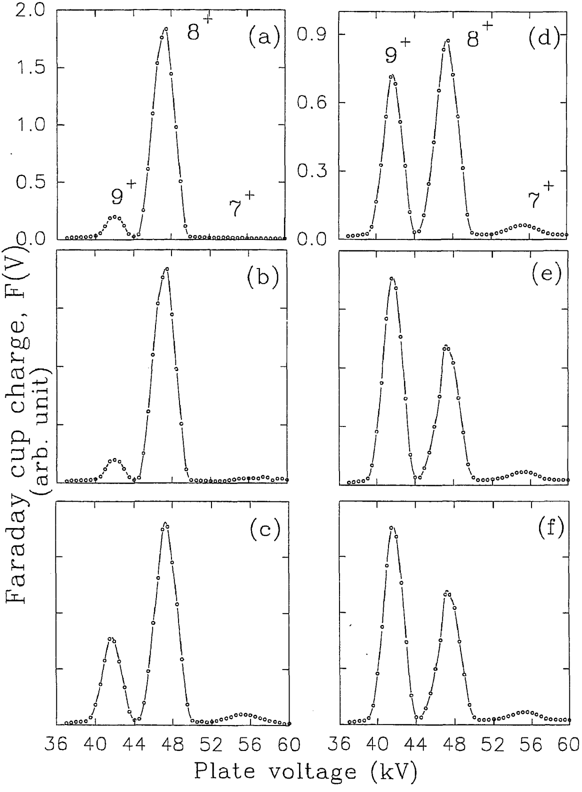

Figure 5. Normalized charge spectrum as in figure 4 with 96 MeV F^{8+} ions incident on C foil of thickness: **(a)** 1.5, **(b)** 2, **(c)** 5, **(d)** 10, **(e)** 20 and **(f)** 30 $\mu g/cm^2$.

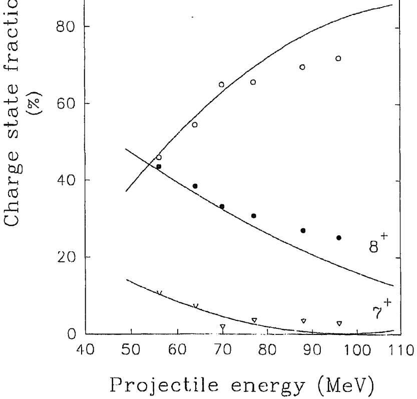

Figure 6. Charge state fractions obtained from the spectra taken with the charge state selector for F^{8+} ion incident on 30 μg/cm^2 C foil as a function of energy of the projectile. The solid curves are results reported by Shima *et al* [5].

subsequently selecting the desired charge state by a switching magnet. For obtaining several charge states to go through the selector the beam was passed through a set of carbon foils of varying thickness between 1.5 and 30 μg/cm^2. Any one of the carbon foil could be brought onto the path of the beam by remote control. Some positions on the holder were left blank in order to allow ions in a definite charge state to enter the selector. Typical charge profiles obtained at the Farady cup with a 5^+ or 8^+ charge state of the incident beam are shown in figure 4 for 60 MeV F ions. The latter was obtained with the help of the post stripper foils. The observed line shape is Gaussian. The resolution in VS mode, $\Delta V/V$ where ΔV is the FWHM of the profile and V is the voltage at which the peak appears, was found to be $\sim 5.3\%$ in the present geometry for both the cases suggesting that the inherent beam quality (emittance, focussing and stripping elements) to be the deciding factor. In cases where the beam enters the selector through a carbon foil placed before the selector, because of the Coulomb interaction, the beam is split into several charge states. The charge state fractions thus obtained depend not only on the incident energy and the atomic number of the ion beam but to a significant extent on the thickness of the carbon foil used until charge equilibrium is attained (before equilibrium is reached these fractions may also depend on the incident charge state). This is nicely illustrated in figure 5 which shows the observed charge spectra for several thicknesses of

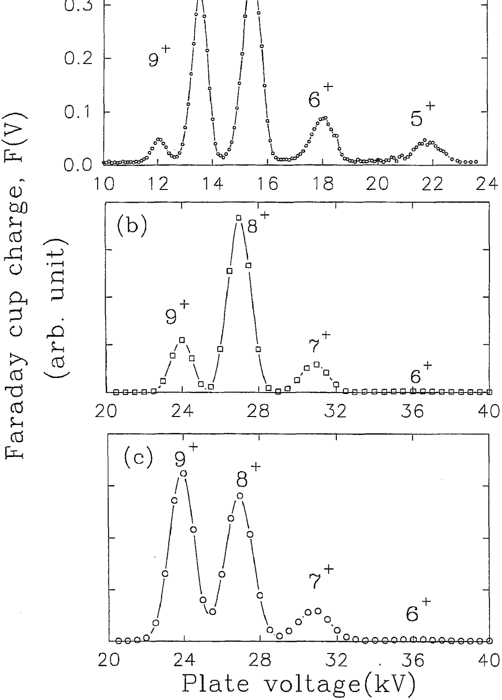

Figure 7. Normalized charge spectra, as in figure 4, with a beam of: (**a**) 24 MeV F^{8+} (obtained using gas stripper) incident on 3 μg/cm^2 C foil, (**b**) 56 MeV F^{8+} (obtained using foil stripper) incident on 3 μg/cm^2 C foil and (**c**) 56 MeV F^{8+} (obtained using foil stripper) incident on 30 μg/cm^2 C foil.

eached. From a fit to the spectra with Gaussian line shape the charge state fractions were determined (see IV). We have shown in figure 6, as a function of the incident beam energy the charge state fractions obtained with a 30 μg/cm^2 C foil. As expected, the 9^+

with that of Shima *et al.* However, as seen from the higher energy data, it is evident that charge equilibrium is not achieved with the 30 μg/cm^2 C foil used by us. The presently observed deviations at higher energies are expected to disappear had we used thicker foils. Such measurements would result in an increase of the 9$^+$ fraction with a corresponding decrease in the 8$^+$ and 7$^+$ fractions. The effect of the increased divergence of the beam due to the thickness of the C foil arising mainly due to multiple scatterings can be seen in figure 7 for F ions of 56 MeV. A comparison of the charge spectra taken with 3 and 30 μg/cm^2 foils (figures 7b and 7c) indicates the broadening of the lines caused mainly by Rutherford scattering. This is not so obvious at higher energy of 96 MeV (figure 5) where this contribution is small. Figure 7a shows the charge spectrum with 24 MeV F^{8+} obtained using gas stripper in the terminal of the accelerator to have a beam with smaller divergence. The charge spectrum taken with a 3 μg/cm^2 C foil is still very well resolved even though one expects larger line-widths due to Rutherford scattering because of the still lower energy suggesting that the beam quality before the scattering chamber is the principal factor deciding the resolution.

6. Conclusion

An electrostatic charge selector for charge state analysis has been constructed and its performance tested. The data obtained using this selector on charge state fractions of F ions after interacting with C foil are found to be in good agreement with the published data of Shima *et al* [5]. The effect of beam divergence on the experimental spectral line width is well parametrized by the analytical expressions presented here.

Acknowledgement

The authors acknowledge useful discussion on spectral line shapes and charge state fractions with R G Pillay and A A Tulapurkar.

References

[1] L C Tribedi, V Nanal, M B Kurup, K G Prasad and P N Tandon, *Phys. Rev.* **A51**, [illegible]
[2] L C Tribedi, K G Prasad and P N Tandon, *Phys. Rev.* **A47**, 3739 (1993)
[3] S D Narvekar, R R Hosangadi, L C Tribedi, R G Pillay, K G Prasad and P N [illegible] *Pramana – J. Phys.* **39**, 79 (1992)
[4] L C Tribedi, S D Narvekar, R G Pillay and P N Tandon, *Pramana – J. Phys.* **39**, [illegible]
[5] K Shima, T Mikumo and H Tawara, *Atomic Data Nucl. Data Tables* **34**, [illegible]

Total electron scattering cross sections for carbon dioxide at low electron energies

P RAWAT, K P SUBRAMANIAN and VIJAY KUMAR
Physical Research Laboratory, Navrangpura, Ahmedabad 380 009, India
E-mail: vkumar@prl.ernet.in

MS received 9 January 1998

Abstract. Absolute total electron scattering cross sections for carbon dioxide have been measured at low electron energies using a photoelectron source. The measurements have been carried out at 27 electron energies varying from 0.91–9.14 eV with an accuracy of ±3%. The cross sections obtained in the present experiment have been compared with other measurements and theoretical computations.

Keywords. Electron scattering; total cross sections; carbon dioxide.

PACS No. 34.80

1. Introduction

In recent years, there has been considerable interest in the measurement of total electron scattering cross sections of carbon dioxide, especially at low electron energies. Also, a lot of activity in the theoretical study of e-CO_2 collisions has started in the recent past. One of the reasons for such an interest lies in the fact that CO_2 plays an important role in the study of planetary atmospheres, laser fusion plasma and gas lasers. Also, this is one polyatomic molecule for which accurate low energy electron scattering cross section calculations are available.

The electron scattering cross section measurements for carbon dioxide have been carried out using various techniques. This includes the work reported by Brüche [1], Ramsauer and Kollath [2], Szmytkowski and Zubek [3], Ferch *et al* [4], Hoffman *et al* [5], Sueoka and Mori [6], Szmytkowski *et al* [7] and Buckman *et al* [8]. These measurements show an increase in cross section with decreasing electron energy below 1.8 eV and at around 70 meV, the cross sections have been found to exceed the value at the maximum of the $^2\Pi_u$ resonance at around 3.8 eV by a large factor [4]. The cross sections have also been theoretically computed by Morrison *et al* [9] using coupled channels procedure together with the adiabatic nuclei approximation. Comparison of the measured and the theoretically computed cross section values shows a general agreement helium, neon [10], argon, krypton, xenon [11], molecular hydrogen [12] and molecular oxygen [13] at electron energies from 0–10 eV. In this paper, we present the cross sections for carbon dioxide in the electron energy range between 0.91 and 9.14 eV at an electron energy resolution of 45 meV.

2. Experimental set up

The experimental set up used for the study, the method for analysis of the data and error analysis have been described in detail previously by Kumar *et al* [10] and Subramanian and Kumar [11]. In brief, the experiment consists of measuring the intensities of the peaks in the photoelectron spectra of the source gas such as argon, krypton, xenon or carbon dioxide itself. The photoelectrons thus produced by the source gas are scattered by the target gas, the cross section of which is to be determined. Each peak in the photoelectron spectrum of the source gas provides one point in the electron energy scale.

Electrons are produced by photoionization of the source gas in a small ionization region located close to the electron energy analyser. Vacuum ultraviolet photons from strong atomic emission lines are allowed to impinge on the source gas which is photoionized and electrons of different energies corresponding to the states of the ions are produced. With different combination of photons of three different wavelengths (He I 58.4, Ne I 73.6 and 74.4 nm) and argon, krypton, xenon and carbon dioxide as source gases, a large number of electron energies are accessible from 0.91 to 9.14 eV. The resonant emission lines He I (58.4 nm) and Ne I (73.6 and 74.4 nm) are produced by microwave discharge of helium and neon respectively. The intensity of the photon beam is monitored using a beam splitter which consists of a high transparency wire mesh mounted at an angle of 45° to the beam axis. More than 90% of the light is transmitted and the rest is reflected towards a light detector which includes a perspex light pipe coated at the front end with a scintillator, *p*-terphenyl, and an EMI 6199 photomultiplier. Any change in the light intensity could thus be monitored using the beam splitter, and the change in intensity, if any, during the experiment could be incorporated in the results.

The transmitted photon beam was allowed to pass through a large number of circular baffles before emerging into a small region where photoionization of the source gas takes place. The pressure of the source gas was kept low to avoid any electron scattering by the source-gas atoms/molecules. The photoelectrons thus produced were energy analysed using a cylindrical mirror analyser (CMA) and were detected by a channeltron (4029, Galileo Electro-Optics Corp., USA) operated in the counting mode. After proper amplification, the signals were stored in a microprocessor-controlled multichannel analyser operated in the multiscaling mode.

The CMA has a slit-to-slit focusing geometry and the diameter of the inner and outer cylinders were 10.2 and 25.4 cm respectively. The photoelectrons produced in the ionization region were allowed to enter the first slit of the analyser at an angle of 54°44′ ± 3°.

used to define the 55° angle over the 2π geometry, was 2.37 cm. Without any target gas, the amplitudes of the photoelectron peaks produced by the source gas were monitored at a fixed but low source gas pressure in the ionization region. The target gas was then introduced and if the source gas and target gas were not the same, the amplitudes of the photoelectron peaks would decrease with increasing target gas pressure. This decrease was attributed to electron scattering by target gas species whose number density increases with increasing pressure. When the source and target gas were the same (e.g. in case of carbon dioxide), the amplitudes of the photoelectron peaks would first increase with increase of source/target gas pressure and after a certain gas pressure was attained, the amplitudes would start decreasing with subsequent increase in gas pressure. To begin with, the increase in peak amplitudes would be due to the increase in photoelectron production rate followed by small electron scattering, but the subsequent decrease in amplitudes was because of scattering alone. The absolute gas pressure in the ionization and scattering regions was measured using an MKS capacitance manometer (head 310 MH-1). The details about pressures in different regions of the instrument have been given in a previous publication [10].

3. Method and error analysis

Using the technique described above, electron scattering cross sections for carbon dioxide have been measured at 27 energies. When source and target species are different, the electron scattering cross section σ can be evaluated by using the following equation:

$$\ln\left(\frac{I_{e2}}{I_{e1}}\frac{I_{\lambda 01}}{I_{\lambda 02}}\right) = \frac{P_1 - P_2}{760}\left[n_0\sigma x + k(al_1 + l_2)\right]. \tag{1}$$

Here I_{e1} and I_{e2} are the amplitudes of the photoelectron peak at two different target gas pressures P_1 and P_2, $I_{\lambda 01}$ and $I_{\lambda 02}$ are the incident photon intensities monitored by the beam monitor during the experiment at two pressures, l_1 is the distance from the centre of the beam splitter to the circular aperture covering the ionization region, l_2 is the distance from the same aperture to the actual ionization region defined geometrically by different slits in the accelerator region and cylindrical mirror analyser, x is the scattering path length, a is the ratio of the pressures of the target gas outside and inside the ionization region and k is the photoabsorption coefficient of the target gas at a particular photon wavelength (figure 1). The total photoabsorption coefficients for carbon dioxide at the three incident photon wavelengths have been taken from Samson and Yin [14]. The ratios of $I_{\lambda 01}$ and $I_{\lambda 02}$ were determined from the beam splitter as described previously [10].

When source and target gas species are the same, the electron scattering cross sections could be evaluated by the equation given below:

$$\ln\left(\frac{I_{e2}}{I_{e1}}\frac{I_{\lambda 01}}{I_{\lambda 02}}\frac{P_1}{P_2}\right) = \frac{P_1 - P_2}{760}\left[n_0\sigma x + k(al_1 + l_2)\right]. \tag{2}$$

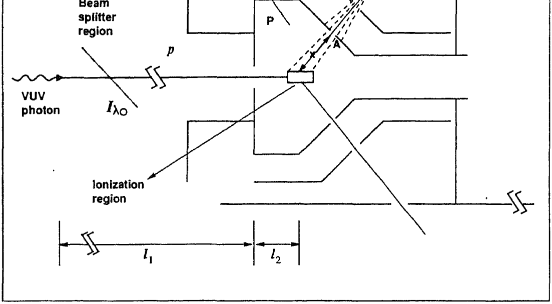

Figure 1. Schematic diagram showing ionization as well as the electron scattering region in the cylindrical mirror analyser of the photoelectron spectrometer.

present experiment was estimated to be ± 3%. The electron scattering cross sections for carbon dioxide were measured using equations (1) and (2) respectively in the two cases described above. In both these equations, all parameters $I_{e1}, I_{e2}, I_{\lambda 01}, I_{\lambda 02}, P_1$ and P_2 could be determined experimentally and cross sections could be calculated.

The problem of inadequate discrimination against forward scattered electrons is a difficult one. Such an inadequacy is due to the inability of the experimental system to discriminate low angle scattered electrons which, in general, have large amplitudes. Attempts to estimate the magnitude of this effect on the measured cross sections in a certain experimental set up becomes much more difficult as almost no experimental values of elastic and inelastic differential scattering cross sections at very low angles are available. An attempt, however, has been made in this direction for our experimental set up using a numerical simulation method.

In the present experimental set up, the geometry of the apparatus allows a full cone angle of 3° beam of electrons into the analysing region (figure 1). Taking into account the forward scattering of the electrons near the exit slit of the scattering region, it would be safe to assume that the overall angle of emergence is increased by a factor of two, giving the full cone angle of 6° around the nominal angle of projection of 54°44′.

In order to study the problem of inadequate discrimination against forward scattered electrons, a Monte Carlo method was developed. The electron trajectories originating from the ionization region and terminating at the detector were numerically studied using are produced, (ii) random angle of projection within the allowed cone of ejection determined by the geometry, (iii) spread in energy of the photoelectron determined by the thermal broadening, (iv) place nearby the first slit A (figure 1) where a chosen fraction of the emitted photoelectrons are undergoing forward scattering and (v) deflection in angle within a specified cone due to the forward scattering. Assuming cylindrical symmetry of the spectrometer, the analysis was carried out in the in-plane geometry. In the absence of values of differential cross section available at small angles, the forward scattering cross section at the exit slit was arbitrarily chosen as 100 Å^2 per steradian, which is about 6 times larger than the peak value of the measured total cross section in the present work.

The discrimination due to geometry was computed using normal trigonometrical relations. The discrimination due to the range differences are computed with the standard equation for range of electron trajectory in the analysing field of a slit-to-slit focussing type CMA given by

$$L = r_1 \times \sqrt{4\pi k}\cos\theta\exp(-k\sin^2\theta)\mathrm{erf}\,(\sqrt{k}\sin\theta). \tag{3}$$

Equation (3) has been derived by Karras *et al* [15]. The error function $\mathrm{erf}(\sqrt{k}\sin\theta)$ is defined as

$$\mathrm{erf}(x) = \frac{2}{\sqrt{\pi}}\int_0^x e^{-t^2}\mathrm{d}t,$$

where $x = \sqrt{k}\sin\theta$. The analyser constant, $k = E/eV\ln(r_2/r_1)$, E is the energy of the electron in eV, e is the electronic charge, V is bias potential applied to the analysing field electrode, θ is the angle of projection and r_1 and r_2 are the radii of the inner and outer cylinders of CMA.

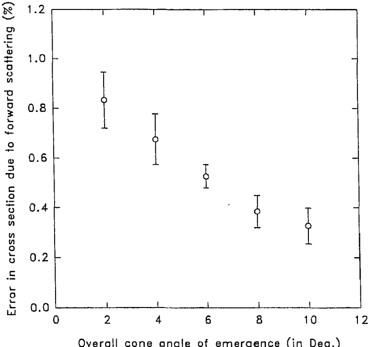

standard deviation values. Finally, similar data were generated for different angles of emergence for forward scattering giving the full cone angles of 2, 4, 6, 8 and 10°.

The result shows that the average value of error in cross section due to lack of discrimination is more or less independent of $\Delta\epsilon/E$ in the chosen range of 0.2 to 0.6%. However, it is very much dependent on the overall cone angle of emergence. The results of the present study are shown in figure 2, where the error in cross section value is plotted against the overall cone angle of emergence.

For our experimental system where the overall cone angle of emergence has been estimated to be 6°, the maximum error due to inadequate discrimination against forward scattering has been found to be about 0.5%.

4. Results and discussion

The total electron scattering cross sections for carbon dioxide as measured in the present experiment are shown in figure 3 for electron energies ranging from 0.91 to 9.14 eV along with error bars at four energies only. Also shown in the figure are the measured cross sections reported by Ferch *et al* [4], Hoffman *et al* [5], Buckman *et al* [8], and Szmytkowski *et al* [7] and theoretically computed cross sections by Morrison *et al* [9]. Transmission measurements made with an electron time-of-flight spectrometer were reported by Ferch *et al* [4] in the low electron energy region (0.07 to 4.62 eV) with an energy resolution of 10 meV at 0.07 eV and 250 meV at 3.8 eV respectively. The measurements of Hoffman *et al* [5] were carried out using a beam transmission technique at electron energies from 2–50 eV at an energy resolution of 140 meV. The retarding potential time-of-flight technique was used by Sueoka and Mori [6] and a time-of-flight technique was also used by Buckman *et al* [8] to measure cross sections at electron energies from 5 to 403 eV and 0.10–5.0 eV with an energy resolution of 300 and 250 meV respectively. A linear transmission method was employed by Szmytkowski *et al* [7] for electron energies varying from 0.5 to 80 eV at the energy resolution of 50 meV. The cross sections were also measured using the Ramsauer technique by Brüche [1] and Ramsauer and Kollath [2] and the normalized values of cross section were reported by Szmytkowski and Zubek [3] using a linear transmission method in the electron energy 1–49 eV, 0.2–2 eV and 2–8 eV respectively. The theoretically computed cross sections were reported by Morrison *et al* [9], Morrison and Lane [16], Collins and Morrison [17], and Lynch *et al* [18]. A theoretical coupled channels investigation was reported by Morrison *et al* [9] for incident electron energies from 0.07 to 10.0 eV. The fixed nuclei approximation was made with the molecule in the ground state and the nuclei frozen at their equilibrium positions. The static-model exchange-polarization interaction potential was used to calculate total integrated cross sections. The improvement in the method was carried out by Collins and Morrison [17] at electron energies ranging from 0.1 to 2 eV by using orthogonalized model potential. Lynch *et al* [18] calculated the integrated elastic electron scattering cross

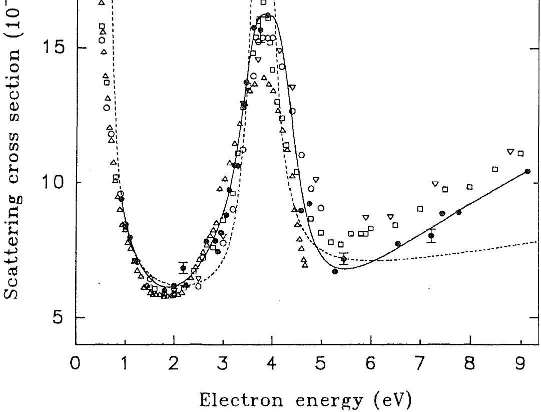

Figure 3. Total electron scattering cross sections for carbon dioxide as a function of incident energy from 0.91 to 9.14 eV obtained by various researchers. The symbols denote: o, Buckman *et al* [8]; ∇, Hoffman *et al* [5], ..., Morrison *et al* [9]; □, Szmytkowski *et al* [7]; Δ, Ferch *et al* [4]; •, present work; ————, cross section curve after proper curve fitting (present work).

section values reported by Brüche [1], Ramsauer and Kollath [2], Szmytkowski and Zubek [3], Morrison and Lane [16], Collins and Morrison [17] and Lynch *et al* [18] have not been included in figure 3.

For the sake of discussion, the cross section curve (figure 3) in the total electron energy range from 0–9 eV has been divided into three regions. These include energy regions below 2 eV, between 2 to 5 eV and between 5 to 9 eV. In the first energy region, the cross section has been found to decrease rapidly with increasing energy followed by a sharp increase at higher energies. This rapid decrease is mainly due to s-wave scattering and thus can be explained by a nearly bound $l = 0$ state in the e-CO_2 potential [9, 19]. The existence of such a virtual state has been verified both experimentally by Kochem *et al* [20] as well as theoretically by Estrada and Domcke [21]. At energies below 1.1 eV, there is an excellent agreement in cross section values reported by Buckman *et al* [8], Szmytkowski *et al* [7], Ferch *et al* [4], Morrison *et al* [9] and those obtained in the present experiment. But the agreement worsens at increasing energies. There is a large discrepancy between the results shown in figure 3 compared to values reported by Lynch researchers. The cross section and the energy minima have been reported in the present work and by Szmytkowski *et al* [7] to be 6.13 and 5.84 Å^2 at 1.88 and 1.90 eV respectively whereas Ferch *et al* [4], Hoffman *et al* [5], Buckman *et al* [8] and Morrison *et al* [9] have reported the cross section values of 5.85, 6.02, 5.84 and 6.21 Å^2 at the minima of around 1.8, 2.0, 2.0 and 2.0 eV respectively. It may be pointed out here that the minima stated above are not those directly measured by the respective groups, but rather are the results obtained by fitting curves to the values measured by them. Also, it may not be possible to have an exact energy minima in case of Buckman *et al* [8] and Hoffman *et al* [5]. In the first case [8], the energy steps used are large (0.5 eV) and therefore, elude finding the exact minimum; in the second case [5], there is no data available below 2.0 eV. A comparison of all these values shows that the largest disagreement in cross sections at the minimum is about 6.3%.

The results obtained in the present experiment in the energy region 2–5 eV (figure 3) shows a sharp increase in cross section up to the well known maximum centered around 3.8 eV followed by a sharp decrease up to 5 eV energy. The peak around 3.8 eV was attributed to the formation of a shape resonance [22]. The temporary state involved was the $^2\Pi_u$ of the CO_2^- ion having a short lifetime. In general, the shape of the resonance peak has been faithfully reproduced by all the work shown in figure 3 but the cross section values at the maximum of the resonance peak and also at the wings around the peak show some discrepancies. To have a clear comparison, the cross section curves reported by Ferch *et al* [4], Buckman *et al* [8], Hoffman *et al* [5], Szmytkowski *et al* [7], and Morrison *et al* [9] along with the curve obtained in the present experiment have been made to undergo proper curve fitting procedure. The cross section curve after proper curve fitting to the results obtained in the present experiment has also been shown in figure 3. This has been carried out using an appropriate mathematical function in the library of large number of such functions available in the Tablecurve-2D (Jandel Scientific) software. After proper fitting, the values of electron energy and cross section at the peak of the shape resonance, width of the peak at 75% of the maximum value and the slopes of the peak at 75% value on both wings of the peak have been obtained and these are given in table 1. The values of 75% was chosen as in most of the curves, it was difficult to get full width at half maximum. Also given in the table are the values of energy resolution used by researchers in their respective experiments. From the table, it is clear that there is a good agreement in the energy values obtained at the peak of the resonance but the cross section values show a large discrepancy between the present results and other investigations. There is large overestimation of cross section of 30.88 Å^2 by Morrison *et al* [9] and this is most likely due to the neglect of nuclear motion in the calculation [8]. The cross section values given by Ferch *et al* [4] and Buckman *et al* [8] are 14.2 and 5% lower as compared to the cross section reported in the present work whereas the cross section value (not given in table 1) reported by Sueoka and Mori [6] is almost 30% smaller. There is a fairly good agreement in the cross section value reported by Szmytkowski *et al* [7] and Hoffman *et al* [5] as compared to that given in the present experiment. It is expected that higher the energy resolution used in the experiment, higher given in table is the energy resolution used in different experiments.

		Peak value			$\lvert$Slope$\rvert$ in Å^2/eV at 75%	
CO_2	Energy resolution in meV	Electron energy (eV)	Cross section (Å^2)	ΔE at 75% of peak value (eV)	Rising	Falling
Ferch *et al* [4]	~250	3.8	13.9	1.3	6.4	9.7
Buckman *et al* [8]	~250	3.9	15.4	1.1	13.4	8.7
Hoffman *et al* [5]	~140	3.9	16.9	1.0	12.1	9.8
Szmytkowski *et al* [7]	~50	3.8	16.7	0.8	13.1	12.4
Morrison *et al* [9]	–	3.8	30.9	0.3	77.6	77.6
Present work	~45	3.8	16.2	0.9	13.9	14.7

other within the experimental uncertainties except possibly those of Ferch *et al* [4]. It appears that such a behaviour cannot be explained by the above argument alone but it is felt that the above behaviour could be explained by the combined effect of narrower electron energy width and better discrimination against small angle scattering in different experiments. In the present experiment, it has been shown that error in cross section values due to lack of discrimination against low angle scattering is about 0.5%. Hoffman *et al* [5] have pointed out that their measurements may be 1% too low at 4 eV and less than 1% too low at 10 eV because of inadequate discrimination against forward scattered electrons. In a subsequent paper, Buckman and Lohmann [23] have discussed about the problem of low angle scattering in their experimental system and estimated this error to be less than 0.1% at about 2 eV electron energy. The small angle contribution was estimated to be below 0.5% at all electron energies of interest in the experimental system reported by Szmytkowski *et al* [7] where as no such estimate was reported by Ferch *et al* [4].

Also given in table 1 are the ΔE values at 75% of the peak value of the shape resonance and modulus of the slopes at the two sides of the peak at 75% peak value. The values of the modulus of the slopes on the rising and falling sides of the peak as given by different experimental groups show that the resonance peak is more or less symmetrical around the maximum in the present work as well as in the experiment reported by Szmytkowski *et al* [7] whereas the experiments by Ferch *et al* [4], Buckman *et al* [8] and Hoffman *et al* [5] show that the resonance peak is asymmetrical in nature. This may be attributed to the energy resolution used in the experiment. It has been found (table 1) that higher the energy resolution, more symmetrical is the resonance peak around the maximum.

In the energy region from 5–9 eV, cross section values reported by the three experimental groups only ([5, 7] and present work) have been shown in figure 3 along with the theoretically computed values of Morrison *et al* [9]. Unfortunately, Ferch *et al* [4] and Buckman *et al* [8] have not carried out these measurements beyond 4.62 and 5.0 eV respectively. The general trend in this energy region as suggested by different research

Wavelength λ (Å^2)	Source gas	Photo-ion state	Electron energy (eV)	Cross sect (Å^2)
744	Ar	$^2P_{3/2}$	0.91	9.38
736	Ar	$^2P_{3/2}$	1.09	7.96
584	CO_2	$\tilde{C}^2\Sigma_g^+$	1.80	6.01
744	Kr	$^2P_{1/2}$	2.00	6.19
736	Kr	$^2P_{1/2}$	2.18	6.84
744	Kr	$^2P_{3/2}$	2.66	7.83
736	Kr	$^2P_{3/2}$	2.85	7.84
744	CO_2	$\tilde{X}^2\Pi_g$	2.90	7.44
584	CO_2	$\tilde{B}^2\Sigma_u^+(\nu = 1)$	2.96	8.15
736	CO_2	$\tilde{X}^2\Pi_g$	3.07	8.80
584	CO_2	$\tilde{B}^2\Sigma_u^+(\nu = 0)$	3.12	9.74
744	Xe	$^2P_{1/2}$	3.23	10.65
584	CO_2	$\tilde{A}^2\Pi_u(\nu = 4)$	3.31	10.62
736	Xe	$^2P_{1/2}$	3.41	12.89
584	CO_2	$\tilde{A}^2\Pi_u(\nu = 3)$	3.46	13.74
584	CO_2	$\tilde{A}^2\Pi_u(\nu = 2)$	3.61	15.75
584	CO_2	$\tilde{A}^2\Pi_u(\nu = 1)$	3.75	15.68
584	CO_2	$\tilde{A}^2\Pi_u(\nu = 0)$	3.89	16.22
744	Xe	$^2P_{3/2}$	4.59	8.95
736	Xe	$^2P_{3/2}$	4.77	9.21
584	Ar	$^2P_{1/2}$	5.28	6.71
584	Ar	$^2P_{3/2}$	5.46	7.18
584	Kr	$^2P_{1/2}$	6.55	7.73
584	Kr	$^2P_{3/2}$	7.22	8.02
584	CO_2	$\tilde{X}^2\Pi_g$	7.44	8.85
584	Xe	$^2P_{1/2}$	7.78	8.88
584	Xe	$^2P_{3/2}$	9.14	10.43

et al [7] and Hoffman *et al* [5] occurs almost at the same energy of about 5.4 eV
different cross section values of 6.9, 7.9 and 8.5 Å^2 respectively. Morrison *et a*
reported a minimum value of 7.1 Å^2 at the electron energy of 6.0 eV but the increa
cross section values was rather slow at higher electron energies. At electron ene
between 5.5 and 9 eV, rate of change of cross section per unit electron energy has
found to be almost similar in the three cases, but absolute values of cross section
quite different. At the two typical energies 7.5 and 9.0 eV, the cross section v
reported in the present work are lower by 10% and 7% as compared to those give

the corresponding electron energy.

References

[1] E Brüche, *Ann. Phys. Lpz.* **83**, 1 (1927)
[2] C Ramsauer and R Kollath, *Ann. Phys. Lpz.* **4**, 91 (1930)
[3] C Szmytkowski and M Zubek, *Chem. Phys. Lett.* **57**, 105 (1978)
[4] J Ferch, C Masche and W Raith, *J. Phys. At. Mol. Phys.* **14**, L97 (1981)
[5] K R Hoffman, M S Dababneh, Y-F Hsiech, W E Kauppila, V Pol, J H Smart and T S Stein, *Phys. Rev.* **A25**, 1393 (1982)
[6] O Sueoka and S Mori, *J. Phys. Soc. Jpn.* **53**, 2491 (1984)
[7] C Szmytkowski, A Zecca, G Karwasz, S Oss, K Maciag, B Marinkovic, R S Brusa and R Grisenti, *J. Phys.* **B20**, 5817 (1987)
[8] S J Buckman, M T Elford and D S Newman, *J. Phys.* **B20**, 5175 (1987)
[9] M A Morrison, N F Lane and L A Collins, *Phys. Rev.* **A15**, 2186 (1977)
[10] V Kumar, E Krishnakumar and K P Subramanian, *J. Phys.* **B20**, 2899 (1987)
[11] K P Subramanian and V Kumar, *J. Phys.* **B20**, 5505 (1987)
[12] K P Subramanian and V Kumar, *J. Phys.* **B22**, 2387 (1989)
[13] K P Subramanian and V Kumar, *J. Phys.* **B23**, 745 (1990)
[14] J A R Samson and L Yin, *J. Opt. Soc. Am.* **B6**, 2326 (1989)
[15] M Karras, M Pessa and S Aksela, *Ann. Acad. Sci. Finnicae* **AVI**, 289 (1968)
[16] M A Morrison and N F Lane, *Phys. Rev.* **A16**, 975 (1979)
[17] L A Collins and M A Morrison, *Phys. Rev.* **A25**, 1764 (1982)
[18] M G Lynch, D Dill, J Siegel and J L Dehmer, *J. Chem. Phys.* **71**, 4249 (1979)
[19] M A Morrison, *Phys. Rev.* **A25**, 1445 (1982)
[20] K H Kochem, W Sohn, N Hebel, K Jung and H Ehrhardt, *J. Phys.* **B18**, 4455 (1985)
[21] H Estrada and W Domcke, *J. Phys.* **B18**, 4469 (1985)
[22] C R Claydon, G A Segal and H S Taylor, *J. Chem. Phys.* **52**, 3387 (1970)
[23] S J Buckman and B Lohmann, *Phys. Rev.* **A34**, 1561 (1986)

Magnetization of high-T_c superconductors

B KALTA and K K NANDA*
Sonepur College, Subarnapur, India
*Institute of Physics, Bhubaneswar 751 005, India
E-mail: nanda@iopb.stpbh.soft.net

MS received 19 July 1997; revised 28 January 1998

Abstract. We have tried to understand the field dependence of magnetization of high temperature superconductors in the light of phenomenological theory. Especially, the field dependence of $\mathrm{d}M/\mathrm{d}\ln B$ of polycrystalline Bi(2212) is understood by incorporating the overlap of vortices in the London theory.

Keywords. High-T_c superconductors; magnetization; phenomenological theory.

PACS Nos 74.25; 74.20

The magnetic properties of high temperature superconductors (HTSCs) in magnetic fields are very unusual near the transition temperature T_c and are different for different HTSCs. Near T_c, the magnetization (M) of Y(123) is proportional to $(T - T^*)^2$, where T^* is almost field independent and close to T_c [1, 2]. It has also been observed that the magnetization of Y(123) is approximately logarithmic in B_a in the reversible region and can be understood by using 3D description of the London theory [3–5]. It has also been applied to understand the temperature dependence of specific heat in magnetic field [6], whereas, the field dependence is understood by incorporating the overlap of vortices in the London theory [7]. Incorporating the overlapping of vortices in the London theory the magnetization for 3D superconductors can be written as [7]

$$M = M_L = \frac{B - H}{4\pi} = -\frac{\phi_0}{32\pi^2\lambda_{\mathrm{eff}}^2}\ln\left(\frac{B_{c2}}{B_a}\right) = -\frac{\phi_0 f^2}{32\pi\lambda^2}\ln\left(\frac{B_{c2}}{B_a}\right). \tag{1}$$

This is similar to the result obtained from the variational model [8] in the London limit. The temperature dependence of penetration depth and the upper critical field is given by [9]

$$\lambda(T) = \frac{\lambda_0}{\sqrt{2}(1 - t)^{\beta}} \quad \text{and} \quad B_{c2} = B_{c20}(1 - t)^{2\nu}, \tag{2}$$

where $t = T/T_c$. The ν is 1/2 in the mean field region and 2/3 in the critical region.

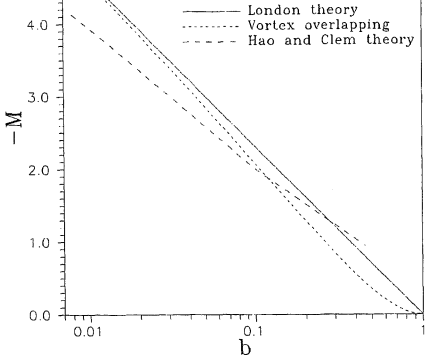

Figure 1. The magnetization (in units of $\phi_0/32\pi^2\lambda^2$) vs b.

which are in between that obtained from the usual London theory and the variational approach proposed by Hao *et al* [7] and the magnetization is approximately logarithmic in B_a. Near B_{c2} or close to T_c, the logarithmic term in eq. (1) can be expanded as $(1-(B_a/B_{c2})$. So the magnetization behaves as $(B_{c2}-B_a)^2$ or $(T_c-T)^2$. If the upper critical field is large, the change on T_c with magnetic field is little as observed experimentally [1, 2].

The magnetic properties of Bi(2212) are different from Y(123). In the intermediate field range, the $-4\pi M$ vs $\ln B_a$ curve of Bi(2212) single crystal is not linear as predicted from the London theory. The variation in the case of single crystal [10, 11] is different from the polycrystalline case [12]. According to the mean field theory developed by Koshelev [13] (from eq. C11), the field dependence of the slope $\mathrm{d}M/\mathrm{d}\ln B$ can be written as

$$\frac{\mathrm{d}M}{\mathrm{d}\ln B}=\frac{\phi_0}{32\pi^2\lambda^2(T)}\left[1+2\frac{B_a}{B_{c2}}\ln\left(\frac{B_a}{\eta e B_{c2}}\right)\right]\quad \text{with}\quad \eta=0.35. \tag{3}$$

Whereas, according to the vortex overlapping mechanism [7], it is given by

$$\frac{\mathrm{d}M}{\mathrm{d}\ln B}=\frac{\phi_0}{32\pi^2\lambda^2(T)}\left[1-\frac{B_a}{B_{c2}}\ln(eB_a/B_{c2})\right]. \tag{4}$$

Shown in figure 2 is the $\mathrm{d}M/\mathrm{d}\ln B$ versus B_a. The dashed line represents the Koshelev's result and the solid line represents the vortex overlapping result. It is noted from this figure that both mean field theory and vortex overlapping mechanism predicts different

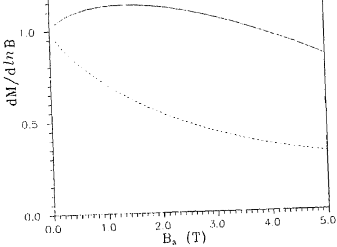

Figure 2. $\mathrm{d}M/\mathrm{d}\ln B_a$ (in units of $\phi_0/32\pi^2\lambda^2$) versus B_a. For the solid line we have taken $B_{c2} = 10$ and for dashed line $B_{c2} = 20$ T.

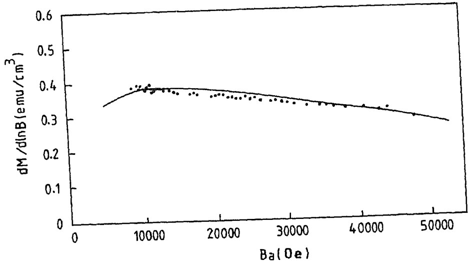

Figure 3. The field dependence of $\mathrm{d}M/\mathrm{d}\ln B_a$ of a polycrystalline Bi(2212) sample at $T = 55$ K. The data are taken from figure of ref. [12]. The solid line is a theoretical fit according to eq. (4) with parameters $\lambda = 4017$ Å and $B_{c2} = 100$ T.

Genoud *et al* [12] have claimed that the polycrystalline data can be fitted to Koshelev's prediction quantitatively. In this context, it is worth pointing out that eq. (C11) and (C12) of ref. [13] predicts similar field dependence for $\mathrm{d}M/\mathrm{d}\ln B$. Hence, the claim of Genoud *et al* is not justified. In order to verify the overlapping mechanism quantitatively, we have taken the data of Genoud *et al* [12] for a polycrystalline sample and compared with eq. (4) as shown in figure 3. The solid line is a fit to the data according to eq. (4) with $\lambda = 4017$ Å and $B_{c2} = 100$ at $T = 55$ K. These values are reasonably in good agreement with earlier reported results implying that the field dependence of $\mathrm{d}M/\mathrm{d}\ln B$ can be understood by incorporating the overlap of vortices in the London theory.

In conclusion, the field dependence of $\mathrm{d}M/\mathrm{d}\ln B$ of polycrystalline Bi(2212) is

[1] K S Athreya *et al*, *Phys. Rev.* **B38**, 11846 (1988)

[2] U Welp, W K Kwok, G W Crabtree, K G Vandevoort and J Z Liu, *Phys. Rev. Lett.* (
(1989); *Physica* **C162–164**, 735 (1989)

[3] V G Kogan, M M Fang and S Mitra, *Phys. Rev.* **B38**, 11958 (1988)

[4] S Mitra *et al*, *Phys. Rev.* **B40**, 2674 (1989)

[5] G Triscone *et al*, *Physica* **C224**, 263 (1994)

[6] S B Ota, *Phys. Rev.* **B43**, 1237 (1991)
S B Ota, K K Nanda and S N Behera, *Physica* **B194–196**, 1387 (1994)

[7] K K Nanda, *Physica* **C245**, 341 (1995)

[8] Z Hao, J R Clem, M W McElfresh, L Civale, A P Malozemoff and F Holtzberg, *Ph*
B43, 4844 (1991)
Z Hao and J R Clem, *Phys. Rev. Lett.* **67**, 2371 (1991)

[9] L N Bulaevskii, V L Ginzberg and A A Sobyanin, *Physica* **C152**, 378 (1988)

[10] M Tuominen, A M Goldmann, Y Z Chang and P Z Jiang, *Phys. Rev.* **B42**, 412 (199

[11] V G Kogan, M Ledvij, A Yu Simonov, J H Cho and D C Johnston, *Phys. Rev. Lett.* 7
(1993)

[12] J-Y Genoud, G Triscone, A Junod, T Tsukamoto and J Muller, *Physica* **C242**, 143 (

[13] A E Koshelev, *Phys. Rev.* **B50**, 506 (1994)